A. Thermomechanical Processing Design for Lightweight Materials

Principal Investigator: Esteban B. Marin
Senior Structural Analyst
Center for Advanced Vehicular Systems (CAVS)
Mississippi State University (MSST)
200 Research Blvd.
Mississippi State, MS 39762
(662) 325-6696; e-mail: ebmarin@cavs.msstate.edu

Co-Principal Investigator: Paul T. Wang
Manager, Computational Manufacturing and Design
CAVS, MSST
P.O. Box 5405
Mississippi State, MS 39762-5405
(662) 325-2890; e-mail: pwang@cavs.msstate.edu

Sebastien Groh
CAVS, MSST
200 Research Blvd
Mississippi State, MS 39762
(662) 325-5576; email: groh@cavs.msstate.edu

Stephen Horstemeyer
CAVS, MSST
200 Research Blvd
Mississippi State, MS 39762
(662) 325-3685; email: sjhorst@cavs.msstate.edu

Andrew Oppedal
CAVS, MSST
200 Research Blvd
Mississippi State, MS 39762
(662) 325-8502; email: aoppedal@cavs.msstate.edu

Clemence Bouvard
CAVS, MSST
200 Research Blvd
Mississippi State, MS 39762
email: clemence@cavs.msstate.edu

Co-Principal Investigator: Wei Chen
Professor of Mechanical Engineering
Robert R. McCormick School of Engineering and Applied Science
Northwestern University (NWU)
Department of Mechanical Engineering
2145 Sheridan Road
Evanston, Illinois 60208-3111
(847) 491-7019; e-mail: weichen@northwestern.edu

Co-Principal Investigator: Jian Cao
Professor of Mechanical Engineering
Robert R. McCormick School of Engineering and Applied Science
NWU
Department of Mechanical Engineering
2145 Sheridan Road
Evanston, Illinois 60208-3111
(847) 467-1032; e-mail: jcao@northwestern.edu

Balasubramaniam Radhakrishnan
Oak Ridge National Laboratory (ORNL)
1 Bethel Valley Road
Oak Ridge, TN 37831-6164
(865) 241-3861; e-mail: radhakrishnb@ornl.gov

Gorti Sarma
ORNL
1 Bethel Valley Road
Oak Ridge, TN 37831-6164
(865) 574-5147; e-mail: sarmag@ornl.gov

Joe Horton
ORNL
1 Bethel Valley Road
Oak Ridge, TN 37831-6115
(865) 574-5575; e-mail: hortonja@ornl.gov

Objective

The project is aimed at developing physics-based, experimentally-validated thermo-mechanical processing models and design methodologies for improving manufacturability and forming technology of lightweight materials such as wrought aluminum (Al) and magnesium (Mg) alloys.

Approach

The technical approach is (i) to build an experimental material database that captures the important features of microstructure evolution during hot/cold rolling, stamping, and extrusion processes of Al and Mg alloys, (ii) to develop a multiscale material model using an internal state variable (ISV) formalism that is able to predict microstructure evolution (hardening, recovery, recrystallization, and texture-induced anisotropy) of metals during thermo-mechanical processing, (iii) to construct numerical models of metal forming (rolling, stamping, extrusion) for process design, and (iv) to employ optimization techniques with uncertainty to establish an integrated approach for material-process design using simulation-based techniques.

Main activities (subtasks) planned to perform the proposed research are the following:

- Develop plane-strain compression (rolling), bi-axial stretching (stamping), and lab-scale extrusion techniques for Al/Mg alloys at room and elevated temperature.

- Build an experimental database capturing microstructure evolution of Al alloys.

- Perform pilot-scale rolling experiments and material characterization of Mg alloys.

- Extend experimental database with microstructure information for Mg alloys.

- Develop multiscale ISV model to predict microstructure evolution of Al and Mg alloys during thermo-mechanical processing.

- Construct thermo-mechanical process models and develop manufacturability metrics for process design (rolling, stamping, and extrusion).

- Develop methodologies for uncertainty quantification and reliability-based design optimization of metal-forming processes.

Team members participating in this task are:

MSST: Paul Wang, Esteban Marin (macroscale ISV model development, extrusion modeling), Sebastien Groh (support ISV model development with micro-scale/discrete dislocation/crystal plasticity simulations), Stephen Horstemeyer (lab-scale extrusion experiments), Andrew Opeddal (mechanical testing of magnesium), Clemence Bouvard (extrusion simulations).

ORNL: Balasubramaniam Radhakrishnan and Gorti Sarma (support ISV model development with meso-scale/crystal plasticity simulations), Joe Horton (pilot-scale rolling experiments and characterization of Mg alloys).

NWU: Jian Cao (biaxial stretching experiments and stamping simulations), Wei Chen (design optimization under uncertainty).

Accomplishments

- Performed microstructure analyses and mechanical tensile tests on 6022 aluminum alloy. The samples were extracted from material at different stages of a rolling process used to manufacture aluminum sheets for automobile panels. The rolling steps comprise reductions of a 6-inch billet to a 3-inch billet to a 1/8-inch sheet, an annealing process of the 1/8-inch sheet, and, finally, a reduction to the 1/32-inch finish gauge sheet. The microstructure studies determined grain morphology, texture, inclusion/precipitate content, and void distribution through scanning electron microscope (SEM) analyses, optical microscopy (OM) analyses, and X-ray tomography. Mechanical properties were determined from tensile tests at different strain rates, temperatures, and material directions (rolling and transverse) using an Instron 5882 electromechanical machine. The history effects in the material microstructure-property relationship induced by the rolling stages and captured in the experimental data provides a database for advanced material modeling (MSST).

- Carried out channel die compression experiments at room temperature on Al6022 with an in-house designed fixture. Plane-strain compressed specimens (reduction of 60%) were annealed at different temperatures and times and then subjected to micro-indentation tests. Hardness measurements showed the sigmoidal shape typically depicted by plots of differential hardness versus annealed time. Electron backscatter diffraction (EBSD) studies were also performed on a number of annealed specimens to quantify the fraction of recrystallized material. Results showed the general trends typically observed in recrystallization phenomena: the higher the annealing temperature and the longer the annealing time, the higher the fraction of recrystallized grains (MSST).

- Completed mechanical testing and texture measurements of pure polycrystalline magnesium deformed under simple compression. In these experiments, samples extracted from extruded/ rolled plates were compressed in the through-thickness and in-plane transverse directions. Results from these tests (stress-strain curves and texture) showed clearly the effect of twinning on the deformation behavior of the material. Additional experiments considering strain path changes and temperature reloads are considered for the future (MSST).

- Performed extrusion tests on magnesium alloy AZ61 using a lab-scaled indirect extrusion fixture designed to learn about the process and generate experimental data for modeling purposes. Experimental results captured the global load-displacement curve of the test and the evolution of local temperatures at specific points in the billet. Interrupted extrusion tests (at 20%, 50% and 75% extruded billet) clearly revealed the development of flow patterns typical of extrusion processes. EBSD studies on some of these partially extruded billets showed the microstructure evolution during the process (grain morphology, texture, and recrystallization). A test matrix was designed to perform a parametric study of the process. Selected processing parameters are the following: billet temperature, ram velocity, and extrusion ratio. These experiments are currently underway (MSST).

- Magnesium Elektron North America Inc. (MEL) cast 97 experimental alloy slabs. A recipe adapted to ORNL's mill size was developed to allow hot rolling of these slabs to a thickness of 1.5 mm. During the project, 32 of the alloys were rolled, tested, and analyzed. Results showed that several of the alloys have strengths and ductilities near those of AZ31. Recovery/recrystallization on one selected alloy (AZ31b-H24) showed that only 15min at 200°C or 8min at 250°C was required for recovery as contrasted with the standard ASM handbook recommendations of 1 hour at 345°C (ORNL).

- Investigated kinematic hardening behavior in sheet metals using a novel design of test apparatus and a new model. To measure the strain correctly, the transmission type laser extensometer was utilized and the double-side fins were considered in the sheet specimen. Test results showed that this (double-wedge) device can perform stable tension-compression (15% pre-strain) and compression-tension (9% pre-strain) tests for a sheet thickness of 0.8mm. A good repeatability for a couple of cyclic tests was also observed (NWU).

- Examined forming limits of rolled aluminum sheets Al 6022 using limit-dome tests at room temperature. Various widths of samples were employed to obtain various strain paths. Test results showed a 0.025 strain variation in the forming limit curve (NWU).

- Obtained the forming limit curves of magnesium sheet AZ31 at two temperatures: 200C and 170C. Various specimen widths were used. Results showed that the material displays a good formability at both temperatures. Hence, the lower forming temperature was suggested to be used due to energy considerations (NWU).

- Made an attempt to simulate material behavior of magnesium alloys using a phenomenological approach. The material model used had an orthotropic yield function with separate hardening laws for tension and for compression. Model implemented in a commercial code predicted the asymmetry in the yield stress in tension and in compression (NWU).

  1. Established a preliminary hierarchical multi-scale modeling approach to predict the inelastic deformation of face-centered cubic metals. This approach builds a clear bridging methodology connecting nano-, micro- and meso-scales: Dislocation mobility data numerically generated using molecular dynamic simulations (nano-scale) is used by a discrete dislocations approach (micro-scale) to determine the material parameters for a particular slip system hardening law typically employed in crystal plasticity models (meso-scale). This bridging methodology has been validated by using the multiscale crystal plasticity model to predict the mechanical response of an Al single crystal deformed under uniaxial compression. The computed strain-stress response agrees well with experimental data from the literature (MSST).

  2. Performed quasi-statics and dynamics calculations in magnesium to establish a dislocation mobility rule for each slip system. Peierls stresses (minimum stress needed to move a dislocation at 0 K) were calculated for each slip system, and a good agreement with experimental data was obtained. At finite temperatures two types of anisotropy were identified, which were related (i) to the dislocation character and (ii) to the slip system. Independently of the slip systems, edge dislocations move faster than screw dislocations, and regardless of the dislocation character (edge or screw), dislocations moving in the basal plane travel faster than dislocations sliding in the prismatic plane. Viscous-drag coefficients were calculated for each character lying in each slip system (MSST).

  3. Implemented and tested kinematics, kinetics, and hardening rules for twinning deformation in a crystal plasticity code. Analyzed dislocation/twin activities in a magnesium single crystal under different loading conditions and used that information to identify the parameters of slip hardening rules. This multiscale material model of magnesium alloys reproduced well the anisotropy reported in the literature (MSST).

  4. Carried out void growth and coalescence studies in mono-crystalline magnesium out using molecular dynamics calculations to reveal the dependence of strain rate, temperature, and orientation of the crystal on damage evolution. The model set-up considered a cubic specimen containing an initial spherical void in the center. Two specific crystallographic orientations were analyzed: [0001] and [11-20]. During a [0001] tensile test, twin boundaries developed at the void surface, leading to a constraint on void growth. On the other hand, during a [11-20] tensile test, emission of shear loop in the prismatic slip planes is at the origin of void growth. Furthermore, analysis of the damage components

(nucleation, growth, and coalescence) revealed that a large number of small voids nucleated, leading to coalescence and then fracture of the specimen. This process was independent of the temperature and the applied strain rate (MSST).

5. Employed the visco-plastic self-consistent model of crystal plasticity to model the mechanical behavior and texture evolution of pure magnesium specimens compressed through the thickness and in-plane transverse directions. This constitutive framework incorporates both slip and deformation twinning. In particular, the composite grain twinning model and a dislocation density based constitutive hardening model were employed in these simulations. The model predicted well the experimentally-determined evolution of texture and stress-plastic strain response (MSST).

6. Used the Eulerian-ALE (Arbitrary Lagrangian Eulerian) finite element code HyperXtrude to simulate the lab-scale indirect extrusion experiments. This commercial code has been designed to model the non-isothermal flow of an incompressible viscous material. The simulation used the sine hyperbolic inverse flow stress model and the material parameters for aluminum embedded in the database of the code. The numerical results predict well the trends in flow patterns of the experiments. The recently released version of the code allows using user material functions. This new functionality will be employed to couple CAVS constitutive models to the code for simulation of magnesium extrusion (MSST).

7. Applied meso-scale models (crystal plasticity and Monte Carlo techniques) to predict the texture evolution during thermo-mechanical processing of Al 6022 sheet. Good agreement was obtained between model predictions and experimental textures obtained for direct annealing of the hot band and after cold rolling and annealing of the hot band (ORNL).

8. Carried out benchmark simulations of microstructure deformation of hexagonal close-packed polycrystals using a finite-element code developed at ORNL. Numerical results were compared with those obtained using material point simulations as well as the models developed at MSST. Excellent agreement was obtained (ORNL).

9. Developed a new recovery model for cube texture evolution in aluminum. The nucleation model was based on orientation dependent "excess dislocations" and was incorporated into Monte Carlo recrystallization simulations. Model successfully predicted the strengthening of Cube texture during recrystallization following plane strain compression (ORNL).

- Established a design optimization framework for sheet-stamping process with considerations of both robustness and reliability requirements. The framework relies on a probabilistic design model that incorporates uncertainty as well as failure margins for both tearing and wrinkling as design requirements. The framework considered state-of-the-art uncertainty propagation techniques to improve the efficiency of the process with respect to other typical methods: analytical probabilistic models and sampling-based approximations (Monte Carlo technique) (NWU).

- Proposed a procedure for robust design optimization using the Gauss-type quadrature formula, with an emphasis on the efficient calculation of design sensitivities. Typically, evaluation of statistical moments requires multiple function evaluations, and, as such, the design sensitivity evaluation using approximate schemes such as finite difference method increases significantly the computational cost of optimization. In this work, formulas for semi-analytic design sensitivity of statistical moments were derived for tensor product and univariate dimension reduction method. It was shown that the proposed design sensitivity analysis reduces the computational cost of robust design up to 40 % when compared to the finite difference method (NWU).

- Proposed a level-set-based method for robust shape and topology optimization. This method considered uncertainties as represented by random variables or random fields. In this method, the problem is mathematically formulated by expressing the statistical moments of a response as functionals of geometric shapes and loading/material uncertainties. Spectral methods are employed for reducing the dimensionality in uncertainty representation and the Gauss-type quadrature formulae is used for uncertainty propagation. Preliminary 2D and 3D results show that this methodology can lead to designs with different shapes and topologies and superior robustness compared to their deterministic counterparts (NWU).

- Developed a statistical volume element method to analyze, quantify, and calibrate multi-length scale statistical microstructure-constitutive property relations for material-product design applications. The approach used statistical volume element simulations to predict material properties corresponding to various realizations of random microstructure configurations. Computed statistical constitutive properties were then used to calibrate the model parameters in a macroscopic constitutive model. As such, the calibrated material model, which incorporated the uncertainties propagated from random material microstructure, facilitated the probabilistic analysis of material performance at the continuum level in multi-scale design and analysis (NWU).

- Developed a multi-scale design approach with an emphasis on the treatment of material uncertainty across a product domain as random field. The approach integrates manufacturing simulations, multi-scale material models, and product models in a multi-scale framework. Hence, it allows either hierarchical or concurrent designs of manufacturing process, material, and product in a multi-scale context. A control arm design problem considering the spatial variation of initial porosity level due to casting process was used to demonstrate the applicability of the proposed approach (NWU).

- Established an enhanced hierarchical statistical sensitivity analysis method for designing systems with dependent subsystem responses. A top-down strategy is employed to direct sensitivity analysis from the top level to lower levels. The method utilized the concept of a subset statistical sensitivity analysis (SSA) to group a set of dependent responses from lower level sub-models in the upper level SSA. The effectiveness of the proposed method was illustrated and verified via a mathematical example and a multi-scale design problem (NWU).

- Proposed a multi-scale design methodology to facilitate the design of a hierarchical materials-product system with the consideration of random field uncertainty propagated across multiple length scales. Novel design of experiments and metamodeling strategies were proposed to manage the complexity of propagating uncertainties. A hierarchical multi-scale engineering system that involved a 2-scale (sub-micro- and micro-scales) material design and a macro-scale product (bracket) design was used to demonstrate the applicability of the proposed methodology (NWU).

Introduction

Thermo-mechanical processing (TMP) is typically used to improve the mechanical properties of a material by inducing changes in its microstructure (grain structure, texture, and precipitates). Properties such as plasticity, strength, ductility, and formability can be tailored by a proper design of the different steps in TMP (e.g., hot/cold rolling, extrusion, heat treatment, stamping) as well as by the design of material microstructure. In this context, building robust design methodologies and multi-scale design methods under uncertainty for TMP can contribute to improve current manufacturing processes and/or fix many technical problems (e.g., formability) that at present hinder the production of selected lightweight materials such as Mg alloys.

The focus of Task 8, "Thermo-Mechanical Processing Design for Lightweight Materials," is to build a comprehensive framework that facilitates the reliability-based optimum design of TMP for lightweight materials. This framework includes building an extensive material database capturing the processing-structure-property relationship of Mg and Al alloys, developing a multiscale constitutive approach that captures the history-dependent response of the alloys, and establishing the methodologies for uncertainty quantification/propagation together with an integrated robust and reliability optimization method for TMP as applied to Al and Mg alloys.

This document is the final report of this task. It presents a summary of the main research activities performed by the team members participating in this two-year project. Three institutions are represented in this task: Mississippi State University (MSST), Oak Ridge National Laboratory (ORNL) and Northwestern University (NWU). Based on this, this report has been organized in three main sections, each of them describing the particular institution's activities carried out during the project.

Research Activities at Mississippi State University

Material Database for Aluminum and Magnesium Alloys

Microstructure and Mechanical Characterization of 6022 Aluminum Alloy

The 6022 aluminum alloy was developed by Alcoa primarily for automotive panel applications. The automotive body panels are fabricated using a stamping process of thin gauge aluminum sheets. These sheets are manufactured through a rolling process that comprises reductions from a 6-inch billet to a 3-inch billet to a 1/8-inch sheet through a series of hot rolling steps. The 1/8-inch sheet is then put through an annealing process and finally reduced through cold rolling to the 1/32-inch finish gauge sheet which is used to manufacture the automotive panels (Figure 1).
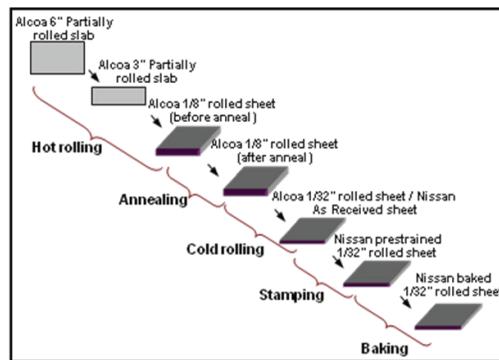
Figure 1. Manufacturing process of 6022 Aluminum sheet (Alcoa).

For the project (in fact, most of the work was performed in a parallel DOE project), 6022 aluminum alloy material was provided by Alcoa Inc. at various stages of the manufacturing process. Samples from this material were extracted to determine their processing-structure-property relationship. Microstructure studies were performed to determine grain morphology, texture evolution, inclusion/precipitate content, and void distribution. Mechanical properties were determined using tensile tests at different strain rates, temperatures, and material directions (rolling versus transverse). Some experimental results obtained in these studies are presented in Figures 2 and 3.
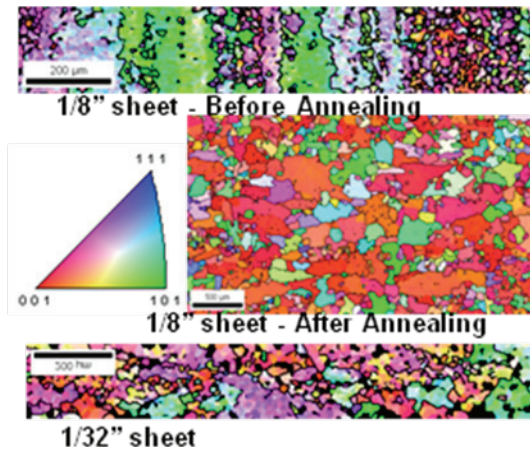
Figure 2. Inverse pole figure maps for 6022 aluminum rolled sheet at some stages during its manufacturing process.
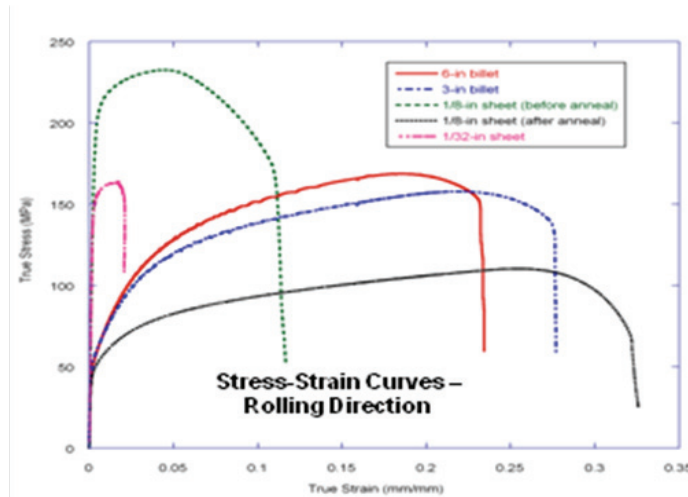
Figure 3. Tensile stress-strain curves for 6022 aluminum at different stages during its manufacturing process. Tests performed at ambient temperature with a constant strain rate of 0.0001 sec-1.

The material database built for the manufacturing process of 6022 Aluminum captures then the deformation history effects on the material and should be useful to improve the manufacturability of these aluminum sheets. Besides, the database is providing useful information for advanced constitutive modeling development.

Channel Die Compression (CDC), Annealing, and Recrystallization Studies on Al 6022

A CDC fixture was designed to perform room temperature plane strain compression experiments (Figure 4). Using this new fixture, CDC tests were performed on samples of Al6022 extracted from a 1/8" rolled plate.

a.

b.

Figure 4. (a) Fixture designed for channel die compression experiments and (b) samples of deformed specimen at different levels of strain (up to 50% strain).

Each CDC test used 2 specimens, with dimensions 5mm × 10mm, stacked and super-glued together to prevent the surfaces from sliding along one other. To reduce friction between the samples and the channel die, the samples are wrapped in Teflon tape and polytetraflouroethylene powder is applied to the surfaces. Using an Instron machine and the CDC fixture, the samples are then compressed at room temperature up to a strain of 60% at a rate of 0.05 in/min.

The deformed samples were then annealed in a salt bath at temperatures of 375, 400°C, and 425°C with annealing times varying from 0 to 5000 seconds (Figure 5). After the prescribed annealing time, each sample was removed from the furnace and immediately quenched in water.
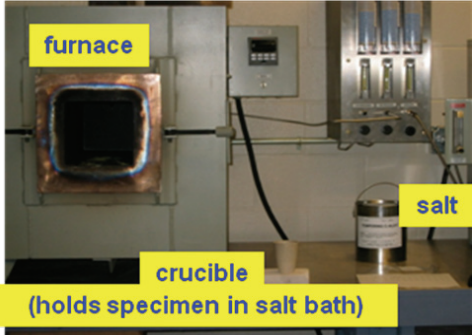
Figure 5. Annealing equipment for CDC samples of Al6022.

The annealed samples were next prepared for hardness measurement using a micro-indenter. Partial results from these tests are presented in Figure 6. As expected, the hardness values decrease for longer annealing times and for higher temperatures. The plot of differential hardness versus annealing time (Figure 6b) shows a typical sigmoidal shape representative of
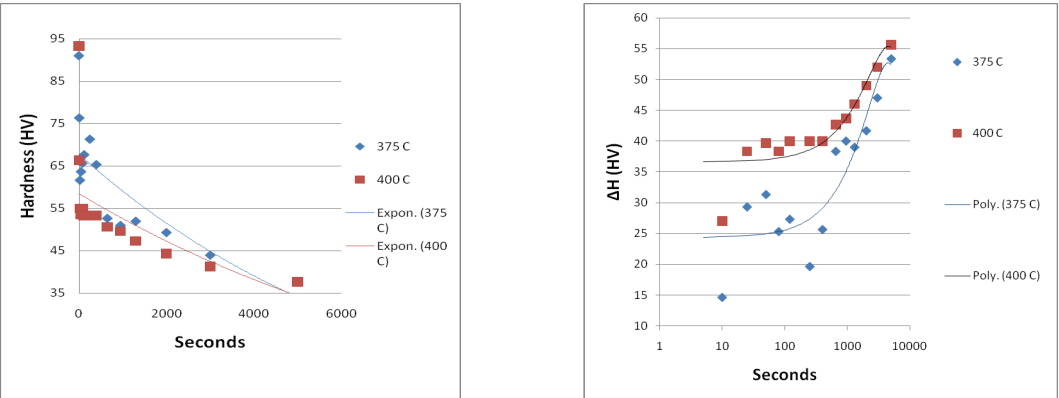
recrystallization processes.

Figure 6. (a) Hardness versus time and (b) differential hardness versus time for the annealed Al6022 specimens. HV denotes the Vickers Hardness.

A number of the annealed samples were then prepared for microstructure analysis using electron back scatter diffraction (EBSD) scans to quantify the fraction of recrystallized grains, information needed to model the recrystallization kinetics in Al alloys. The main characteristic analyzed in these studies is the orientation spread of deformed and re-crystallized grains. The Grain Orientation Spread (GOS) is the average value of orientation spread in a grain. For partially recrystallized and deformed samples, the difference in GOS provides a way of separating deformed and recrystallized regions. A single GOS value can be used for all re-crystallized grains on different samples. Here, a GOS angle of around 2° has been employed to identify grains that have been re-crystallized.

Data were collected using EBSD for the samples with annealing times of 50s, 250s, and 5000s, all annealed at 375°C, 400°C, and 425°C. From the collected data, the fraction recrystallized was determined for each sample. Table 1 shows the computed fraction of recrystallized grains. Although not fully consistent, the table shows the general trends typically observed in recrystallization studies: the higher the annealing temperature and the longer the annealing time, the higher the fraction of recrystallized grains. Figures 7 and 8 show selected grain maps from the EBSD studies. Clearly, the typical trends mentioned above are observed in these micrographs.

(a)

(b)

Figure 7. Grain maps for annealing at 400C: (a) 50 s and (b) 5000s.

(a)

(b)

Figure 8. Grain maps for annealing at 425C: (a) 50 s and (b) 5000 s.

	50s	250s	5000s
375°C	.815	.825	.885
400°C	.90	.865	.920
425°C	.820	.835	.86

Table 1. Fraction Recrystallized For Selected Samples

Mechanical Testing and Texture Measurements on Pure Polycrystalline Magnesium

Magnesium alloys have attractive properties in applications that favor lower weight [Mordike 2001]. However, magnesium alloys exhibit a hexagonal close packed (HCP) crystalline structure that leads to low ductility and strong anisotropy compared to other face centered cubic and body centered cubic metals. If the ductility and anisotropy could be controlled, magnesium alloys could be developed and formed to fill an increasing market as lighter weight, more fuel efficient vehicles become important.

Deformation mechanisms in Magnesium include the easy to activate (0001) <1120> basal slip and a more difficult (1010) <1120> prismatic slip, but these both have an <a> type dislocation Burgers vector [Kelley 1968]. C-axis extension and compression require a dislocation Burgers vector in the <c> or <c+a> direction. The most observed deformation mechanism that can accommodate simultaneously both compression and tension is the <c+a> (1122) <1123> 2nd order pyramidal slip. However, the critical resolved shear stress (CRSS) for this slip system is much higher than that of basal and prismatic.

Deformation twinning can also accommodate c-axis extension, and it is in fact an important deformation mechanism in magnesium and other HCP metals. Unlike slip, which is bi-directional, deformation twinning has a polarity. The common {1012} <1011> tensile deformation twinning system in Magnesium can only accommodate c-axis extension [Christian 1995]. Other deformation twinning systems such as the {1011} <1012> compression can accommodate c-axis compression but are slow growing. Despite that, they are a main c-compression deformation mechanism for zirconium at liquid nitrogen temperature instead of pyramidal <c+a> type slip.

Simple compression experiments have been conducted on polycrystalline pure Mg samples cut via electrical discharge machining from extruded and rolled plates. The samples were tested in the through thickness (TT) and in-plane transverse (IPT) directions at room temperature and a strain rate of 10-3 s-1. Figure 9 shows the mechanical behavior of the material while Figures 10, 11, and 12 display, respectively, the initial texture and resulting texture after mechanical testing. Note the effect of twinning on both the mechanical response and texture evolution. Texture was determined via neutron diffraction and represents the bulk texture of the material.
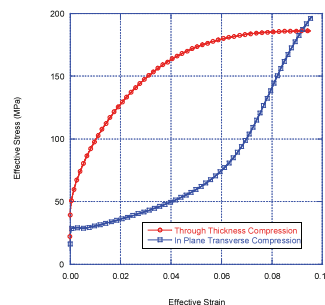
Figure 9. Simple compression of pure polycrystalline Mg showing anisotropy caused by basal texture and twinning. TT compression has the characteristic parabolic shape, while IP compression has a characteristic sigmoidal shape caused by twinning activity.
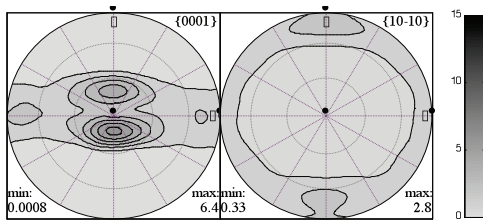
Figure 10. Initial texture of extruded/rolled material. The texture is dominated by the orientation of the basal poles.
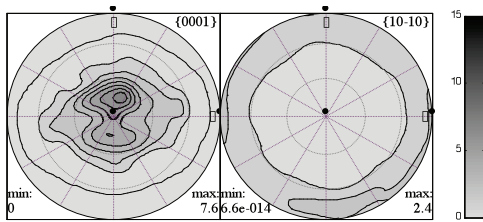
Figure 11. Texture after TT compression of 9.5%. Note the sharpening of the texture.
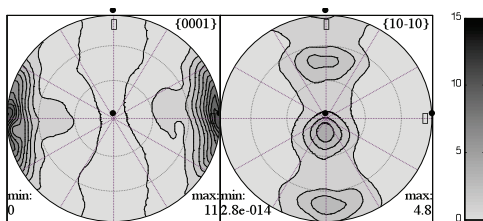
Figure 12. Texture after IPT compression of 9.6%. Note rotation of basal pole.

Additional experiments have been conducted to characterize the material under strain path changes and temperature reloads. These are simple compression experiments at the strain rate range of 1 s^{-1} to 10^{-3} s^{-1} and temperatures varying from liquid nitrogen (77K) to 373K. In the strain path change experiment, an initial compression preload in the TT (IPT) direction is followed by a reload in the IPT (TT) direction. The evolution of the microstructure and the hardening response after the first test affect the response during reload in the normal direction. On the other hand, in the temperature reload experiment, the material is preloaded in the TT (IPT) direction at liquid nitrogen temperature to create twinned structures and subsequently reloaded in the TT (IPT) directions at room temperature.

In all these experiments, the interplay between twin and slip will be examined, and the results will be used for model development. Twinning evolution as a function of strain will be collected from the experimental samples. Twinning evolution will be measured using EBSD and optical metallography as twinned area fraction.

Lab-Scale Extrusion Fixture and Extrusion Experiments

Extruded structural components of magnesium alloys are increasingly being used in the automotive industry due to its good mechanical properties, including low density and high specific strength. However, the extrudability of these alloys is still limited because of their highly anisotropic mechanical behavior originated from their HCP structure. As such, understanding the microstructure-property relationship of these alloys as related to the extrusion process can help to improve their manufacturability.

In this subtask, we are developing a lab-scale indirect extrusion facility to determine the processing-structure-property relation of extruded Mg AZ61 and AM30 alloys. Direct extrusion could be designed by this concept. The main goal is to understand the influence of process parameters (temperature, pressure, ram speed, extrusion ratio) on the microstructure and mechanical properties of extruded material, as well as to generate experimental data for model validation.

The lab-scale indirect extrusion fixture contains (i) a chamber made of two parts (top – bottom), each part with an internal sleeve, and with a clamp holding these parts together; (ii) a replaceable die; and (iii) a base having slotted windows built from a schedule-80 pie. The designed fixture and its set-up on the Instron machine for the extrusion experiments are shown in Figure 13.
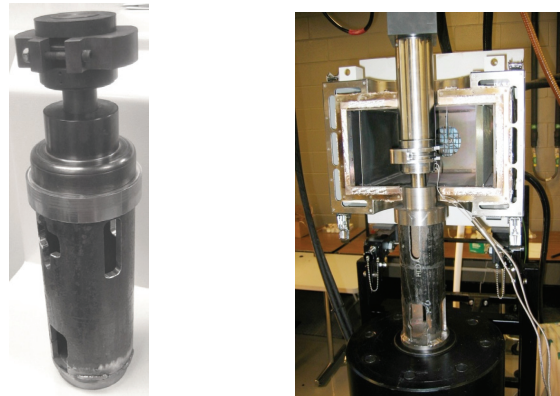
Figure 13. Design of the indirect extrusion fixture and its set-up on the Instron machine.

Experiments (MsSt)

For the experiments, the extrusion process is defined by three processing parameters: extrusion ratio (ER), billet temperature, and the ram speed. A parametric study of the process is being performed by varying these parameters one-at-a-time to see their effect on (i) the metal flow patterns, (ii) the microstructure evolution, and (iii) the mechanical properties of the Mg alloys. A test matrix is given in Table 2. The sample size is 1 1/4" diameter x 1' length, the bearing length is 1/16", and the orifice diameters are 1/4" (ER=25) and 1/8" (ER=100).

Billet Temp.	Ram Speed	ER
454C/850F	5,10 mm/min	25,100
482C/900F	5,10 mm/min	25,100
510C/950F	5,10 mm/min	25,100

Table 2. Lab-scale Extrusion Parameters

Extrusion experiments on Mg AZ61 have been initiated. One specific case is briefly reported here to show the test results that were obtained. This case corresponds to the following processing parameters: ram speed = 10 mm/min, billet temperature = 454°C, and ER = 25. During the extrusion experiments, the billet was compressed 1/2". The magnesium extrudate obtained in this experiment is shown in Figure 14.

Figure 14. Magnesium alloy AZ61 extrudate obtained during preliminary extrusion experiments.

The recorded load-displacement curve from the test is presented in Figure 15. Note that the curve shows an abrupt increase of the load at the beginning, signaling the upsetting stage where the billet is being deformed elastically. The maximum load is reached as soon as the material starts to flow through the die.
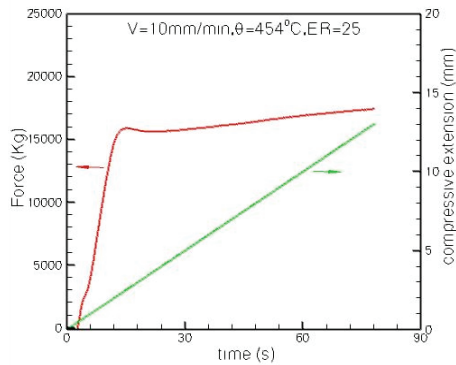
Figure 15. Load-time curve recorded by the Instron machine during the extrusion experiment.

The metal flow patterns and grain structure evolution developed during extrusion are being examined using interrupted extrusion experiments for selected cases from Table 2. Figure 16 show the development of flow lines at different extrusion amounts: 25%, 50%, and 75%. The results are obtained using the following processing parameters: ram speed = 5 mm / min, billet temperature = 454°C, and ER = 25. The flow lines shown in Figure 16 are typical of indirect extrusion. Recall that during this process, the billet remains stationary within the container. As the die progresses during extrusion, material close to the die is scrapped off the container walls and flows into the shear zone of the billet, while the material far away from the die will still be stationary (Figure 16A). As extrusion proceeds, the stagnant material will start to flow, setting up a clear flow patterns typical of the process (Figures 16B and 16C). Note that at the billet-die interface, the material undergoes heavy deformation unlike that seen in direct extrusion.
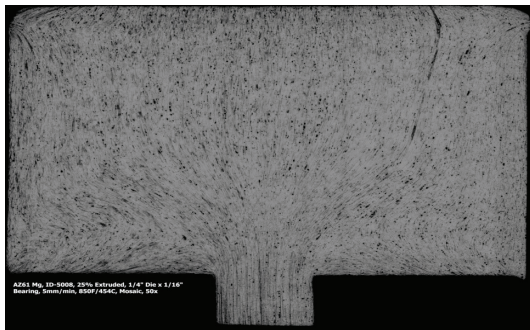
A. Sample extruded at 25%.
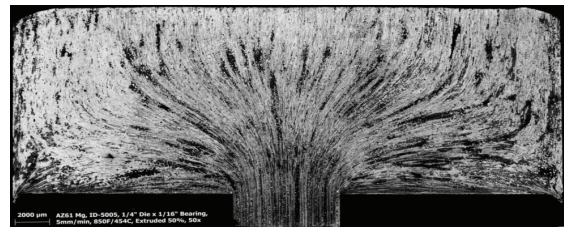
B. Sample extruded at 50%.
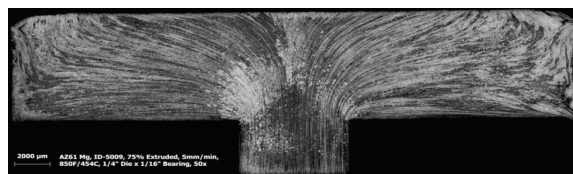
C. Sample extruded at 75%.

Figure 16. Results from interrupted extrusion experiments showing the development of flow patterns in magnesium alloy AZ61.

To characterize the microstructure evolution during extrusion, characterization studies on partially extruded billets are being performed using EBSD. Figure 17 shows the grain structure and pole figures for two material points close to the bearing area obtained from the 50% extruded sample. There is a distinctive grain structure and texture that develop at different material points during the process. In particular, at the center of the billet/extrudate, the material shows a fine grain structure with a strong rod type texture typical of extrusion. On the other hand, close to the die wall the microstructure displays bigger grains and a weaker texture,

features believed to be induced by shear effects. Additional studies are in progress to elucidate the mechanisms responsible for such microstructure changes.

A. Material point close to the die wall.

B. Material point at the center of the billet.
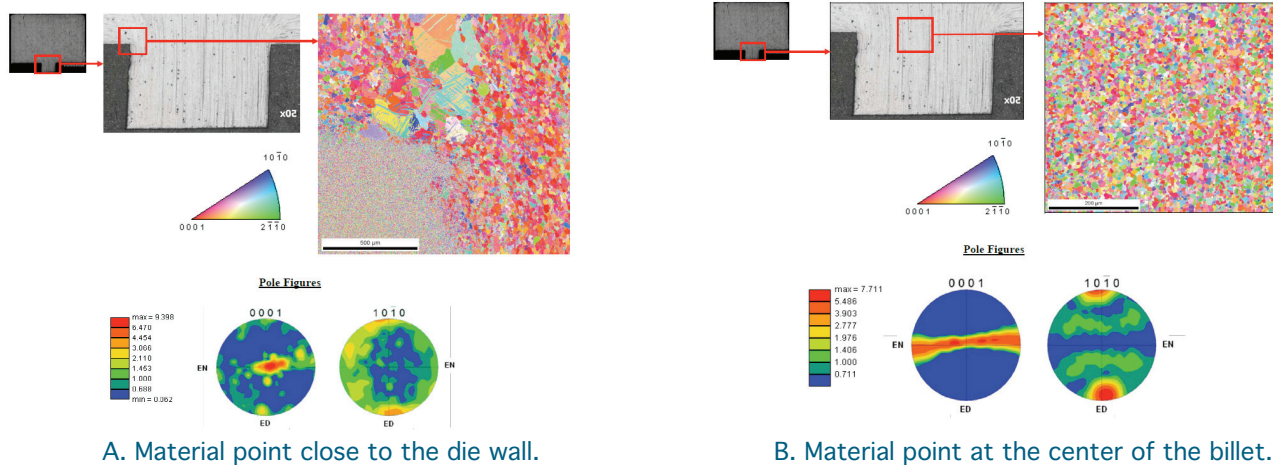
Figure 17. Grain structure and pole figures for two material points close to the bearing area for the case of 50% extruded sample.

On Developing a Multiscale Modeling Framework for Macroscopic ISV Material Models.

A Hierarchical Multi-Scale Materials Modeling Approach

A multi-scale materials modeling approach bridging Moleculare dynamics (MD) and discrete dislocation (DD) to crystal plasticity (CP) in FCC single crystals has been established in this task. In this approach, the material parameters of a dislocation-based hardening law typically used in crystal-plasticity models are numerically computed from DD simulations results. These simulations use dislocation-mobility information obtained from MD computations. A schematic of the bridges connecting these different length scales as well as the simulation tools used at each length scale are summarized in Figure 18. A brief description of the approach follows.
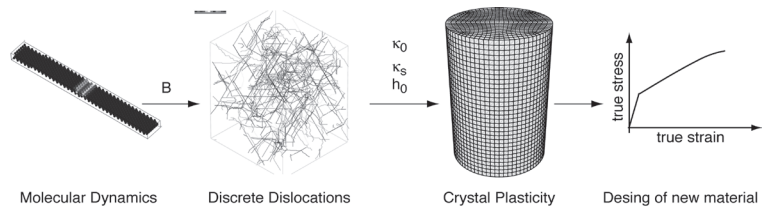
Figure 18. The link between nano-scale, micro-scale and meso-scale in the hierarchical multi-scale modeling approach.

At the crystal plasticity level, the plastic strain in FCC single crystals results from dislocation glide on well-defined lattice planes. A glide system (α) is defined by the dislocation Burgers vector b(α) and the normal vector of the gliding plane n(α). Two expressions are needed to relate the evolution of the plastic shear strain rate (i) to the applied stress on the glide system τ_α and (ii) to the evolution of the slip-system strength κ_α. The flow law relates the shear strain rate to the applied shear stress using the following power-law relationship:

Here, m is the strain-rate sensitivity exponent, taken in the order of 0.05, and $\dot{\gamma}_{0,\alpha}$ is a reference shear strain rate, chosen in the order of 10^{-3} s^{-1}. Assuming that all glide systems harden at the

$$\dot{\gamma}_\alpha = \dot{\gamma}_{0,\alpha} \left(\frac{\tau_\alpha}{\kappa_\alpha} \right)^{1/m}$$

same rate, i.e. $\kappa_\alpha \to \kappa$, one can write the evolutionary law for the strength κ as

Here, κ_s, κ_0 and h_0 are the saturation strength, the initial strength and the initial hardening rate, respectively. In general, these parameters are determined by correlating the model response to

$$\dot{\kappa} = h_0 \left(\frac{\kappa_s - \kappa}{\kappa_s - \kappa_0} \right) \sum_\alpha \dot{\gamma}_\alpha$$

experimental strain-stress curves. However, in this work, they are numerically computed using DD simulations.

At the discrete dislocations level, as the Peierls stress is low in fcc crystals, the velocity v of a single dislocation in these materials can be correlated to a linear form given by

Here, b is the magnitude of the Burgers vector and B is the drag coefficient. This coefficient is determined using MD simulations and the computed value for Al is presented in Figure 19. It is

$$v = \frac{\kappa b}{B}$$

noted that B increases from 2.5×10^{-5} Pa-s to 5.5×10^{-5} Pa-s when the temperature varies from 100K to 500K. Such a range of values for the drag coefficient is in agreement with experimental data.
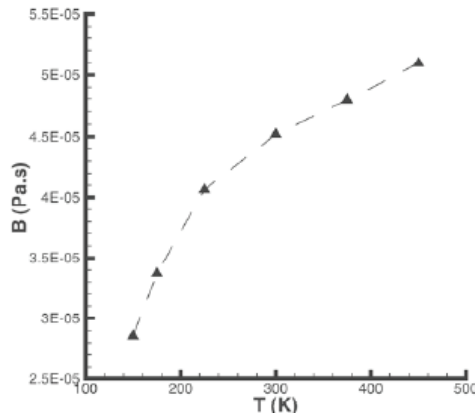
Figure 19. Dislocation drag coefficient as a function of temperature computed from MD.

The above mobility law is used to simulate the tensile test of a dislocation box using DD. A deformation rate of 20 s^{-1} is applied along the [421] axis. The analysis starts with an initial dislocation density of 10^{12} m^{-2}, uniformly distributed over all the slip systems. During the deformation of the simulation box, the plastic strain rate generated by the gliding dislocations equilibrates the applied strain rate. Hence, with $\Sigma \dot{\gamma}_\alpha$ being a constant, the evolution equation of the slip system strength can then be integrated to recover the Palm-Voce equation

The hardening (strength) computed from DD is plotted in Figure 20. The same figure also

$$\kappa = \kappa_s - (\kappa_s - \kappa_0) \exp \left(-\frac{h_0}{\kappa_s - \kappa_0} \sum_\alpha \dot{\gamma}_\alpha t \right)$$

shows the fitted response using the above equation for four sets of parameters. The value of these parameters depends on the time range used to correlate the above equation and the predicted hardening from DD. The initial strength ranges between 3.3 MPa and 3.4 MPa, the initial hardening rate ranges between 29.6 MPa and 35 MPa, and the saturation strength varies between 46.7 MPa and 49.1 MPa.
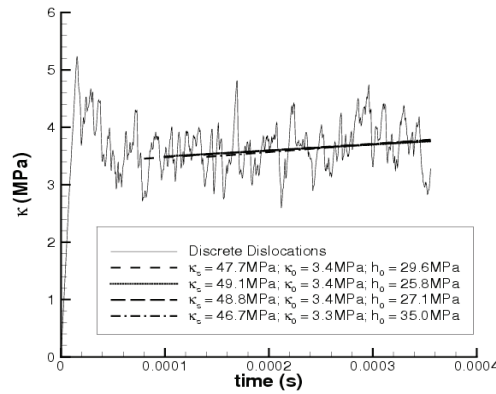
Figure 20. Evolution of hardening as predicted by DD and fit to the integrated evolution equation for the strength κ.

The set of parameters shown in Figure 20 has been used in a crystal-plasticity framework [Marin 2006] to calculate the stress-strain responses of an Aluminum single crystal under compression loading along the [421] direction. The predicted curves are compared to the experimental one [Hughes 2000] in Figure 21. A good agreement between numerical predictions and experimental data is observed for the range of hardening parameters determined from DD. In addition, the deformed mesh at a strain of 0.6 presented in Figure 22 clearly shows that the crystal cross-section ovals during deformation. Note that the experimental cross-section of the deformed crystal agrees well with the predicted deformed shape.
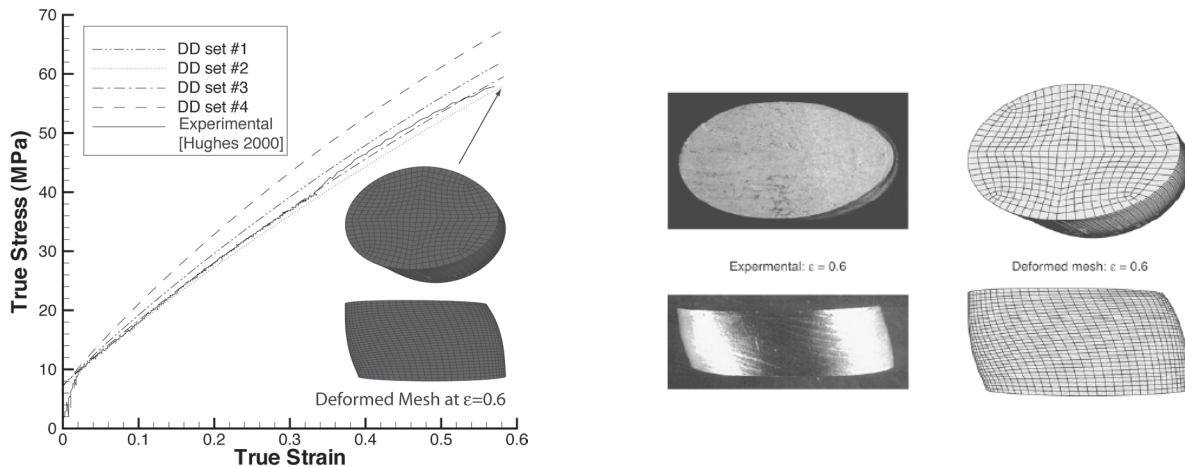
Figure 21. Stain-stress response using the crystal-plasticity parameters calculated by DD.

Figure 22. Experimental versus predicted deformed shape of Al single crystal.

Dislocation Motion in Magnesium by Molecular Static and Molecular Dynamics Simulations

A multiscale modeling framework developed previously for FCC materials [Groh 2008] has shown that the mechanical response of a material can be related to (i) the intersections and reactions between dislocations and (ii) the average dislocation velocity. In an effort to extend such a framework to HCP materials, this work focused on studying the motion of dislocations on basal, prismatic, and <a>-pyramidal slip systems. The goal is to derive a dislocation velocity rule usable for simulation at a higher length scale, i.e., discrete dislocations model. In what follows, we present the dislocation core structures obtained to start the simulations, the quasi-static calculations performed to compute the Peierls stress, and the dynamic calculations to determine the mobility of dislocations.

Structure of the Dislocation Core

Figure 23 shows the core structure of the basal, prismatic, and pyramidal-<a> edge dislocation, obtained after minimization of the potential energy. The core of the basal edge dislocation, Figure 23a, dissociated into two Shockley partials bounding an intrinsic fault I2 according to the reaction,

1

and a distance close to 8b separated the two partials. The core structure of the prismatic edge dislocation, Figure 23b, was undissociated but spreads in the plane ⁻ , while the dislocation core structure of the edge dislocation lying in the pyramidal plane remained undissociated, Figure 23c, independently of the position of the origin chosen for the initial elastic solution. Note that the different core structures obtained will affect (i) the value of the Peierls stress and (ii) the mechanism of motion.

(a)   (b)   (c)
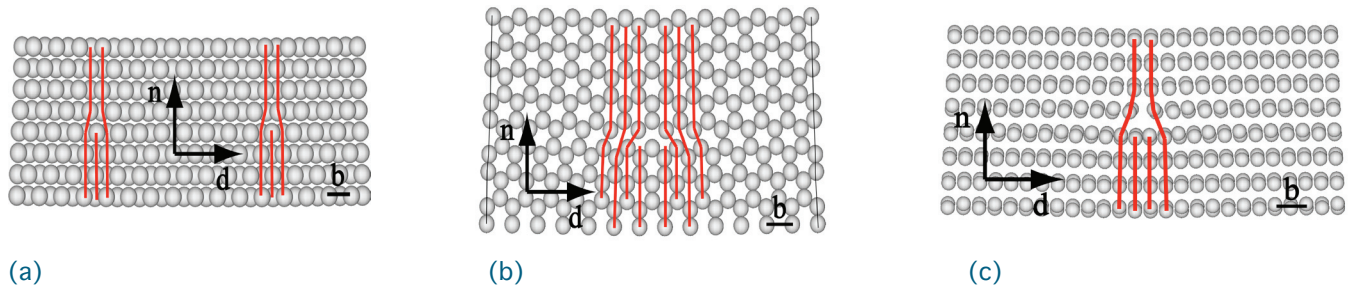
Figure 23. Core structure of <a> -edge dislocation in the (a) basal, (b) prismatic, and (c) pyramidal planes.

Estimation of the Peierls Stress by Molecular Statics

Molecular static calculations were performed to estimate the value of the Peierls stress for edge dislocations lying in the basal, prismatic, and pyramidal slip planes. As a reference, the size of the simulation cell was 100b x 100b along the displacement and normal directions. In order to capture the simple Peierls picture, the dimension of the simulation cell along the dislocation line was restricted to one lattice period, i.e., 0.55 nm, 0.52 nm, and 1.18 nm for basal, prismatic, and pyramidal crystallographic orientation, respectively. A strain increment $\Delta E = 10^{-5}$ applied on the top surface followed by relaxation to the minimum potential energy was repeated until the total strain reached 0.2% for the basal and prismatic crystal orientations and 0.5% for the pyramidal orientation.

Figure 24 shows the strain-stress behaviors calculated for the basal, prismatic, and pyramidal edge dislocations. In the cases of prismatic and pyramidal edge dislocations, we observed that before the dislocation moved, the stress increased linearly with the strain. The corresponding shear modulus was 12.6 GPa, which is in good agreement with the shear modulus reported by

Sun et al. [Sun 2006] (C_{44} = 12.8 GPa). The Peierls stress, which defines the minimum stress needed for moving a dislocation, was reached when the dislocation started to move without increasing the stress. A strong anisotropy between slip systems was observed, Table 3. The obtained Peierls stresses were in agreement with the nature of the dislocation core structures, i.e. a low Peierls stress for a dissociated core and a larger Peierls stress for an undissociated core [Hirth and Lothe 1992].
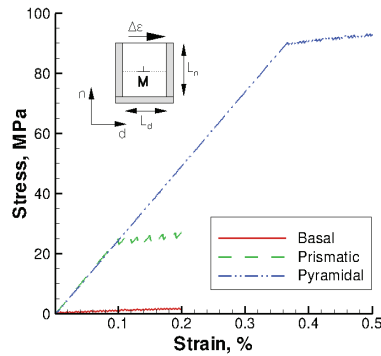
Figure 24. Strain-stress curves obtained by molecular static to model dislocation motion lying on the basal, prismatic and pyramidal slip planes. (ΔE = 10^{-5}, L_n = 100b and L_d = 100b).

The Peierls stresses were not affected by a change of strain increment. Increasing the simulation cell size did not affect significantly the Peierls stress on the basal plane. On the other hand, increasing the cell size from 80b x 80b to 120b x 120b, decreased the Peierls stress on the prismatic slip plane from 25.5 MPa to 23.7, respectively. The length of the edge dislocation lying in the prismatic plane (lengths ranging from one lattice period to thirty lattice periods were tested) did not affect its Peierls stress.

	Experimental data (MPa)	This Study (MPa)	
		Liu et al. (1996)	Sun et al. (2006)
Basal	0.52 (a)	14	0.35
Prismatic	39.2 (b)	22	23.7
Pyramidal	105* (c)	24	90-92

Table 3. Peierls stress (MPa) for basal, prismatic, and pyramidal slip system in Mg calculated by molecular statics (a: [Conrad 1957]; b: [Reed-Hill 1957]; c: [Staroselsky 2003]; *numerical value)

As reported in Table 3, the calculated Peierls stress for each systems are in a good agreement with experimental data. To determine the sensitivity of the Peierls stresses to the particular potential used, similar calculations were performed using the EAM potential proposed by Liu et al. [Liu 1996]. Although the core structure for the edge dislocations were similar to the one reported above, the corresponding Peierls stresses, Table 3, were not in agreement with both the experimental data and the value calculated using the potential from [Sun 2006].

Dislocation Mobility by Molecular Dynamics

MD simulations have been performed to determine the velocity of dislocations lying on the basal and prismatic slip planes. For comparison purposes, the velocities of edge/screw dislocations lying on these slip planes are plotted in Figure 25 as a function of the applied stress for a temperature of 100K.
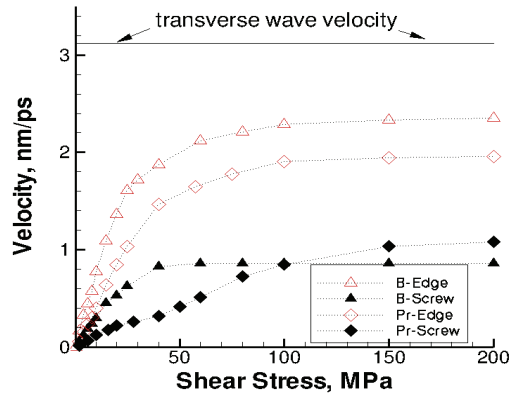
Figure 25. Dislocation velocity for an edge and screw dislocations lying on the basal (B) and prismatic (Pr) slip planes.

Two types of anisotropy were observed: (i) anisotropy of the velocity related to the dislocation character and (ii) anisotropy of the velocity related to the slip plane.

Before the dislocation velocity saturates, the dislocation velocity increases linearly with the stress for a dislocation lying on either the basal or the prismatic slip planes. At 100K, the drag coefficients are 4.7×10^{-6} Pa.s, and 1.3×10^{-5} for edge and screw dislocations on the basal slip plane, respectively, while 7.7×10^{-6} Pa.s and 3.7×10^{-5} Pa.s for edge and screw dislocations lying on the prismatic slip plane respectively. In addition, as the Peierls barrier is higher in the prismatic than in the basal slip planes, the lower velocity for a dislocation lying in the prismatic plane compared to the velocity of a dislocation lying in the basal plane is the consequence of a stronger interaction between the dislocation and the Peierls barrier. For example, at 50 MPa, screw dislocations moved with a speed of 0.84 nm/ps and 0.41 nm/ps in the basal and prismatic slip planes, respectively, while edge dislocations moved with a speed of 2 nm/ps and 1.5 nm/ps in the basal and prismatic slip planes, respectively.

Summary

The effect of the (i) temperature and (ii) the dislocation character on the dislocation mobility was investigated on each slip systems. The Peierls stresses for edge and screw dislocations moving on either the basal, prismatic, or pyramidal slip planes were also determined, and a good agreement with experimental data from the literature was found.

From the dynamics calculations, we found a strong anisotropy of the dislocation velocity related (i) to the dislocation character and (ii) to the slip systems. In general, edge dislocations lying on the basal slip plane are moving two times faster than screw dislocations from the same slip system. On the other hand, edge dislocations lying on the prismatic slip plane are moving five times faster than screw dislocations gliding on the same slip plane. In addition, dislocations moving on the basal are two-three times faster (edge-screw) than dislocations from the prismatic slip system. The numerical dislocation velocities obtained during this study were correlated to a dislocation mobility rule following a viscous drag form, and the corresponding drag coefficients calculated at 100K are reported in Table 4.

	Edge	Screw
Basal	4.7×10^{-6}	1.3×10^{-5}
Prismatic	7.7×10^{-6}	3.7×10^{-5}
Pyramidal	8.0×10^{-5}	Not stable

Table 4. Value of the drag coefficient (Pa.s) for edge/screw dislocations lying on the basal, prismatic, and pyramidal slip planes at 100K

Numerical Implementation of Deformation Twinning in a Crystal Plasticity Model

Mg single crystals and associated polycrystalline alloys are characterized by highly anisotropic mechanical behavior [Kelly 1968; Nave 2004; Barnett 2007], with twinning being an important deformation mechanism at low temperatures. Hence, realistic modeling of Mg and its alloys requires accounting for deformation twinning in the constitutive equations. Over the last two decades, an extensive effort has been made to incorporate twinning deformation in polycrystalline modeling. The main assumption common to most models is to consider that a critical resolved shear stress exists to activate twinning, and, therefore, deformation twinning is considered as a polar pseudo-slip. Such assumption is also considered in our development.

The aim of the work was to implement deformation twinning in an existing crystal plasticity framework. As a benchmark to validate the implementation, we apply the model to reproduce the anisotropic behavior of a magnesium single crystal under plane stain compression. The subsections below describe the implementation of deformation twinning in the crystal plasticity framework and in the numerical results obtained.

Modeling Framework

The crystal plasticity framework developed in [Marin, 2006], where crystallographic slip is the only deformation mechanism, has been extended to account for deformation twinning. This development follows closely the work of [Kalidindi 1998]. This section presents solely the main aspects of the framework that need modifications to account for twinning.

The multiplicative decomposition of the local deformation gradient F can be written as the following; see Figure 26:

$$F = F^e F^p \quad \text{with} \quad F^e = V^e R^e$$

Here, F^e is the local elastic deformation gradient, decomposed in the elastic stretch, V^e, and lattice rotation, R^e, while F^p represents the local plastic deformation gradient due to both slip and deformation twinning.

In configuration $\bar{B}$, the plastic velocity gradient, $\bar{L}^p$, is written as the sum of the slip contribution in the non-twinned region and the twin contribution, and is given by

$$\bar{L}^p = \left(1 - \sum_{\beta}^{N^{tw}} f^{\beta}\right) \sum_{\alpha}^{N^{sl}} \dot{\gamma}^{\alpha} \bar{s}^{sl,\alpha} \otimes \bar{m}^{sl,\alpha}$$
$$+ \sum_{\alpha}^{N^{tw}} \delta \dot{f}^{\alpha} \gamma^{tw} \bar{s}^{tw,\alpha} \otimes \bar{m}^{tw,\alpha}$$

where $\dot{\gamma}^{\alpha}$ is the plastic shearing rate on the a-slip system that is defined by the unit vectors ($\bar{s}^{sl,\alpha}, \bar{m}^{sl,\alpha}$), $\dot{f}^{\alpha}$ is the rate of volume fraction of the α-twin system which is represented by the unit vectors ($\bar{s}^{tw,a}, \bar{m}^{tw,a}$), γ^{tw} is the constant shear strain associated with twinning, and δ is a material constant.
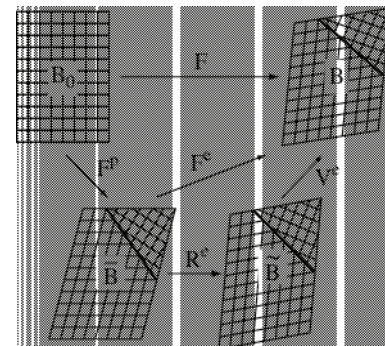
Figure 26. Kinematics of elasto-plastic deformation of single crystals deforming by crystallographic slip and twinning.

Note that the previous equation does not consider the slip system activity in the twinned region. This implies that the disorientation between the twin and the parent stays constant during the deformation. Also, this equation introduces the rate of the volume fraction on each a-twin system and the total volume fraction of twins in the formulation. The evolution equation of the twin volume fraction is represented by a power-law expression

$$
\begin{cases}
\dot{f}_v^\alpha = \dfrac{\dot{\gamma}_0}{\gamma^{tw}}\left(\dfrac{\tau^\alpha}{\kappa^{tw,\alpha}}\right)^{1/m} & \text{if}\left(\tau^\alpha>0\right)\text{and}\left(\sum_\alpha f_v^\alpha \leq f_v^{sat}\right) \\[2mm]
\dot{f}_v^\alpha = 0 & \text{if}\left(\tau^\alpha \leq 0\right)\text{or}\left(\sum_\alpha f_v^\alpha > f_v^{sat}\right)
\end{cases}
$$

where τ^α and $\kappa^{tw,\alpha}$, represent, respectively, the resolved shear stress on the α-twin system and the associated twin resistance. Note that the saturation of the twin volume fraction is controlled by the parameter f_v^{sat}. The hardening of the twin system is modeled by the expression

$$
\kappa^{tw} = \kappa^{tw}{}_0 + h_{tw}\left(\sum_i^{N^{tw}} \dfrac{\dot{\gamma}^i}{\dot{\gamma}_{ref}}\right)^d
$$

where $\kappa_0{}^{tw}$ is the twin critical resolve shear stress, $\dot{\gamma}_{ref}$ was a reference shear rate set up to 1 s^{-1}, and h_{tw} and d are material parameters.

Finally, slip system hardening is modeled by an extended Palm-Voce rule [Salem, 2005] for each slip-system family: basal-<a>, prismatic-<a> and pyramidal-<c+a>,

$$
\dot{\kappa}_{sl}^i = h_{sl,s}^i(f)\left(\dfrac{\kappa_{sl,s}^i(f)-\kappa_{sl}^i}{\kappa_{sl,s}^i(f)-\kappa_{sl,0}^i}\right)^{N^{sl,i}}\sum_k |\dot{\gamma}^k|
$$

$$
\text{with}
\begin{cases}
h_{sl,s}^i(f) = h_{sl,s0}^i\left(1+C\sum_\beta f^\beta\right)^b \\[3mm]
\kappa_{sl,s}^i(f) = \kappa_{sl,s0}^i + \kappa_{pr}\left(\sum_\beta f^\beta\right)^{0.5}
\end{cases}
$$

where $h_{sl,s0}^i$, $\kappa_{sl,0}^i$, $\kappa_{sl,s0}^i$ are material constants, and the parameters C, κ_{pr}, and b define the coupling between slip and twinning.

The developed framework has been implemented in both a material point simulator and an ABAQUS user material subroutine. These implementations have been used to determine the stress-strain behavior of magnesium single crystals under plane strain compression.

Numerical Results

Kelley and Hosford [Kelley 1968] have conducted deformation studies at room temperature on magnesium single crystals. These crystals were oriented to suppress shear on the easily activated basal slip systems and were deformed by plane strain compression. Table 5 presents the six predefined orientations, and the experimental results are given in Figure 27a. Note that, for orientations E and F, twinning was observed at the beginning of the deformation to accommodate the compression perpendicular to the unconstrained c-axis. Once twinning was virtually completed, deformation continued by banding.

Table 5. Direction of the compressive load and constraint for the plane strain compression testing

Id	Compression	Constrain	Euler Angle
A	$<0001>$	$<1\bar{0}>$	(150, 0, 0)
B	$<0001>$	$<1\bar{1}>$	(240, 0, 0)
C	$<1\bar{0}>$		(0, 90, 30)
D	$<1\bar{1}>$		(0, 90, -60)
E	$<1\bar{0}>$		(-90, 90, 30)
F	$<1\bar{1}>$		(90, 90, -60)

Based on the analysis of the slip/twin activity for each orientation, the hardening parameters of the model were calibrated with the experimental data as follow:

- Orientation C gives the material parameters for the prismatic slip system.

- Orientation A gives the material parameters for the pyramidal slip system.

- Orientation E gives the materials parameters for the twinning activity.

- The coupling parameters between slip and twins, C, κ_{pr}, h_{tw}, b and d were obtained using a parameter sensitivity study.

The computed stress-strain behaviors for the six orientations are given in Figure 27b. Note that the trends observed in experiments are well predicted by the model.

(a)   (b)
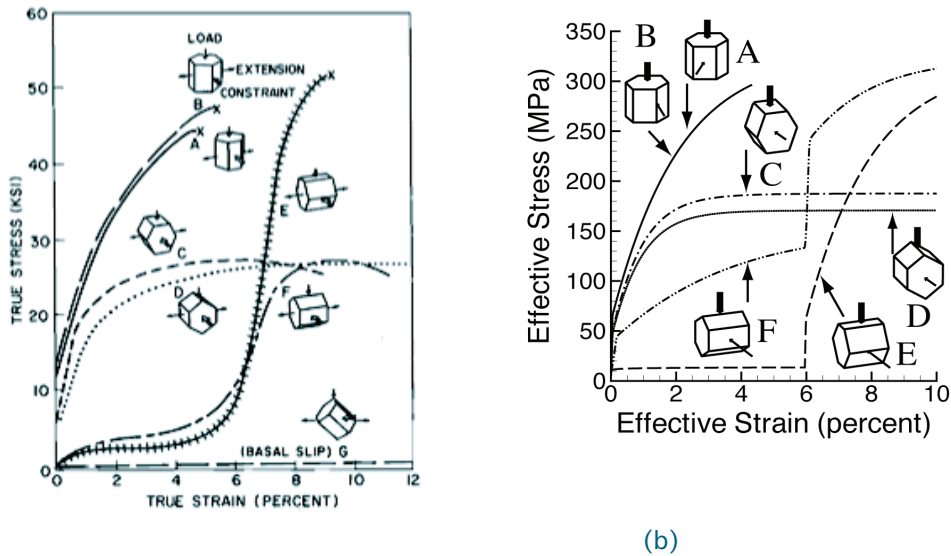
Figure 27. Stress vs strain in pure magnesium single crystal for the orientations given in Table 5: (a) experimental results [Kelley 1968], (b) predictions from the model.

Summary

In this work, an existent crystal plasticity framework was extended to account for deformation twinning, where twins were considered as pseudo-dislocations. The framework was based on the multiplicative decomposition of the local deformation gradient. One of the main assumptions of this modeling approach is to assume a constant orientation between the twinned region and the parent material. This assumption implies that no slip activity occurs in the twinned material. The model also assumes a power-law type for the evolution of the twin volume fractions and a constant hardening on both the slip and the twin systems.

The crystal plasticity model was applied to predict stress-strain curves under plane strain compression of Mg single crystals with six predefined orientations. Deformation twinning was only visible when the loading was applied perpendicularly to the unconstrained c-axis. The predicted stress-strain curves agreed well with data from the open literature.

Void Growth in Magnesium: A Molecular Dynamics Study

Extensive computational research has been devoted to analyze void growth and coalescence in face centered cubic (fcc) metals under various loading conditions using molecular dynamics simulations. Prismatic [Rudd 2002; Seppala 2004; Lubarda 2004] and shear loops [Lubarda 2004; Belak 1998; Traiviratana 2008] have been postulated as mechanisms to transfer matter away from voids.

As reported by Groh et al. [Groh 2009], dislocation properties such as core structures, Peierls stresses and dislocation velocities are highly anisotropic in magnesium. Furthermore, in addition to dislocation deformation, twinning deformation is an important mechanism to accommodate plastic deformation in magnesium alloys at low and ambient temperature. This mechanism is not typically present in fcc metals. The aim of the present study is to investigate the deformation mechanisms related to void growth in magnesium single crystal under different loading conditions using molecular dynamics simulations.

Simulation Setup

Molecular dynamics simulations using LAMMPS were performed to simulate void growth and coalescence in magnesium. The simulations, performed using the EAM potential [Sun 2006], used a cubic specimen with average edge dimension L containing an initial spherical void of radius R located in the center of the specimen. The initial void volume fraction was set to 0.4%, and several void radii ranging from 5Å up to 30Å were simulated.

Periodic boundary conditions were applied along the faces parallel to the loading direction. System trajectories consistent with the canonical ensemble were used to deform the specimen using the Nose and Hoover temperature thermostat. Specimens were deformed with an engineering strain rate between $10^8 s^{-1}$ and $10^{10} s^{-1}$ at five different temperatures ranging from 50K up to 500K.

The evolution of the void volume was calculated using a numerical tool developed by the molecular biology community [Perrot 1992] to study the structure and function of molecules. The technique is based on the idea of rolling a probe sphere over a molecule to generate a smooth-outer contour, where the radius of the probe sphere is chosen to represent a solvent molecule. Sanner et al. [Sanner,1996] extended this technique and proposed a fast and robust algorithm called maximum speed molecular surface (MSMS). In this study, MSMS was used to keep track of the rate of change of the void volume fraction (porosity) and the number density of voids.

Numerical Results and Discussion

Uniaxial loading was performed in both [0001] and [11-20] directions. The initiation of the plastic flow occurred at the void surfaces, and snapshots extracted from the simulations performed at 100K and for a strain rate of 109 /s are given in Figure 28A and 28B for [0001] and [11-20] loading directions.
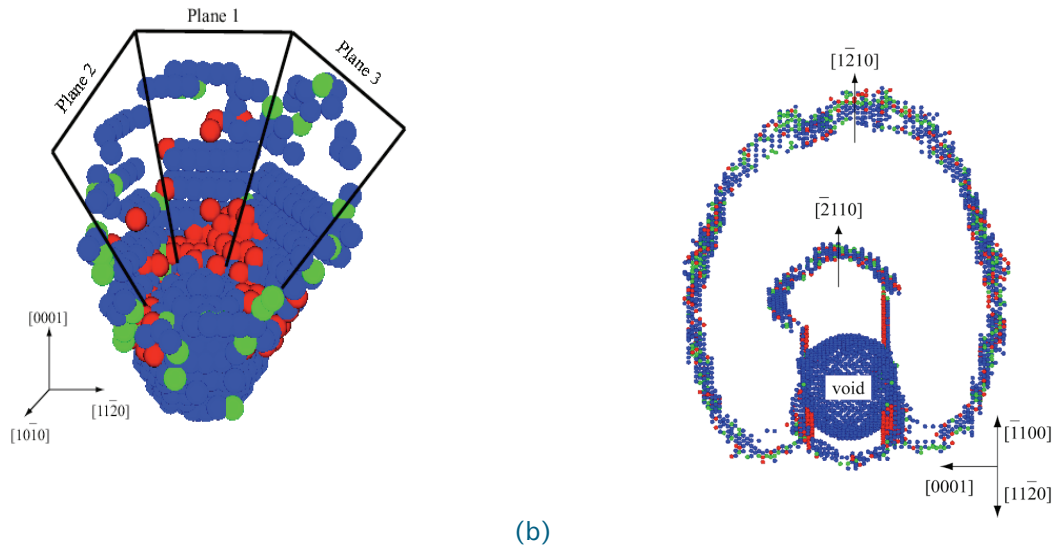
Figure 28. Initiation of the plastic flow at the void surface for loading along (A) [0001] and (B) [11-20] directions.

As the load was applied perpendicular to the basal plane along the [0001] direction, partial dislocations with Burgers vector   were nucleated at the void surface and propagated in   twin planes (three twin planes referred by P1, P2, and P3 as shown in Figure 1A). Once the partial dislocations were nucleated at the void surface, they propagated away from the void leading to the formation of twin boundaries, in accordance with the growth of the twin boundary tip presented by Hirth and Lothe [Hirth 1992]. However, the reaction between P1 and P3 lead to a new plane that is not a twin boundary plane.

Contrary to what happened during the [0001] testing, the initiation of the void growth occurred by nucleation and emission of dislocation shear loops in the prismatic slip planes during the tensile test along the [11-20] direction as represented in Figure 28B. Such a mechanism of void growth is in agreement with the previous work of Rudd et al. [Rudd 2007] carried out on metal with fcc crystal structure. Dislocations are nucleated on four prismatic slip planes. Once these dislocations started moving, shear loop were formed on the prismatic slip plane as reported in Figure 28B, with the normal to the (10-10) slip plane oriented perpendicular to the plane of the paper. In agreement with our previous work related to the anisotropy between (i) slip systems and (ii) dislocation characters [Groh 2009], the shear loop with Burgers' vector [1-210] in the slip plane (10-10) extended along the screw directions.

To model damage evolution at the macroscopic level, Horstemeyer et al. [Horstemeyer 2000] proposed a continuum damage formulation, Φ , that includes void nucleation, η , void growth, v, and void coalescence, c, using a multiplicative decomposition written as

$$\Phi = \eta vc.$$

In that model, void nucleation occurs principally at the internal interfaces (matrix/particle interfaces), while the intervoid ligament distance controls the coalescence. In the case of the present study, homogeneous void nucleation must replace heterogeneous void nucleation as the material of reference is a magnesium single crystal, and, therefore, no internal interfaces were considered.

Based on the multiplicative decomposition framework given by the previous equation, the evolution of void volume fraction resulting from the growth of the initial void, the evolution of the total void volume fraction (damage), and the number of nucleated voids were monitored during the deformation. The growth of the initial void and the total damage evolution are plotted in Figure 29A for a specimen deformed with a strain rate of 10^9 /s at 300K. In addition, the total number of voids and the number of voids of small dimensions are plotted in Figure

29B with respect to the engineering strain. From Figure 29A, one can observe that the damage evolution is completely represented by the growth of the initial void up to 4 % strain. On the other hand, after 4% of deformation, the initial void growth only represents a small contribution to the damage; the void growth contribution to damage increased from 0.4% up to 1% while the total damage increased from 0.4% up to 4%. The sharp increase of damage observed between 4% and 4.5% (see Figure 29A) was correlated to the increase of the number of voids in the material at the same strain level. Hence, the void nucleation mechanism was dominant. For example, the number of voids rose from one (the initial void) to thirty-two, while twelve of them were of small dimensions less than the size of the original void. Once all the voids were nucleated in a very short period of time, they coalesced, and the void total saturated around five. To summarize, the evolution of the damage progresses according to the following:

- Stage 1: growth of the man made void,

- Stage 2: homogeneous nucleation of voids and coalescence of the nucleated voids,

- Stage 3: fracture of the specimen.
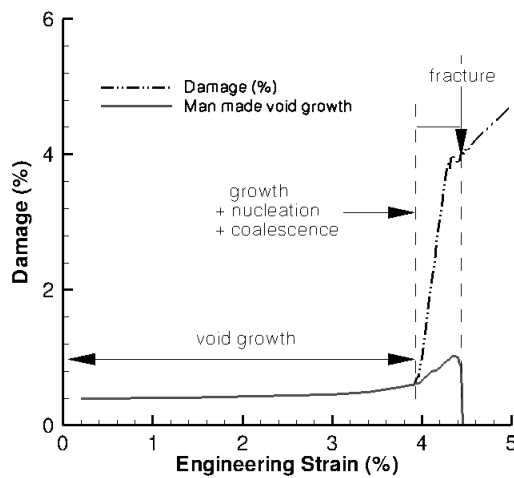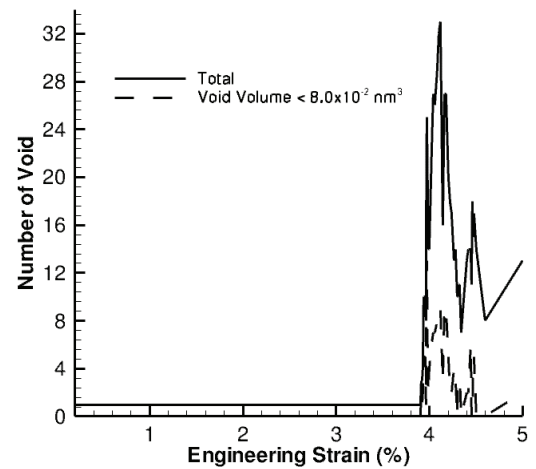
(a)   (b)

Figure 29. Decomposition of the damage evolution based on a macroscopic continuum concept for damage which defines the void volume fraction as the void volume over the total volume: (A) growth of the initial void (pore) and total void damage and (B) the total number of voids in the specimen and number of voids with a volume lower than 0.008 nm3.

The evolution of the von Mises stress, damage and void volume fraction as a function of the engineering strain were analyzed. The following general trends were observed:

- The von Mises stress decreases with (i) decreases in the strain rate or (ii) increases in the temperature or (iii) increases in the void radius,

- The damage increases with (i) decreases in the strain rate or (ii) increases in the temperature or (iii) increases in the void radius.

Modeling the Response of Pure Polycrystalline Magnesium Using Crystal Plasticity

The visco-plastic self-consistent (VPSC) model developed by Molinari [Molinari 1987] and implemented by Lebensohn and Tomé [Lebensohn 1993] is used to model the mechanical behavior and texture evolution of Magnesium. This is a crystal plasticity framework that uses a "visco-plastic" material response with a "self-consistent" averaging scheme. It was originally used to model deformation mechanisms for low symmetry materials such as HCP-type crystalline structures. The code models a polycrystal aggregate subjected to loading and predicts the plastic deformation, texture, and grain shape evolution. The VPSC framework is the connection between the individual single crystal constitutive hardening model, and the mechanical response and texture evolution of the polycrystal aggregate.

The constitutive model incorporates both slip and deformation twinning. We used the composite grain twinning model and a dislocation density based constitutive hardening model described by Beyerlein [Beyerlein 2008]. The model is temperature and strain rate dependent.

It is assumed in this model that slip systems are hardened through the combination of a dislocation forest, dislocation debris, or substructure and Hall-Petch type mechanisms:

$$\tau_c^\alpha = \tau_0^\alpha + \tau_{\text{forest}}^\alpha + \tau_{\text{substructure}} + \tau_{\text{HP}}^s$$

where

$$\tau_0 = \text{initial CRSS}$$

$$\tau_{\text{forest}}^\alpha = b^\alpha \chi \mu \sqrt{\rho^\alpha}$$

$$\tau_{\text{substructure}}^\alpha = k_{\text{substructure}} \mu b^\alpha \sqrt{\rho_{\text{substructure}}}$$
$$\log\left(b^\alpha \sqrt{\rho_{\text{substructure}}}\right)^{-1}$$

$$\tau_{\text{HP}}^s = \mu \text{HP}^\alpha \sqrt{\frac{b^\alpha}{d_g}} \quad s \in \alpha \quad \text{without twins}$$

Dislocation density is evolved through the following evolution equation:

$$\frac{\partial \rho^\alpha}{\partial \gamma^\alpha} = \frac{\partial \rho_{\text{generation}}}{\partial \gamma^\alpha} - \frac{\partial \rho_{\text{removal}}}{\partial \gamma^\alpha} = k_1^\alpha \sqrt{\rho} - k_2^\alpha(\dot{\varepsilon}, T)\rho^\alpha$$

The temperature and rate dependence are introduced as follows:

$$\frac{k_2^\alpha(\dot{\varepsilon}, T)}{k^\alpha} = \frac{\chi b^\alpha}{g^\alpha}\left(1 - \frac{kT}{D^\alpha b^3}\ln\left(\frac{\dot{\varepsilon}}{\dot{\varepsilon}_0}\right)\right)$$

where D is the drag stress and g is the activation energy.

The model has been applied to predict the response of polycrystalline, pure magnesium compressed through the thickness and in-plane transverse directions. Figure 30 presents the initial texture used in the simulations. The results of the calculations are presented in Figures 31 though 34. Figures 31 and 33 displays the experimental and predicted stress-plastic strain response while Figures 32 and 34 shows the experimental and predicted texture after 10% strain. The predicted response agrees well with experiments.

The model will also be used to predict the experimental data from the strain path changes and temperature reloads described in previous sections.
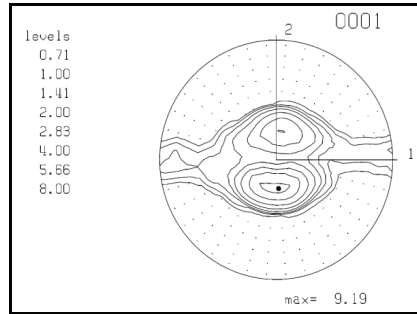
Figure 30. (0001) pole figure of a typical untested specimen revealing a primarily basal texture with some additional off-axis texture.
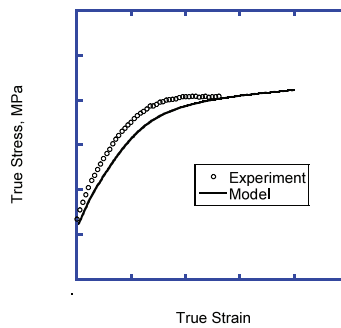
Figure 31. Through thickness compression showing experimental and predicted stress/plastic-strain curves.
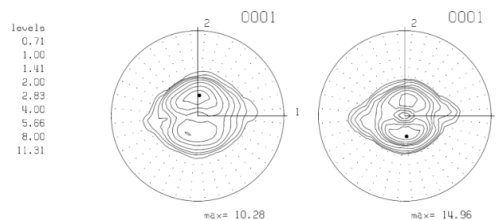
Figure 32. (0001) pole figures (a) obtained experimentally by neutron diffraction and (b) predicted by VPSC after ~9% through thickness compression.
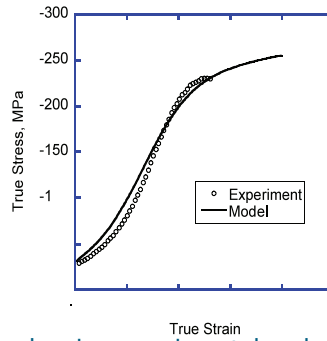
Figure 33. In-plane transverse compression showingexperimental and predicted stress/plastic-strain curves.
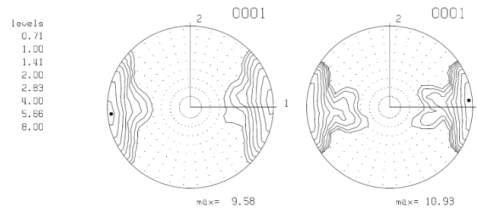
Figure 34. (0001) pole figures (a) obtained experimentally by neutron diffraction and (b) predicted by VPSC after ~9% in-plane transverse compression.

Finite Element Modeling of the Extrusion Process

Extrusion is a metal forming process used to produce long complex profiles with high tolerance and surface quality. Unlike other material forming processes, such as forging and rolling, profile extrusion process usually has complex material flow patterns accompanied with extremely large and severe plastic deformation. Such a feature puts rigorous requirements on the numerical tools used to simulate the extrusion process.

Finite elements meshes in which grid points coincide with the material points (Lagrangian approach) are usually distorted severely and must be re-meshed frequently (adaptive meshing), increasing the CPU time for a simulation. On the other hand, the Eulerian approach avoids re-meshing as the finite element mesh is fixed in space, and, hence, it does not move with the material. This feature avoids strong mesh distortions in the zones of severe deformation. As such, this method has a significant potential for simulating the extrusion process. Besides, this method can be combined with an ALE (Arbitrary Lagrangian-Eulerian) approach to account for moderate mesh adjustments following the shape of the deformed domain.

For the extrusion simulations in this project, we use HyperXtrude, a commercial finite element code developed specifically to model the non-isothermal material flow during metal extrusion. The code uses an Eulerian formulation of the fundamental differential equations that govern flow and heat transfer of incompressible viscous fluids. The code also includes an ALE approach to make mesh adjustments to the free surface of the extrudate in order to satisfy the zero normal velocity condition. The code has the capability to simulate very complex 3-D profile shapes using porthole dies, multiple pockets, and the like.

Preliminary simulations of the lab-scale experiments in HyperXtrude assumed a steady state extrusion process. The finite element model is built from the material volume (control volume) inside the extrusion fixture, see Figure 35.
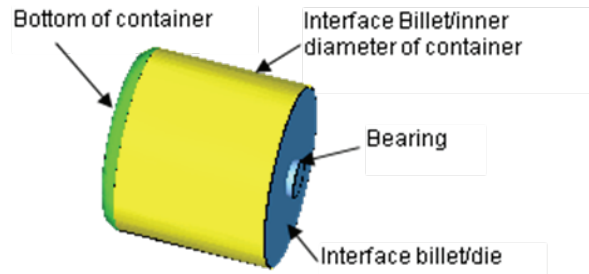
Figure 35. Material volume inside tooling of extrusion fixture.

The finite element mesh of the problem domain is built with HyperMesh (a pre-processor for HyperXtrude) using tetrahedral elements; see Figure 36. Note that the geometry in the numerical model has been slightly modified by removing the curvature at the dummy-block interface. This change did not affect the material flow through the die. The test conditions simulated were: billet temperature = 450C, ram speed = 5 mm/min, extrusion ratio = 25, and bearing length = 1/16". Appropriate boundary conditions were specified along the different surfaces of the model. The material was assumed to be 1100 aluminum alloy following a Sine Hyperbolic Inverse flow stress model. The material parameters were obtained from the HyperXtrude database.
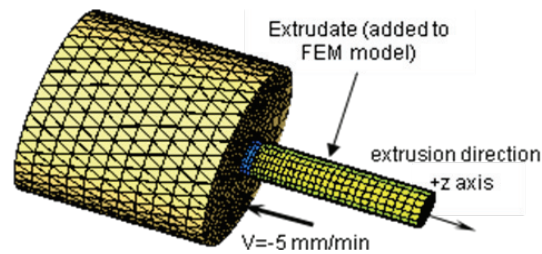
Figure 36. Eulerian finite element model of lab-scale extrusion experiments.

The results of the simulation are presented in Figure 37. Figure 37a displays the velocity contour plots in the cross section of the model domain. Note that material points in the billet, which are initially fixed (indirect extrusion), start to move towards the die orifice, setting up the flow patterns typically found in metal extrusion. Figure 37b shows the temperature profiles along the surface of the 3D model. Note that as the material flows through the die, the temperature increases from 450°C (initial billet temperature) to 454°C at the extrudate. Also note that the temperature distribution is axi-symmetric.
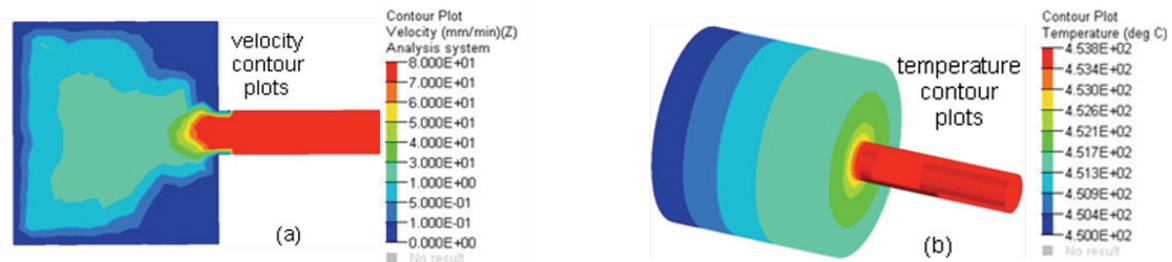
Figure 37. Initial results of HyperXtrude simulation of the indirect lab-scale extrusion experiments.

Material Database for Magnesium Alloys

Rolling Experiments of Mg Alloys

Pilot-scale rolling experiments on a number of Mg alloys produced by MEL Inc were performed at ORNL. Besides of generating information for the material database, this study will help to develop a wrought Mg alloy and/or processes for the cost-effective production of Mg sheets which are both economical and formable enough for practical applications in vehicle structures. Activities were concentrated in two areas: (i) evaluating the feasibility of using innovative roll processing together with lower-cost alloyed ingots to reduce the total cost of sheet materials and (ii) developing a basic understanding of the mechanisms of deformation and recrystallization in order to develop inexpensive alloys for applications in the transportation industry.

It is worth noting that previous work centered on demonstrating the feasibility of utilizing infrared processing to enable continuous processing of wrought Mg alloys as one part of cost reduction. This work, on the other hand, is centered on alloy development to produce a lower-cost wrought alloy with properties close to those of AZ31.

At approximately \$4/lb for finished sheet, cost is one impediment to wider use of Mg in transportation applications. Possible ways to reduce cost mostly center on reducing the number of processing steps to the point of continuous processing, and some potential cost savings in the composition elements and methods associated with the initial alloying of ingots. Previous studies of infrared or plasma-arc-lamp reheats have shown potential to facilitate continuous-strip rolling operation. Also, a more thorough understanding of recovery and recrystallization will allow optimization of any chosen process. These innovations coupled with continuous casting should result in significant cost savings.

Suggestions of a rolling schedule for a lab-sized, 6-inch mill, and experimental conditions were made by MEL Inc and were used as a starting point. MEL cast practice slabs with representative compositions of the alloys to be studied. The process developed and then used for subsequent tests consists of the following: 1) Overnight annealing at 400°C. The minimum times and temperatures necessary for this step have not been investigated; 2) Slabs were then covered with 1.1-mm-thick sheets of stainless steel. The sheets were oxidized and sprayed with dry film graphite lubricant. The rolls are cold so the stainless steel sheets help to retain heat; 3) Hot rolling at 400°C with 10% reductions per pass and 10-min reheat between passes down to approximately 1.5 mm; 4) One half of the sheet was saved and the second half was cold rolled 10%. Figure 38 shows a successful hot-rolled sheet of alloy 129.

Figure 38. MEL Mg alloy #129 as hot rolled at 400°C clad to a thickness of 1.5 mm.

Tensile stress and elongation at failures are tabulated in Tables 6 and 7. Results from comparison AZ31 specimens from some of our previously published papers are also tabulated in Table 6. These comparison results used the same flat dog-bone specimen size with a 25-mm gage length and the same strain rate of 10^{-3}/sec. Figure 39 presents a sample of the experimental stress-strain curve obtained during the tensile tests.
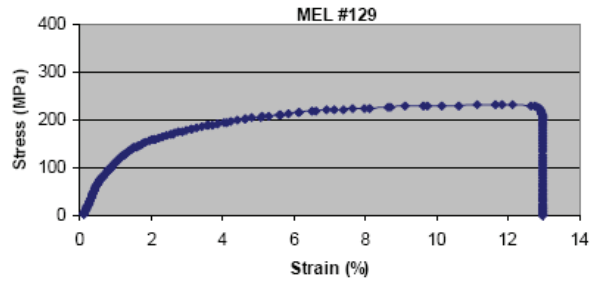
Figure 39. Tensile test data for MEL Mg alloy #129. Specimen axis is along the rolling direction.

Optical metallography was done on all specimens; however, grain-size was difficult to determine on many of the hot-rolled and cold-rolled specimens due to the very fine microstructures present (see Figure 40 for a sample). The incomplete data were not tabulated. One alloy for which the metallography was adequate was alloy 113 with American Society for Testing and Materials (ASTM) grain sizes between 8 and 9, approximate grain diameters of 20 μm. It is vital to have accurate grain-size measurements to determine trends in mechanical properties.
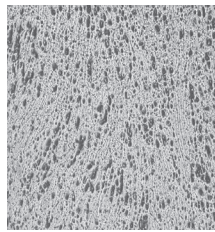
Figure 40. Optical micrograph for MEL alloy #129 (20X magnification).

Examination of Tables 6 and 7 shows many of the alloys have tensile stress and elongations comparable to those of AZ31. Not all of the alloys rolled successfully. While the aim was 10% cold work, it is apparent from the tensile stresses and elongations that substantial cold work was present in the hot-rolled alloys. This also needs to be quantified. These results do suggest that the alloying approach may work, and an alloy based on the compositions MEL suggested could be produced with low cost.

Annealing experiments were also performed on specimens of as-received commercial AZ31b-H24. The annealing was carried out in air, for the times and temperatures indicated by the graph in Figure 41. This alloy in the as-received condition cracked after 7% additional cold rolling, indicating that the cold work in the specimens was near a comfortable limit in order to simulate the required times and temperatures for intermediate anneals during multiple rolling operations. As evident from the graph, substantial recovery occurred in 15 min at 200oC or just 8 min at 250oC. Metallography for grain size and determination of when recrystallization occurred were not performed.
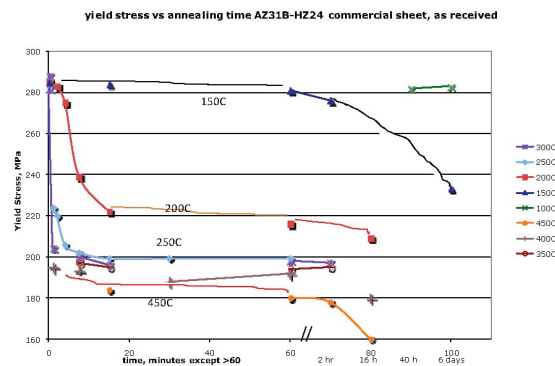
Figure 41. Recovery (tensile stress) of commercial AZ31b-H24 after the indicated times.

In summary, a series of new compositions that were cast in lab sized ingots by MEL Inc were successfully hot rolled and tested at ORNL. Some of the compositions showed comparable results to AZ31 suggesting that this alloying approach may achieve the goal of a less expensive alloy that is still comparable in properties. Recovery/ recrystallization studies showed that 15min at 200ºC or 8min at 250ºC was sufficient for recovery, suggesting that a continuous rolling process should be possible.

Table 6. Tensile properties of successfully rolled experimental wrought magnesium alloys

Tensile Stress and Ductility of Experimental Alloys, 10^{-3} strain rate, 25˚C, 25-mm gage length					
alloy #	**as hot rolled or with CW**	**Tensile Stress, MPa**	**Elongation, %**	**Rolled thickness, mils**	
100	HR	225	10	59	
	cw	265	6	52	**aim was 10%**
103	hr	253	9	60	
	cw	254	8	54	
104	hr	270	8	60	
	cw	287	4	58	
113	hr	213	6	54	
	cw	212	5	52	
115	hr	206	8	55	
	cw	222	1	50	
117	hr	293	10	58	
	cw	305	8	55	
123	hr	221	3	59	
	cw	223	4	52	
127	hr	254	3		**fr practice rolling batch**
128	cw	249	6		**fr practice rolling batch**
129	hr	224	11	60	
	cw	248	2	53	
159	hr	217	7		**fr practice rolling batch**
171	hr	269	15	60	
	cw	312	3	54	
191	hr	192	3	**did not roll**	
Comparisons					
az31	as received	270	24	arc lamp rolling paper[1]	**tested at ORNL, same geometry as above**
az31	as infrared rolled	312	5	infrared rolling paper[2]	**tested at ORNL, same geometry as above**
az31	as extruded	270	20	extrusion paper[3]	
az31	as received	294	12	roll bonding paper[4]	**tested at ORNL, same geometry as above**
az31	half hard	270	5	**MEL web site**	

[1]Horton JA, Blue CA, Agnew SR. Plasma arc lamp processing of magnesium alloy sheet. In: Kaplan HI, editor. Magnesium technology 2003. TMS; 2003. p. 243-6.

[2]Horton JA, Blue CA, Muth T, Bowles AL, and Agnew SR. Infrared processing of magnesium wrought alloys. In: Neelameggham NR, Kaplan HI, Powell BR, editors. Magnesium technology 2005. TMS; 2005. p. 155-8.

[3]Agnew SR, Horton JA, Lillo TM and Brown DW. Enhanced ductility in strongly textured magnesium produced by equal channel angular (ECA) processing. Scripta Mater 2004;50(3):377-81.

[4]Bowles A, Horton JA. Accumulative roll bonding of magnesium alloy AZ31. In: Pekguleryuz MO, Mackenzie LWF, editors. Magnesium technology in the global age. The Canadian Institute of Mining, Metallurgy and Petroleum; 2006. p. 183-92.

Table 7. Tensile properties of successfully rolled experimental wrought magnesium alloys

Alloy #	Processing	Yield (MPa)	Tensile (MPa)	Elong (%)
az31*	hr	145	263	14
	hr+10%cr	145	145	0
mel 102	hr	128	230	25
	hr+10%cr	246	257	5.2
	hr+20%cr	283	283	0.3
mel 105	hr	95	220	23
	hr+10%cr	242	254	2.8
	hr+20%cr	263	269	4.2
mel 108	hr	187	203	2.6
	hr+10%cr	23	238	0
mel 118	hr	8 142	236	21
	hr+10%cr	230	251	10
	hr+20%cr	274	281	2.3
mel 119	hr	165	239	14
	hr+10%cr	256	269	4
mel 120	hr	127	212	5.4
	hr+10%cr	220	237	0.6
mel 138	hr	111	238	24
	hr+10%cr	244	266	6
	hr+20%cr	287	294	3
mel 139	hr	114	225	13
	hr+10%cr	226	253	4.5
mel 140	hr	84	207	6.6
	hr+10%cr	216	216	0
mel 185	hr	123	179	19
	hr+10%cr	159	234	9
	hr+20%cr	211	231	9

*az31 cast into 1/2 slab at mel, hot rolled at ornl

A Meso-Scale Modeling Framework for Polycrystalline FCC Metals.

Recrystallization and Grain Growth Studies Using a Meso-Scale Approach

The objective of these studies is to develop and validate meso-scale simulations of microstructure and texture evolution during thermo-mechanical processing of Al- and Mg-alloy sheets and provide a microstructure module that can be integrated with the modeling efforts at MSST for capturing the main features of microstructure evolution and corresponding history effects occurring during cold/hot working and heat treatment of Al and Mg alloys.

This work involves large-scale, crystal-plasticity modeling of microstructural deformation, extracting the deformation substructure, and evolving the substructure during annealing using a meso-scale technique that includes a nucleation model for recrystallization based on orientation- dependent recovery of subgrains. A new nucleation model based on the concept of "excess" hardening dislocation is also presented. The input for meso-scale models was obtained by a realistic mapping of the initial experimental microstructure to the simulation domain.

Coupled Deformation-Recrystallization Simulations

Thermo-mechanical processing to produce optimum grain structure and texture is essential for the successful utilization of commercial Al and Mg alloys as sheet products. Several modeling techniques have been developed in the past with a reasonably good predictive capability for bulk deformation textures [Kocks 1998]. Significant progress has also been made in the last decade in the development of advanced measurement techniques for characterizing micro textures with high spatial resolution both in two- and three-dimensions. However, prediction of micro-texture evolution during deformation and its subsequent development during recrystallization remains very challenging because of uncertainties involved in predicting the mechanisms that

lead to the formation of recrystallization nuclei with specific crystallographic orientations and the uncertainties involved in predicting the grain/sub-grain boundary properties that determine the growth kinetics of the nuclei. With the availability of large computers and advances in software, it is now possible to perform simulations of polycrystalline deformation with a high enough resolution to capture the formation of in-grain misorientations [Sarma 1998]. Meso-scale simulations of annealing have been combined with the output of deformation simulations to predict the evolution of recrystallization textures [Radhakrishnan 1998, 2000, 2004A, 2004B]. In these simulations, nucleation is modeled by heterogeneous sub-grain growth incorporating misorientation and structure-dependent boundary properties. A recent development in the modeling of nucleation is based on an assumption of orientation-dependent recovery of sub-grains [Crumbach 2004; Radhakrishnan 2008].

Such an orientation-dependent recovery has been demonstrated in Al [Theyssier 1999], copper [Ridha 1982] and steels [Humphreys 1995; Barnett 1999; Yoshinaga 1998]. It has also been shown that the cell morphology in the deformed structure is a function of the grain orientation. In the case of polycrystalline Al, it was shown that orientations in the vicinity of the Cube had equated cell structure while the other deformation orientations had a cell structure that had a linear morphology [Liu, 1998]. The orientation-dependent cell morphology was explained on the basis of the number of different non-coplanar active slip systems [Liu, 1998]. For example, a high number of non-coplanar active slip systems was correlated with a more equiaxed cell morphology than when only a few co-planar slip systems are active during deformation. It has also been experimentally observed in Al polycrystals that orientations such as the Cube that have equiaxed cell structures also recover extremely fast compared to other deformation components.

Computational Approach

Generation of Input Microstructures: In order to obtain realistic comparisons between model and experiment, the input microstructures used for modeling should accurately capture the microstructural features present in the experimental system. The important microstructural features include the grain structure, the bulk texture, and the micro-texture that includes the grain misorientation distribution. The experimental data were in the form of EBSD scans performed on specific two-dimensional sections. A computational approach was developed for mapping the texture information obtained in the two-dimensional sections to a three-dimensional grain structure. The approach is based on reducing the large number of experimental texture points to a finite number of orientations and assigning the orientations to the grains in the three-dimensional structure. The assignments were done on the basis of a weighting function that describes the probability of existence of a given orientation. Because a three-dimensional grain structure has a range in the grain size, the texture obtained after the initial assignment does not usually have a good match with the experimental texture. Also, there is usually a poor match between the model and experimental grain-misorientation distribution functions. A computational approach that minimizes the error both in the texture and the misorientation distribution was developed.

The application of the grain-mapping code using the EBSD data generated for an Al 6022 hot band by MSST is shown in Figure 42. The agreement in texture between the mapped grain structure and the experimental texture is excellent.
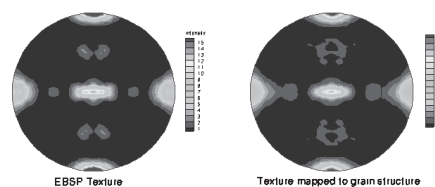
Figure 42. <100> pole figures showing textures from EBSD and the grain structure obtained by mapping.

The three-dimensional grain structure to which the texture was mapped is shown in Figure 43. The grain structure was generated by a MC grain-growth code with isotropic grain-boundary energy and mobility. The assumption is that the grain structure in the hot band is equiaxed. Further refinement of the mapping with simulated non-equiaxed grain structures is an extension of the current capability that will be pursued in the future.

Texture mapped grain structure
(colored using one of the Euler angles)

Figure 43. Three-dimensional grain structure to which the EBSD texture is mapped.

Microstructural Deformation: Meso-scale deformation simulations were performed using a polycrystal plasticity model incorporating neighboring grain interactions in which grain deformation is distributed in a non-uniform fashion among the polycrystals [Sarma 1996]. Interactions with surrounding crystals are incorporated in the calculation of the deformation rate of each crystal through an appropriately-defined local neighborhood. A compliance tensor is computed for each crystal based on a viscoplastic constitutive relation for deformation by crystallographic slip. The compliance of the crystal relative to that of its neighborhood provides a means for partitioning the macroscopic deformation rate among the crystals. Deformation modeling was also carried out using a finite-element implementation of the crystal plasticity model with grain-level discretization. The details of finite-element implementation are described elsewhere [Sarma 1998].The deformation of fcc polycrystals was simulated using 12 slip systems consisting of the 12 {111}<110> octahedral slip systems.

The grain structure shown in Figure 43 was deformed in plane-strain compression to a total cold deformation of 75% reduction in height using the neighborhood compliance model described previously. The final texture that results from the deformation simulation was compared with experimental EBSD texture data for the 1/32" sheet obtained by cold rolling the 1/8" hot band. Figure 44 shows <111> pole figures for the initial texture and the computed texture after cold deformation. The Cube component is generally unstable during cold deformation, and other deformation components form at the expense of the Cube component. However, there is still some residual Cube orientation present after cold deformation

(a)   (b)

Figure 44. <111> pole figures showing the texture in (a) 1/8" hot band and (b) computed texture in 1/32" sheet after plane-strain compression.

The experimental texture obtained by EBSD scan is shown in Figure 45 in the form of a <111> pole figure. The agreement with the simulated texture shown in Figure 44(b) is quite reasonable. The agreement can be improved using the more rigorous finite-element technique with a high degree of mesh refinement.
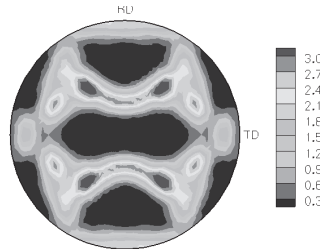
Figure 45. EBSD texture after cold rolling to 1/32".

Recrystallization and Nucleation Model: Recrystallization simulations were performed using a three-dimensional MC approach in a cubic grid. For local-energy calculations, the energy of the site and a neighborhood consisting of the first, second, and third nearest neighbors was used. The input microstructure for the MC simulations was obtained from the output of the crystal-plasticity simulations. The details of the MC procedure are described elsewhere [Radhakrishnan 1998].

The nucleation step during recrystallization was modeled as follows. For each site in the simulation domain, the total shear rate on each {111}<110> slip system was calculated for the entire deformation. For each site, the total shear rate on the non-coplanar systems was calculated by adding the shear rates belonging to a given (111) plane. The shear rates were then normalized by the maximum shear rate for each site and added. The resulting quantity was further normalized by the maximum value in the system to give nucleation probability for each site as a fraction with an upper bound of 1.0. The above definition is different from the definition of the active number of slip systems proposed by Crumbach et al. [Crumbach 2004]. While Crumbach et al. defined the orientation-dependent recovery based on the total number of active slip systems, we specifically identify the non-coplanar slip systems (slip systems with different slip plane) and base our nucleation probability on the relative shear rates in the non-coplanar slip systems.

Figure 46 shows the recrystallization texture obtained using the meso-scale recrystallization model that used the simulated deformation texture in Figure 44(b) as the input. The recrystallization texture shows a strong Cube component, although orientations rotated from Cube are also present. This is in general agreement with the results seen in the literature, although a direct comparison of the model with experiments will await measurements on the 1/32" sheet. The recrystallization simulations used the nucleation model based on orientation-dependent recovery described previously.
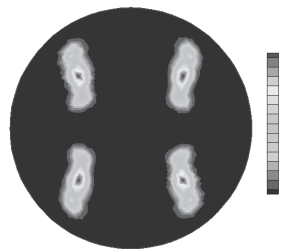
Figure 46. Simulated recrystallization texture in the annealed 1/32" sheet.

The nucleation probability as a function of the site number in the microstructure is shown in Figure 47. The orientations that recovered quickly to form the recrystallization nuclei correspond to those sites that had a high value for the nucleation probability.
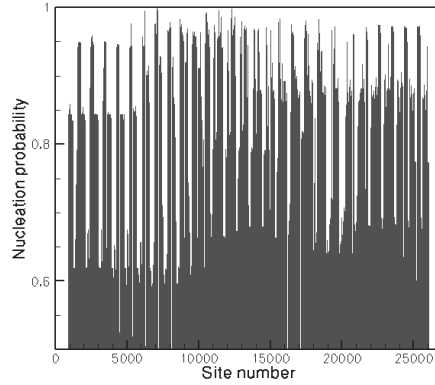
Figure 47. Nucleation probability as a function of site number.

The meso-scale model, in addition to capturing the texture, also captures the recrystallization kinetics, as shown in Figure 48. The simulations currently do not have the capability to model the recrystallization as a function of real time and temperature. However, it is possible to convert the Monte Carlo time step (MCS) shown as the time axis in Figure 48 to real time using a technique that was developed for modeling grain growth in a temperature gradient.
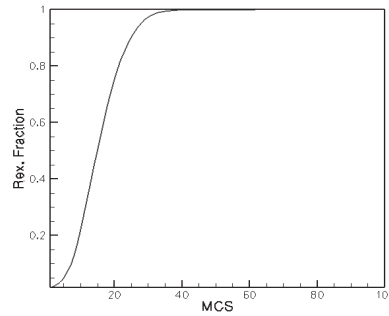
Figure 48. Recrystallization kinetics obtained using the meso-scale annealing simulations. MCS represents the Monte Carlo time step.

New Nucleation Model: A new model for the nucleation of recrystallized grains in FCC polycrystals was developed, based on the concept of "excess" hardening dislocations. The basic premise behind this approach is the existence of dislocations with mutually perpendicular Burgers vectors in FCC polycrystals. Interaction of these mutually perpendicular dislocations does not lead to hardening, since these dislocations remain mobile and do not form locks. The high mobility of the resulting special boundaries promotes rapid recovery of the dislocation substructure. Crystal orientations that have equal amounts of mutually perpendicular dislocations will recover very quickly to form recrystallized nuclei, while orientations with "excess" dislocations will form complex dislocation substructures that are slow to recover.

The nucleation step during recrystallization was modeled as follows. For each site in the simulation domain, the slip system deformation rate in the crystal coordinate system is calculated as

$$D_{ij}^\alpha = \dot{\gamma}_\alpha P_{ij}^\alpha$$

where P^α_{ij} is the symmetric part of the Schmid tensor and $\dot{\gamma}_\alpha$ is the shear rate on slip system α. Among the octahedral slip systems, those containing mutually perpendicular Burgers vectors are identified, and "excess" dislocations are calculated by taking the absolute difference in slip system deformation rates on all such systems. A recovery factor is computed based on the sum of the "excess" dislocations over the entire deformation history, and a probability for nucleation is computed based on the recovery factor.

An illustration of the distribution of slip system deformation rates in some of the commonly found orientations in rolled Al sheet is shown in Figures 49-51 for the D_{12}, D_{13}, and D_{23} components, respectively. For Cube orientation, the slip system deformation rates are completely balanced and can form high mobility, low energy boundaries that contribute to quick recovery. On the other hand, for Copper and S oriented grains, the slip system deformation rates are not balanced, leading to "excess" dislocations that interact to form complex dislocation substructures and lead to slow recovery.
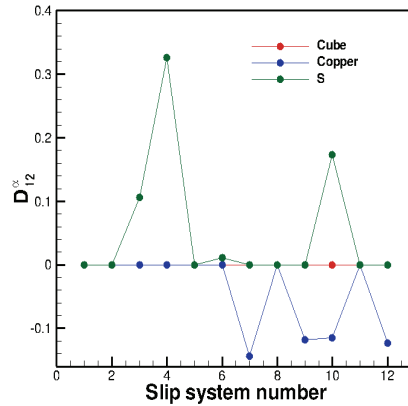
Figure 49. Distribution of deformation rate component D12 among various slip systems.
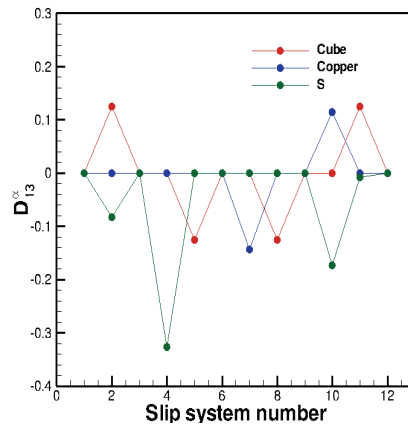
Figure 50. Distribution of deformation rate component D13 among various slip systems.
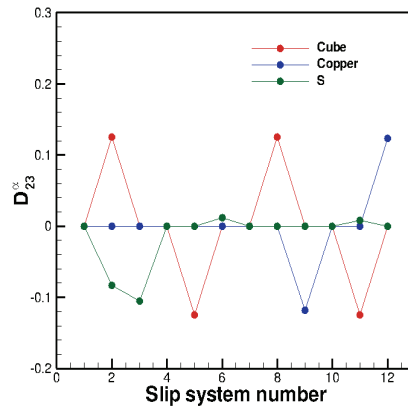
Figure 51. Distribution of deformation rate component D23 among various slip systems.

The combined deformation and recrystallization model was used to simulate the deformation of an FCC polycrystal using a domain size of 180x180x180 sites. This problem was simulated on 216 processors. The input microstructure for the deformation model was obtained through grain growth, starting with a different orientation from a random distribution at each site. The grain growth simulation was performed until the average grain size was about 8, which resulted in a microstructure with about 11,000 grains.   The initial texture for this microstructure is shown in Figure 52 as a <111> pole figure.
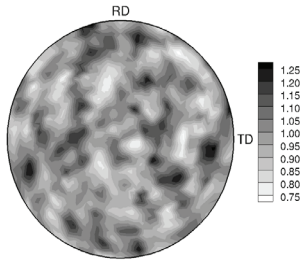
Figure 52. <111> pole figure showing the initial texture for the microstructure with about 11,000 grains.

The microstructure was deformed in plane strain compression using the neighborhood compliance model described above under hot rolling conditions to a compressive strain of -2.0 (about 86% reduction). The resulting deformation texture is shown as a <111> pole figure in Figure 53. The microstructure was then recrystallized, making use of the nucleation model discussed above. The result is a strong Cube texture, as shown in Figure 54, even though Cube is not a major component in the deformed texture.
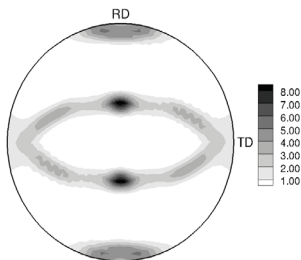
Figure 53: <111> pole figure showing the texture after deformation in plane strain compression to 86% reduction.
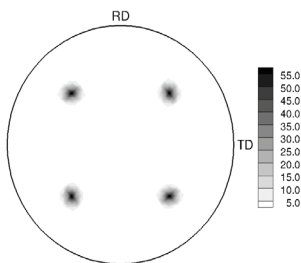
Figure 54: <111> pole figure showing the texture after recrystallization, indicating a strong Cube component.

Benchmark Deformation Simulations for FCC and HCP Polycrystals

Simulations using the crystal-plasticity finite-element model were carried out using a single finite element containing an aggregate of 256 orientations within the element for computing the material response. These simulations were compared with the results from a material point simulation (MPS) program, where the mechanical response and texture evolution of an aggregate of grain orientations is computed for a given velocity gradient, and the velocity gradient for each orientation is assumed to be the same as the applied velocity gradient (under the Taylor hypothesis). These simulations were intended to serve as a verification of the implicit integration scheme used to evolve the material state.

The response of both FCC and HCP crystals under plane-strain compression was simulated. The FCC crystals were assumed to deform on the twelve {111}<110> slip systems, while the HCP crystals were assumed to deform on the three (0001)<2 -1 -1 0> basal, the three {1 0 -1 0}<1 -2 1 0> prismatic and the twelve {1 0 -1 1}<1 1 -2 3> pyramidal slip systems. The material parameters for the FCC and HCP crystals were taken from [Marin 2006]. The slip system strength for the FCC crystals was assumed to be the same for all the slip systems, and the evolution in strength was assumed to be isotropic. For the HCP crystals, the pyramidal slip systems typically have higher strength and, in these simulations, the strength of these systems was initially assumed to be five times the strength of the basal and prismatic systems, and this initial strength difference was maintained through the deformation. A value of 1.633 was assumed for the axial (c/a) ratio for the hcp crystals.

The results from these simulations are shown in Figure 55 in the form of the stress-strain response, and in Figures 56 and 57 in the form of pole figures to show the texture evolution for the FCC and HCP crystals. The stress values have been normalized by the initial slip-system strength. These results show that the response of the aggregate with initially random orientation distribution is very similar from both the MPS program and the finite-element model (FEM). There are small deviations in the stress-strain response with increasing strain, and this is thought to be a consequence of the velocity gradient in the finite element model deviating slightly from the exact plane-strain compression that can be enforced in the MPS program. These results serve to verify the implementation of the integration scheme for the elasto-viscoplastic crystal plasticity model in the finite-element model.
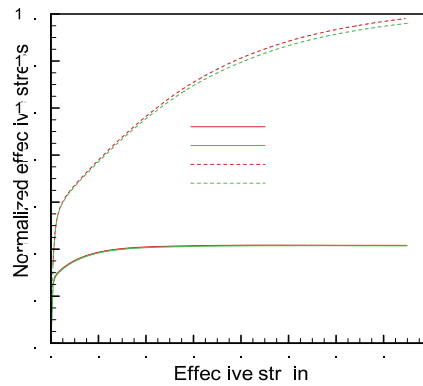
Figure 55. Stress-strain response for an aggregate of 256 FCC and HCP crystals deformed in plane-strain compression computed using material point simulation and one-element finite-element model.
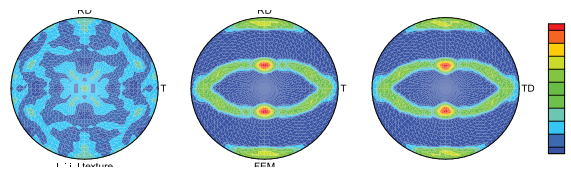
Figure 56. <111> pole figures showing texture evolution for plane-strain compression of an aggregate of 256 fcc crystals computed using MPS and one-element finite-element model.
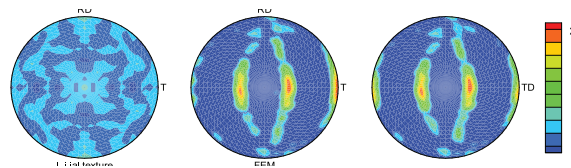
Figure 57. <0001> pole figures showing texture evolution for plane-strain compression of an aggregate of 256 hcp crystals computed using MPS and one-element finite-element model.

The finite-element model was used to simulate FCC and HCP polycrystals with each element representing a single crystal of a different orientation. A unit cube was discretized using a 7×7×7 element mesh, and each element was initially assigned an orientation from a random distribution. The polycrystals were subjected to three different deformation modes: plane-strain compression, uniaxial compression, and simple shear. The material parameters for all simulations and the slip systems for both FCC and HCP polycrystals are the same as described above for the one element simulations.

The deformed mesh for the FCC polycrystal subjected to plane strain compression is shown in Figure 58. The differences in orientations between the elements lead to the highly heterogeneous deformation that is evident from the distorted mesh. The textures after deformation are shown in Figure 59 in the form of <111> pole figures and are consistent with the textures expected for the different modes of deformation for FCC polycrystals.
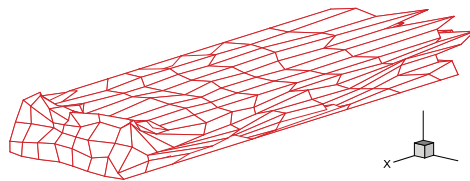
Figure 58. Deformed mesh for 7×7×7 element mesh FCC polycrystal deformed under plane-strain compression (ε = 1.3).
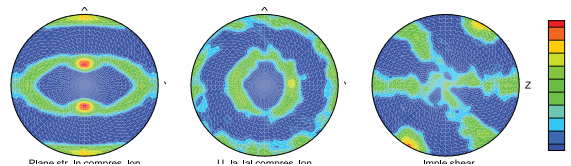
Figure 59. <111> pole figures showing texture evolution for 7×7×7 element FCC polycrystals subjected to various modes of deformation.

Similar results for textures after deformation of the HCP polycrystal are shown in Figure 60 in the form of <0001> pole figures. As in the case of the FCC polycrystals, the textures for the different modes of deformation are consistent with those typically observed for HCP materials. The results from these simulations also compare well with similar results presented in [Marin 2006] and have been used to verify the performance of the finite-element implementation for materials with HCP crystal structure.
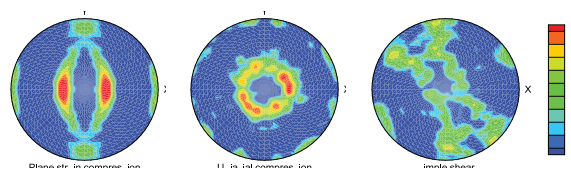
Figure 60. <0001> pole figures showing texture evolution for 7×7×7 element HCP polycrystals subjected to various modes of deformation.

As a summary, the coupled deformation-recrystallization simulations are able to capture the texture evolution in Al 6022 during deformation and static recrystallization reasonably well. However, further improvement can be obtained by more rigorous deformation models using grain-level discretization and more efficient incorporation of the nucleation model to evolve the deformation substructure. Finally, extension of the current capability for modeling the deformation using the crystal-plasticity-based finite element method to HCP polycrystals has been verified using benchmark problems.

Material Database for Aluminum and Magnesium Alloys: Sheet Metal Experiments

Experimental and Numerical Investigation of Kinematic Hardening Behavior in Sheet Metals

Northwestern University has been continuously working on the experimental apparatus for testing material's kinematic hardening behavior of thin sheets. In this work, a novel in-plane tension-compression device was introduced for sheet materials (see Figure 61). This double-wedge device is easy to be fabricated and able to cover the specimen surface completely. Therefore, potential buckling of sheet specimen can be prevented. Using the developed device, the frictional force between the plate and specimen can be neglected for both tension and compression tests. The through-the-thickness biaxial stress and plane strain condition were also investigated by using the FEM simulation for the compression test. Once the Teflon film was attached on the plate, the material status was not under the plane strain condition, which is desired for the uniaxial tension/compression test. Also, the stress ratio between the equivalent stress and the compressive axial loading stress was less than 1.6%, so that the biaxial effect of the through-thickness stress can be ignored in the tension-compression test using the double-wedge device.

Figure 61. Front view of the test apparatus.

In order to measure the strain correctly, the transmission type laser extensometer was utilized and the double-side fins were considered in the specimen, as depicted in Figure 62. Through FEM simulations, it was found that the specimen with double-side fins resulted in a more uniform strain distribution than that from the specimen with single-side fins. Test results showed that the double-wedge device can perform stable tension-compression (15% pre-strain) and compression-tension (9% pre-strain) tests for a sheet thickness of 0.8mm and a good repeatability for a couple of cyclic tests (see Figure 63)
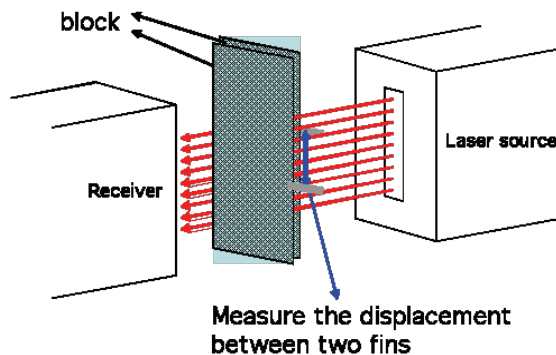
Figure 62. Strain measurement system used.

(a)   (b)
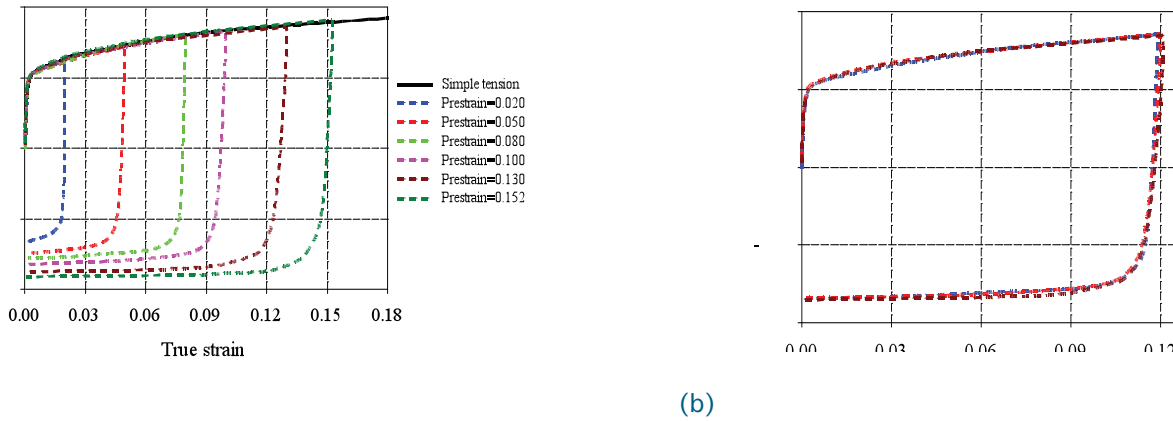
Figure 63. Test results of the 0.8mm BH180 steel sheet: (a) tension-compression test; (b) repeatability (at 0.12 pre-strain level)

The Characterization of Forming Limits for Process Design

Sheet-metal forming processes have been widely used to fabricate a desired sheet-metal product in many industries such as automotive, appliance, aerospace, and others. Productivity and high strength but lightweight products are among the key attributes that sheet-metal forming processes could offer. However, uncertainties due to uncontrollable conditions (e.g., metal suppliers, forming conditions, and numerical errors) play an important role and need to be taken into account in the design process.

The process characteristics considered for design optimization are related to the margin of safety/failure of the sheet metals. Failures in sheet-metal fabrications generally come from three main phenomena: springback, tearing, and wrinkling. In this stamping study, our focus is on tearing and wrinkling. Tearing is a failure due to an excessive localized load leading to a local instability causing the sheet metal to split [Swift 1952; Keeler 1964; Marciniak 1967; Cao 2002]. Wrinkling is an unstable phenomenon mainly due to excessive in-plane compressive loads [Wang 2000].

The first step in characterizing uncertainties in sheet metals is to examine the forming limits of metal sheets. Forming-limit diagram has been a popular tool in industry to characterize the material resistance to thinning since Keeler and Backofen [Keeler 1964] introduced the concept in 1964. In this project, the forming limit curves of two particular lightweight materials are determined: magnesium sheet AZ31 and aluminum sheet AA6022.

Forming Limits of Lightweight Magnesium Alloy AZ31

The focus of this work is to experimentally characterize the forming limits of Magnesium Alloy Sheet, AZ31, at elevated temperatures, 200°C and 170°C. Magnesium sheet has poor formability at room temperature. However, its formability can be dramatically improved at elevated temperature.

Experimental Setup

Figure 64 shows the limit dome test apparatus for testing sheets at elevated temperature at Northwestern University. The setup inside the oven, i.e., punch and die, is shown in Figure 65.
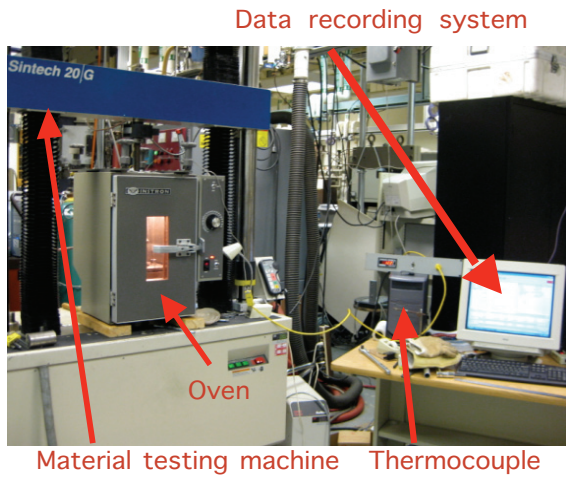
Figure 64. Limit Dome Test Apparatus at NU.
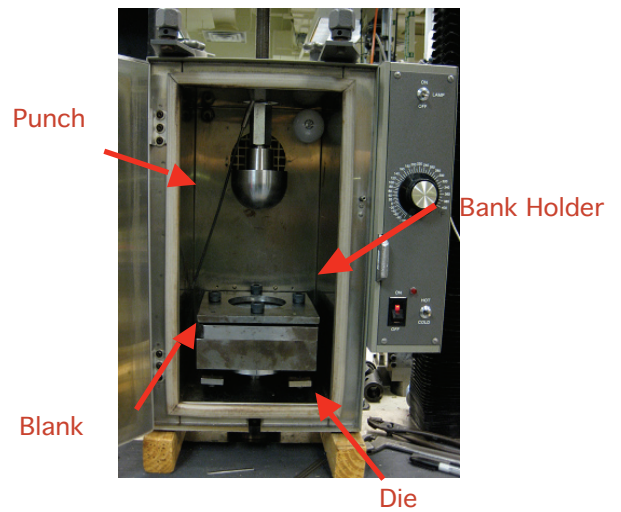
Figure 65. Tooling setup in the oven.

The experiments were conducted using a universal material test system, Sintech 20G, shown in Figure 64. The capacity of the machine is 100 kN while the operation temperature is between -90°C and 1600°C. The oven used in this particular test has the highest temperature around 204°C. The thermocouple, having the operation range between -180°C to 1300°C, was inserted into the oven during the experiment to measure the actual temperature during the operation.

The Magnesium sheets (AZ31BH24) tested at NU were supplied by General Motors. There are two different thicknesses, 2 mm and 4 mm. Our tooling can only handle a maximum thickness of 2 mm in order to provide the sufficient clamping force during the test.

Five sample dimensions have been designed in order to obtain various strain states needed for the forming limit diagram (FLD). A square size with 160mm*160mm has been chosen to capture the failure in the equal bi-axial state. A rectangular size of 160mm*100mm has been introduced to capture the limit at the plane strain condition. Two more rectangular sizes, 160mm*135mm and 160mm*110mm, have been used to capture the strain states in between the above two. The sample size to capture the failure at the uni-axial condition has been specially designed as shown in Figure 66.
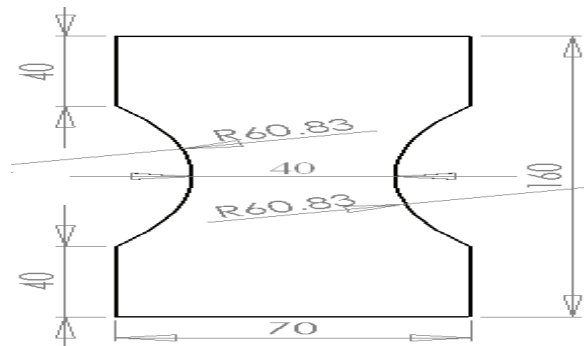
Figure 66. Dimension of the sample to capture failure in uni-axial condition.

An electrolyte, with a capacity of 250A and manufactured by LECTROETCH, is used to etch circle grids onto the Mg sheets. The circle size of the stensile is 2.5mm. The etching equipment is shown in the Figure 67.
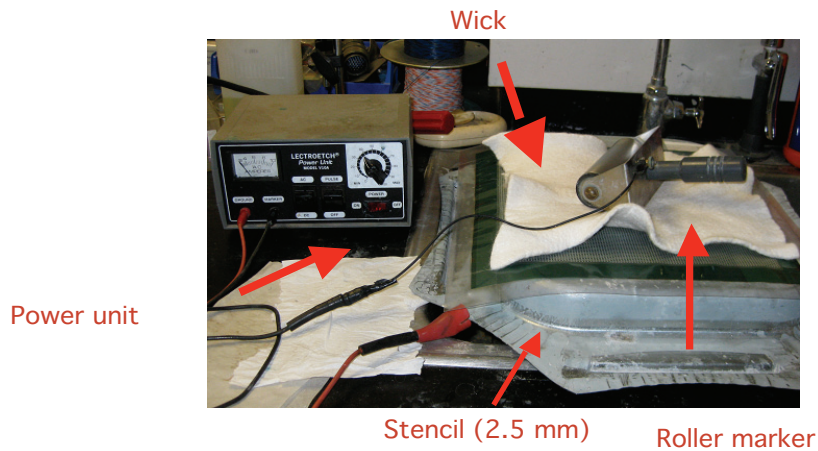
Figure 67. Etching equipment.

The etching effect is presented in Figure 68. The grey mark can be observed by eyes and also can be clearly measured with a microscope (as shown in Figure 69). The average diameter of the inner edge is around 2.2mm.

Figure 68. Etching effect (with 250A).
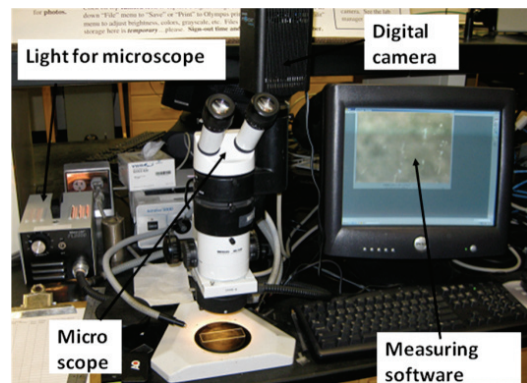
Figure 69. Microscope measuring system.

Experimental Procedure

The test procedure used in the experiments has the following steps:

1. Align the punch and die at room temperature. As the punch was attached onto the top beam of Sintech 20G with threads, its center may be a little offset from the center of the hole. Hence, the punch should be attached onto the upper beam first, followed by the position adjustment of die location. The die will then be fastened onto the bottom supporting disk of the test machine.

2. Clamp the blank: insert the blank onto die surface and then put the blank holder on. Four bolts are screwed into the die to clamp the blank between the die and the blank holder. Care must be taken in this step to avoid fracturing the sheet.

3. Heat the oven. It will take around 3 hours for the oven to heat the die blocks from room temperature to 200°C.

4. Align the punch and die at elevated temperature. The alignment obtained at room temperature needs to be checked or adjusted to make sure that there still exists a good alignment at elevated temperature.

5. Fasten the bolts. Fasten the bolts after the alignment of tooling at elevated temperature with a torque wrench using a suggested maximum torque of 70 ft.lbf.

6. Heat the oven. The temperature in the oven will drop to 140°C after checking or adjusting the tool alignment at elevated temperature. It will need another 1 hour to heat the temperature from 140° C to 200°C.

7. Fasten the bolts again. When the temperature of oven comes back to 200°C, it is time to fasten those four bolts again. The bolts are fastened with a torque wrench to a maximum torque of 90 ft-Lb$_f$.

8. Put the Teflon sheet onto the blank (as shown in Figure 70): Teflon sheet with 0.4mm is used as lubrication in the experiment. The Teflon sheet is trimmed to circle shape with a diameter of 110mm. One layer of Teflon sheet was found to be easily torn during the experiment. Hence, two layers of Teflon were used in the experiment as lubrication.

9. Heat the oven. The oven temperature may drop to around 170°C after steps 7 and 8. Another 0.8 hour will be needed to heat the temperature back to 200°C.

10. Conduct the forming experiment. When the temperature comes back to 200°C, move the punch down with the speed of 5 mm/min. The punch will be automatically stopped when the current forming force drops under 70% of the peak force.
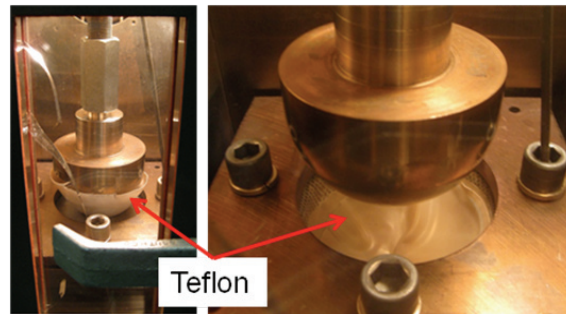
Figure 70. Limit Dome Height (LDH) test with Teflon sheet.

After the experiment, the formed part will be taken out of the tooling and marked with for the next strain measurement.

Experimental Results

The forming limit of magnesium sheet (AZ31BH24) has been tested at two temperatures: 200°C and 170°C. Figure 71 showed typical samples obtained from the forming limit tests. The fractured samples were used to setup the maximum punch height used in the experiments while the non-fractured samples were used to obtain the strain states in the safe zone.

Forming limit curves (FLC) are presented in the following two figures. It can be seen that magnesium (AZ31BH24) has a very good formability at 170°C and also at 200°C. The formability at those two temperatures is similar, which means that a lower forming temperature can be used to be more energy efficient.
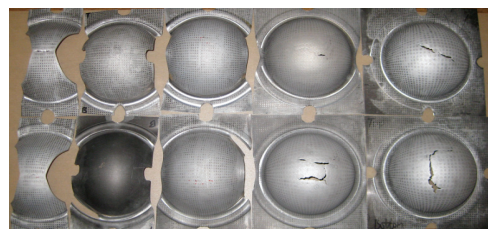
Figure 71. Samples: the first row - 170°C, bottom row - 200°C.
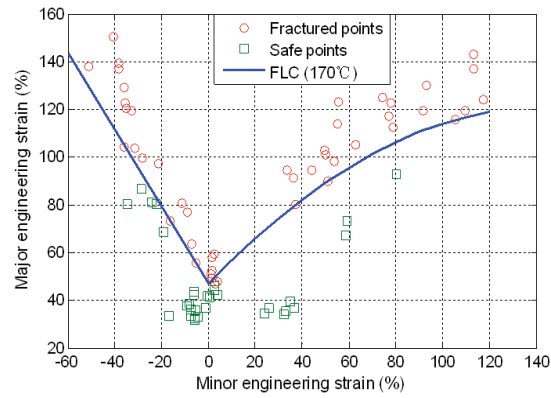
Figure 72. FLC at 170℃.
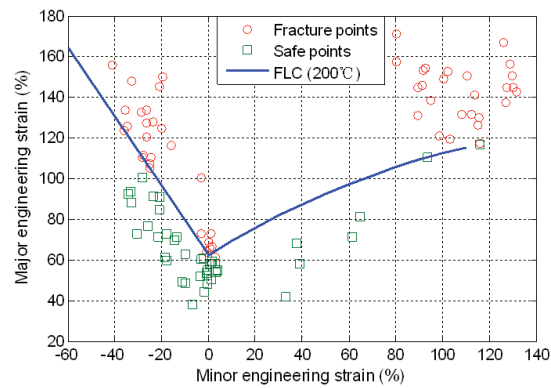
Figure 73. FLC at 200℃.
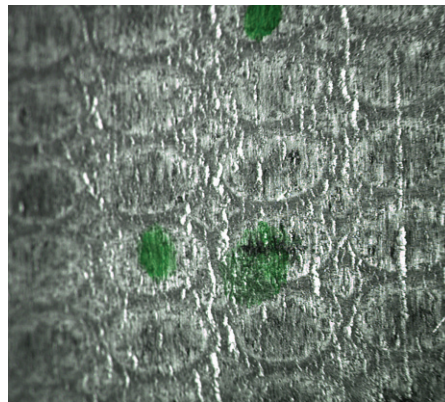
Figure 74. Diffuse necking of fractured sample at 170C.

The samples (160mm*110mm) fractured at the area which is very close to the corner of the die at both 170C and 200C (see Figure 71). This failure was cause by the shearing instead of stretching. Figure 74 shows the diffuse necking part of the central part of the plane strain sample (160mm*100mm) at 170C after the LDH test. There exists a distinct necking strip (not localized fracture). The forming limit at the plane strain state - FLC_0 is about 0.46 at 170C and 0.62 at 200C.

From results of warm LDH tests (Figures 72 and 73), it can be seen that there exists a distinct boundary between necking points and safe points for samples at both temperatures especially on the left side of FLCs. On the right side of FLC at 200C (Figure 73), diffuse necking was

found close to the equal bi-axial state because of the severe necking of the sample which can be found on the two samples shown in the bottom row of Figure 71. One of the punch load-displacement curves recorded in LDH tests is shown in Figure 75. One can use the shape of punch load-displacement curves to empirically determine and then stop the punch at the very beginning of a fracture.
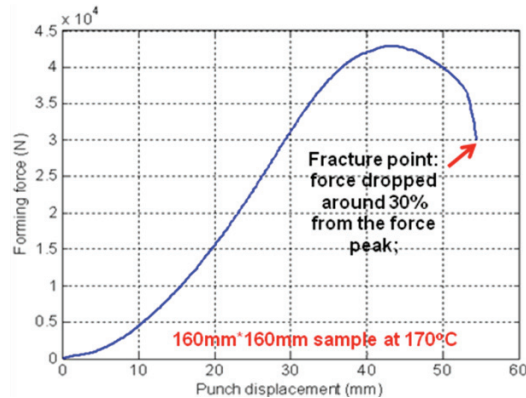
Figure 75. Punch force and displacement recorded in LDH test.

Although the magnesium sheet (AZ31B-H24) shows a better formability at higher temperature, it requires more energy consumption. The variation of the thickness in the formed part is also larger than that at lower temperature. As observed from the dome test, the necking deformation contributes a great part of limit strains, especially in the equal bi-axial state. An optimum forming temperature is needed to keep a balance between the forming costs, formability, and the mechanical ability of the formed part for the magnesium sheet.

Forming Limits of Lightweight Aluminum Alloy AA6602

The forming limit tests for 6022 aluminum alloy were performed at room temperature. Figure 76 shows the set-up of the limit-dome test apparatus used in these experiments.
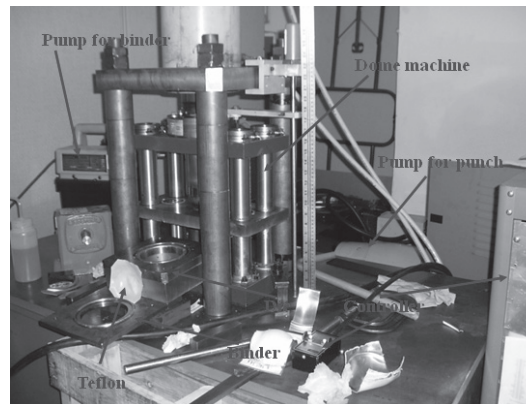
Figure 76. Limit dome test at NWU.

The aluminum sheets were provided by MSST. For the experiments, the sheets were first marked by grids and then clamped between binder rings and deformed by the punch. To reduce friction between the sheet metal and the punch, a Teflon sheet is used between the metal and the punch. Before and after the deformation, grid sizes were measured using microscopes as shown in Figure 77. Various widths of samples (Figure 78) were used to obtain various strain paths. Finally, the forming limit diagram can be obtained as shown in Figure 79. It can be seen that there exists a 0.025 strain variation in the forming limit curve.
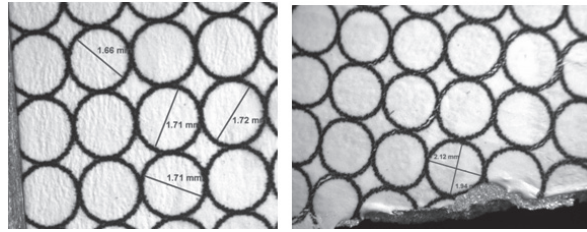
Figure 77. Grids on sheet metal: (a) before deformation; (b) after deformation (near a crack).
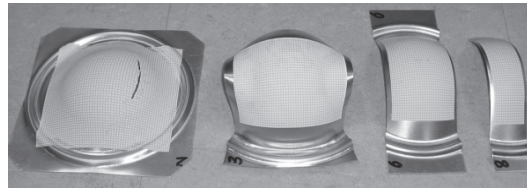
Figure 78. Samples used in the limit dome tests.
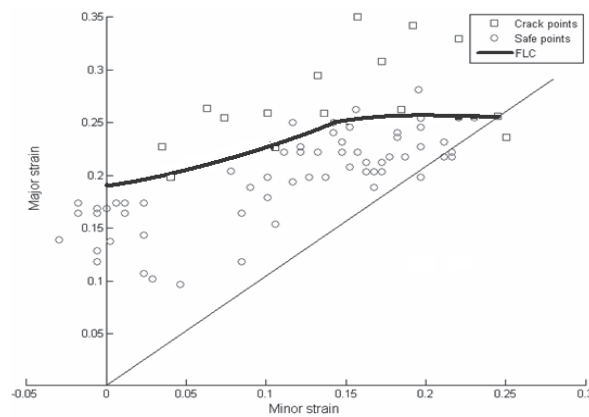
Figure 79. Forming limit diagram of AL6022.

Framework for Reliability-Based Design Optimization of Thermomechanical Processing

Flowchart of Probabilistic Design of Stamping Process

The design process for a stamping process is summarized in the flowchart shown in Figure 80. The main focus of this work is to create an integrated framework for robust and reliability design of a stamping process that achieves a design specification in terms of failure free and takes into account uncertainty.

The design process considering uncertainties for sheet metal forming processes requires integration of finite-element analysis (FEA), statistical analysis, and decision making. Design and optimization under uncertainty provides a means such that unacceptable failures are unlikely to occur with an acceptable confidence.

Study the physics of the stamping process → Process parameterization via DOE → FEA → Tearing analysis / Wrinkling analysis

Robust/reliability design model ← Performance/Margin quantification

Optimization search → Uncertainty assessment

Not Satisfied: Investigate what went wrong ← Verification → Satisfied
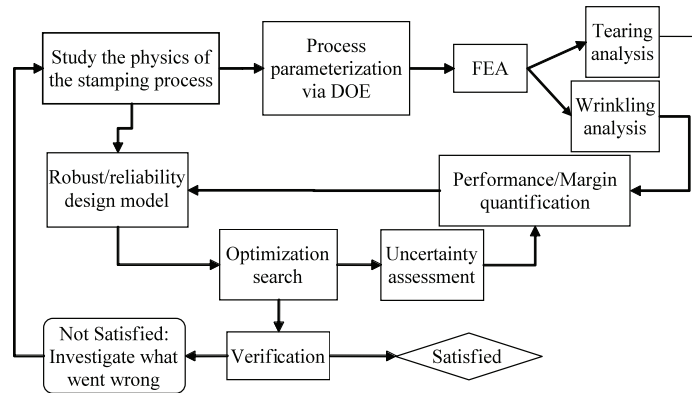
Figure 80. Design Process of Stamping.

In most engineering applications, mean and variance are the parameters of interest to define a probabilistic system. Uncertainty propagation techniques for statistical moments have evolved from analytical probabilistic models and a sampling-based approximation technique called Monte Carlo simulation. Analytical probabilistic models mostly are very difficult to develop. Monte Carlo, on the other hand, is a powerful approximation technique that relies on pseudo random numbers but it requires a large (and often impractical) computational effort. In this work we will employ the state-of-the-art uncertainty propagation techniques to improve the efficiency of this process.

A Probabilistic Design Model for Optimizing Stamping Process

A sheet-stamping process is subjected to tearing and to wrinkling failures due to process setups and material properties. In addition, variations associated with process setups and material properties play a role in the quality of the product. Here, we formulate a probabilistic design model by incorporating uncertainty and both tearing and wrinkling criteria. In sheet-metal forming design, we consider failure margins as design requirements that a forming process needs to satisfy. A design solution needs to also satisfy all reliability requirements in failure analysis (wrinkling and tearing), when uncertainties are taken into account. The constraint statements are defined as follows:

• Probability of tearing occurrence must be less than X (the probability of not having tearing must be larger than R). The statement is mathematically written as follows

$$\left| \quad \right| \left| \quad \right| \quad - \quad$$

where f is the margin, which is defined by a strain-based criterion. The simplest case is to monitor if strain $|\mathcal{E}_{appl}|$ at one point exceeds the limit value $|\mathcal{E}_{cr}|$. By using the stress-based forming limit diagram as the failure criterion, we have another equivalent statement as follows

$$> \quad = \quad - \sigma \quad \left\| \sigma \ \sigma \ \right| > \ \geq \ =$$

• Probability of wrinkling occurrence must be less than X (the probability of not having wrinkling must be larger than R). The statement is mathematically written as follows:

$$\left| \quad \right| \left| \quad \right| \quad - \quad$$

where f is the margin, which is defined by a stress criterion.

To simplify the probabilistic design model, we utilize the moment matching technique [Du 2000] to create an equivalent model in a format of robust/reliability design. While the objective is used to achieve the robust design goal, the constraints are used to ensure reliability. The moment

matching method is an approximation technique that does not need to estimate the entire probability density function (PDF) not by assuming the response follows normal distributions (only need the mean and variance of the system response). As a result, the need of the resources on the uncertainty propagation is reduced. The probabilistic design model is written as follows:

Minimize   ,

$$= \frac{-\sum \mu}{M} + \frac{}{\Sigma}$$

Subjected to ,

$$g_i = -(\mu_{f_i} - k_i \sigma_{f_i}) \le 0$$

$$x \in \Omega$$

where y is the objective function; g_i is the ith constraint function; W_1 and W_2 are weighting factors for normalized means and normalized variances, respectively; w_i is a weighting factor for the ith component; μ_{f_i} is the mean value of f_i; $\sigma_{f_i}^2$ is the variance value of f_i ; M_f^* and Σ_f^{2*} are used to normalize the two aspects of the robust design objective; κ_i is the ith moment factor (corresponding to a minimum reliability) to capture the feasibility of a robust design constraint under uncertainty. The uncertainty propagation techniques previously presented before are utilized for these statistical moment calculations. In particular, we will use the weighted three-point-based method for the mean and variance estimation.

The objective of the model is to minimize the negative value of the expected value of the total margin and its total variance while to maintain the minimum reliability requirements.

Robust Design with Arbitrary Distribution Using Gauss-Type Quadrature Formula

As a rigorous method of uncertainty propagation, the Gauss-type quadrature formula is investigated and applied to robust design formulated in terms of statistical moments of system performances. Due to the highest precision it provides, the Gauss-type quadrature formula is a well known method in the field of numerical integration. However, it has not been extensively used for uncertainty propagation involving various types of random variables. In this work, we developed a systematic procedure to find the nodes and weights of the Gauss-type quadrature formula for arbitrary input distributions and examined its mathematical meaning. It is shown that the nodes and weights of a m-node Gauss-type quadrature formula for a continuous random variable X are the samples and probability mass function of a discrete distribution, respectively, which is equivalent to X in terms of moments up to 2m-1 order. Thus, those nodes and weights can be found from the moments of input random variables with various numerical approaches. Multidimensional quadrature formula can be built from the one dimensional quadrature formula and the tensor product formula and univariate dimension reduction method are adopted in our work.

A procedure for robust design optimization using the Gauss-type quadrature formula is proposed with an emphasis on the efficient calculation of design sensitivity. Since one evaluation of statistical moments requires multiple function evaluations, the design sensitivity evaluation using approximate schemes such as finite difference method will increase the computational cost of optimization significantly. In our research, formulas for semi-analytic design sensitivity of statistical moments are derived for tensor product and univariate dimension reduction method,

which utilize the sample data obtained during the moments estimation. It is shown from our case studies that the proposed design sensitivity analysis reduces the computational cost of robust design up to 40% when compared to the finite difference method.

Level Set Based Robust Shape and Topology Optimization under Random Field Uncertainties

A level-set-based method for robust shape and topology optimization (RSTO) is proposed in this work with consideration of uncertainties that can be represented by random variables or random fields. Uncertainties, such as those associated with loading and material, are introduced into shape and topology optimization as a new dimension in addition to space and time, and the optimal geometry is sought in this extended space. The level-set-based RSTO problem is mathematically formulated by expressing the statistical moments of a response as functionals of geometric shapes and loading/material uncertainties. Spectral methods are employed for reducing the dimensionality in uncertainty representation and the Gauss-type quadrature formulae is used for uncertainty propagation. The latter strategy also helps transform the RSTO problem into a weighted summation of a series of deterministic topology optimization subproblems. The above-mentioned techniques are seamlessly integrated with level set methods for solving RSTO problems. (Figure 81) The method developed is generic, which is not limited to problems with random variable uncertainties as usually reported in other existing work, but is applicable to general RSTO problems considering uncertainties with field variabilities. This characteristic uniquely distinguishes the proposed method from other existing approaches. Preliminary 2D and 3D results show that RSTO can lead to designs with different shapes and topologies and superior robustness compared to their deterministic counterparts (see example in Figure 82).
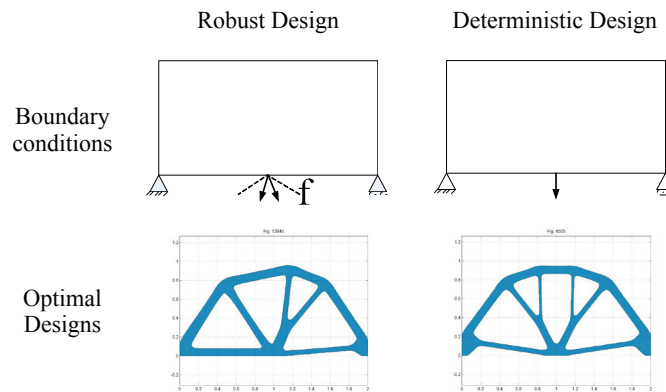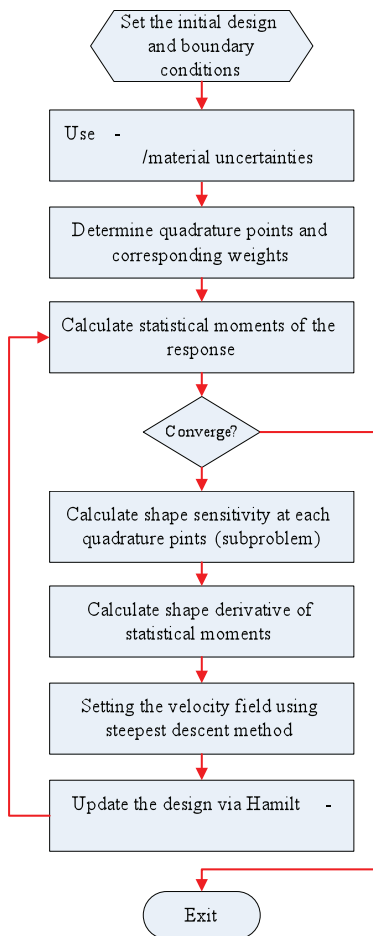
Figure 82. Robust versus Deterministic Topology Optimization.

Figure 81. Flow Chart of the Robust Shape Topology Optimization Algorithm.

UMAT Subroutine for Magnesium Metals and Alloys

Because of the light weight and ease of recycling, magnesium metals and alloys are of particular interest for automotive companies. However, due to the special material behaviors of these materials, few finite element analysis implementations customized for magnesium constitutive law are available. Based on the existing theoretical work of orthotropic yield stress function by [Cazacu 2005] and separate isotropic hardening law for tension and compression by [Kim 2008], a numerical implementation procedure is proposed in this work. Our goal is to develop realistic finite element simulations for modeling the behavior of magnesium alloys.

The proposed numerical implementation procedure consists of the following two phases: elastic and elasto-plastic. In the elastic phase, a trial stress for a given discrete strain increment is evaluated assuming that the increment is elastic, while the equivalent plastic strain is kept as previous. If the effective stress given by the yield criterion is less than the yield stress calculated from the hardening law, the process is considered as elastic. Otherwise, the second phase is carried out. In the elasto-plastic phase, a Newton-Raphson iteration method is used to solve the equivalent plastic strain increment which allows effective stresses calculated separately from yield criterion and hardening law to be equal.

For verifying the numerical implementation procedure proposed above, a single shell element is created in the commercial FEM package ABAQUS and tested under uni-axial tension and compression in rolling and transverse directions using the developed user defined material UMAT subroutine. As shown in Figure 83, the transverse direction exhibits higher yield strength than that in the rolling direction which is consistent with the experiment data presented in [Kim 2008]. Similar results are shown in Figure 84. If tension and compression results are compared, it can also be observed that the compression yield stress is less than the tension yield stress, a phenomenon observed from Mg alloys.
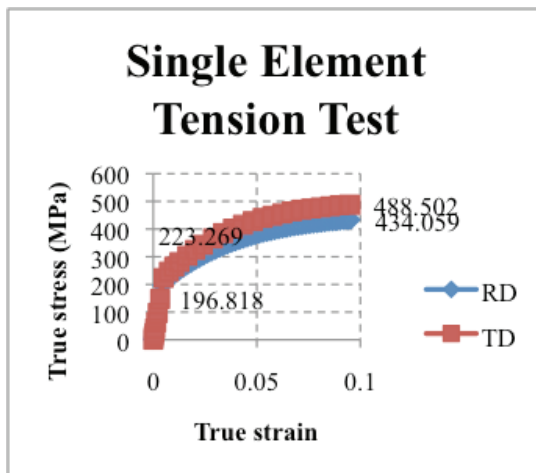
Figure 83. Stress-Strain Curve in Uni-axial Tension Test.
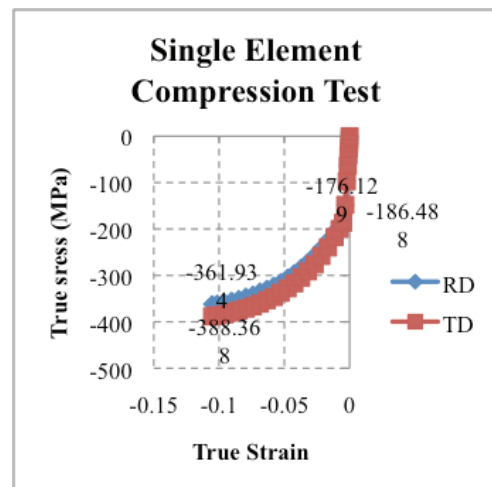
Figure 84. Stress-Strain Curve in Uni-axial Compression Test.

Framework for Multiscale Design of Material-Product Systems Considering Uncertainty

Statistical Volume Element Method for Predicting Microstructure-Constitutive Property Relations

In materials design, there is an inevitable need to establish multi-length scale statistical microstructure-constitutive property relations. In this research, we developed a statistical volume element (SVE) method to analyze, quantify, and calibrate such microstructure-constitutive property relations by statistical means. Statistical volume element simulations are

adopted to predict material constitutive properties corresponding to various realizations of random microstructure configurations. As shown in Figure 85, a computing framework that links random configuration generators and finite element analysis has been developed. A statistical cause-effect analysis approach is proposed to study the influence of random material microstructure on material constitutive properties. Within the proposed approach, statistically significant microstructure parameters are first identified based on their linear impacts on material constitutive properties. Global sensitivity analysis is then employed to provide a more comprehensive importance ranking of these critical microstructure parameters, considering both main and interaction effects. The uncertainties in material constitutive properties due to random microstructure configurations are quantified in terms of distributions, statistical moments, and correlations, as shown in Figure 86. The obtained probabilistic constitutive relations are used to calibrate the model parameters in a constitutive relation model following a statistical calibration process. As shown in Figure 86, with the statistical calibration approach, the obtained probabilistic constitutive relation can be reproduced through a calibrated Bammann-Chiesa-Johnson (BCJ) material model.

Although our approach is currently demonstrated for a single scale microstructure material model, our proposed techniques are generic enough to be applied to more sophisticated multiscale material models in either a hierarchical or a fully coupled (all-in-one) manner. The calibrated material constitutive models that incorporate the uncertainties propagated from random material microstructure will facilitate probabilistic analyses of material performance at the continuum level in multiscale design and analysis. Furthermore, the capability of deriving probabilistic material constitutive relations is essential in the model validation process where the statistical computational results will be compared against random experimental results following the similar statistical model calibration procedure. The capability will also allow designers to assess the reliability of product performance by introducing the statistical representation of material constitutive relations.
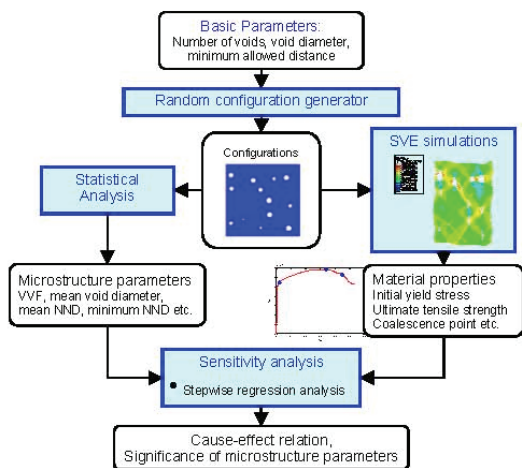
Figure 85. Statistical analysis study of material microstructure-constitutive property relation.
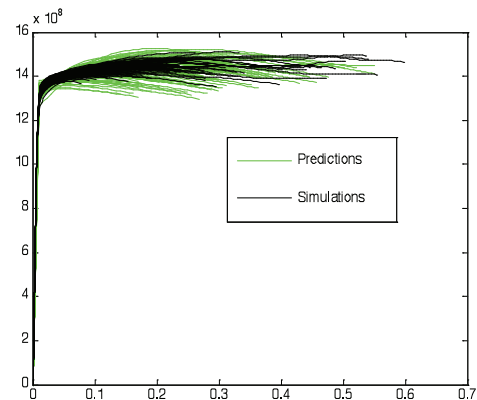
Figure 86. Random predictions/reproductions of the calibrated BCJ model compared to the SVE simulation results.

A Multiscale Design Approach with Random Field Representation of Material Uncertainty

To facilitate product design considering the impact of manufacturing process and material on product performance, a multiscale design approach is developed in our research with an emphasis on the treatment of material uncertainty across a product domain as random field. By integrating manufacturing simulations, multiscale material models, and product models in a multiscale framework, the proposed approach allows either hierarchical or concurrent designs

of manufacturing process, material, and product in a multiscale content. A control arm design problem considering the spatial variation of initial porosity level due to casting process is used to demonstrate the applicability of the proposed approach.

For designing reliable products, uncertainty propagation under the proposed multiscale framework poses a significant computational challenge. An efficient procedure for uncertainty propagation from material random field to end product performance is developed (Figure 87). Material random field is discretized based on the product finite element mesh, and a reduced order Karhunen-Loeve representation is derived from the covariance matrix of the discretized random field, which significantly reduces the dimensionality of random field representation. The univariate dimension reduction method and the Gaussian quadrature formula are applied to efficiently evaluate the statistical moments of the end product performance.

The impact of a material microstructure random field with different correlation lengths on the statistical moments of product performance is studied. It is found that when the correlation parameter approaches infinity, the random field degenerates to a random variable which is uniform across the spatial domain. Based on the empirical study of the control arm design problem, it is discovered that the correlation parameter of input random field has a larger impact on the higher order moments of product performance than on its mean value. Meanwhile, the correlation parameter has a monotonic negative effect on the mean product performance while a larger correlation length causes a greater standard deviation of the product performance.

A reliability-based design of the control arm is demonstrated with the consideration of uncertainty propagation across multiple scales from the material domain to the product domain. Reliable geometry designs of the control arm in terms of wall thicknesses are achieved to minimize the control arm volume while keeping the damage level of the product under specified values. The control arm design example demonstrates the feasibility of the proposed approach with the random field representation of material uncertainty.
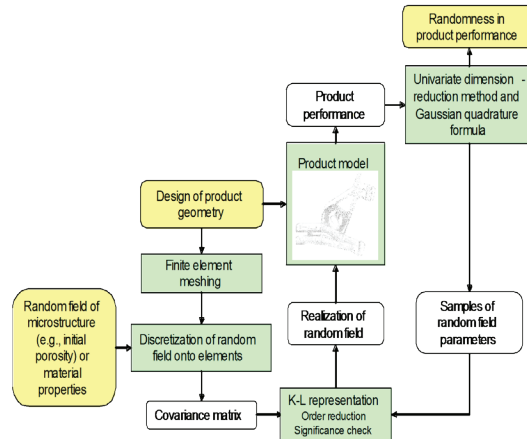
Figure 87. Efficient Random Field Uncertainty Propagation in Design using Multiscale Analysis.

An Enhanced Hierarchical Statistical Sensitivity Analysis Method for Multilevel Systems with Shared Variables

Statistical sensitivity analysis (SSA) is an effective way to examine the impact of variations in model inputs on the variations in model outputs at either a prior or posterior design stage. A hierarchical statistical sensitivity analysis (HSSA) method has been proposed in literature to incorporate SSA in designing complex engineering systems with a hierarchical structure. However, the original HSSA method only deals with hierarchical systems with independent subsystems. Due to the existence of shared variables at lower levels, responses from lower

level submodels that act as inputs to a higher level subsystem are both functionally and statistically dependent. In this work, an enhanced hierarchical statistical sensitivity analysis (EHSSA) method is developed for designing systems with dependent subsystem responses (see Figure 88). A top-down strategy, same as in the original HSSA method, is employed to direct sensitivity analysis from the top level to lower levels. To overcome the limitation of the original HSSA method, the concept of a subset SSA is utilized to group a set of dependent responses from lower level submodels in the upper level SSA. At a lower level, similar to the variance decomposition, the covariance of dependent responses is decomposed into the contributions from individual shared variables. To estimate the global impact of lower level inputs on the top level output, an enhanced aggregation formulation is developed to integrate local subsystem sensitivity analysis results. The importance sampling technique is also introduced to re-use the existing data from submodels SSA during the aggregation process. The effectiveness of the proposed EHSSA method is illustrated and verified via a mathematical example and a multiscale design problem, Figures 89 and 90.
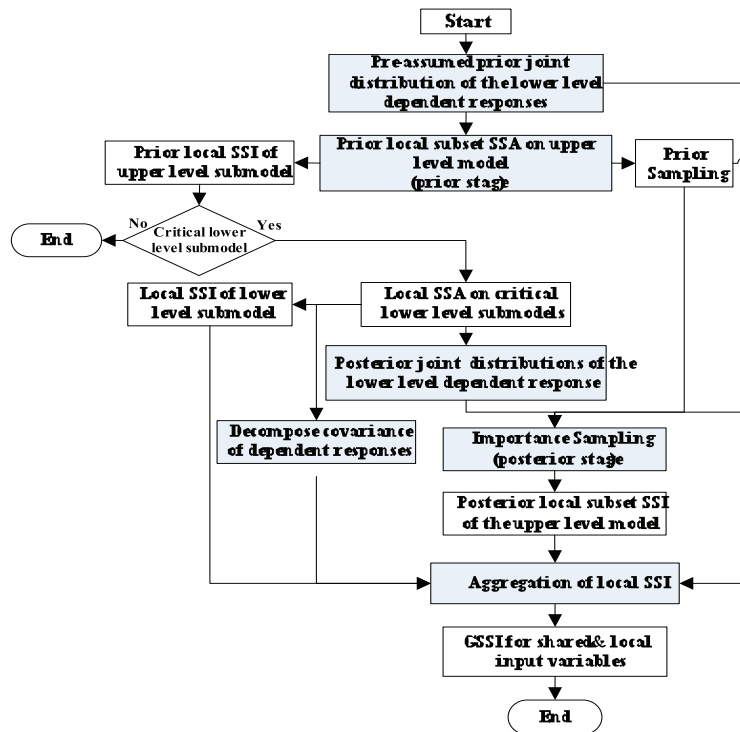
Figure 88. Flowchart of the EHSSA Method with Dependent Lower Level Responses.
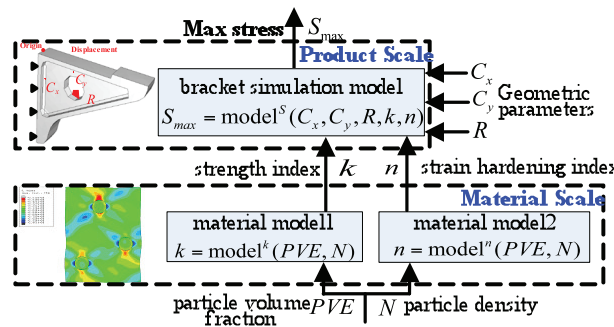
Figure 89. Framework of Multiscale Design System. The product scale is denoted as Scale 1, and the material scale involving two material models is denoted as Scale 2.
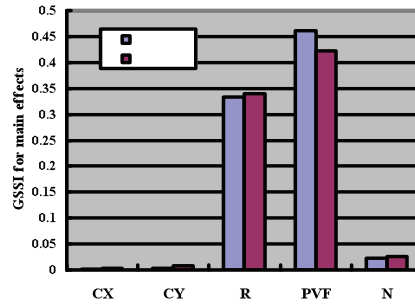
Figure 90. The Global Statistical Sensitivity Index (GSSI) for Main Effect of Each Input Variable.

A Multiscale Design Methodology for Designing Hierarchical Multiscale Systems Considering Random Field Uncertainty

A multiscale design methodology is proposed in this work to facilitate the design of hierarchical materials and product system with the consideration of random field uncertainty that propagates across multiple length scales. Based on the generalized hierarchical multiscale decomposition pattern in multiscale modeling, a set of computational techniques are developed to manage the complexity of multiscale design under uncertainty. Novel design of experiments and metamodeling strategies are proposed to manage the complexity of propagating parameterizable uncertainty and random field uncertainty through three generalized levels of transformation: the material microstructure random field, the material property random field, and the probabilistic product performance. Multilevel optimization techniques are employed to find optimal design solutions at individual scales. A hierarchical multiscale engineering system (see Figure 91) that involves a 2-scale (submicro- and miro- scales) material design and a macro-scale product (bracket) design is used to demonstrate the applicability and the benefits of the proposed methodology.
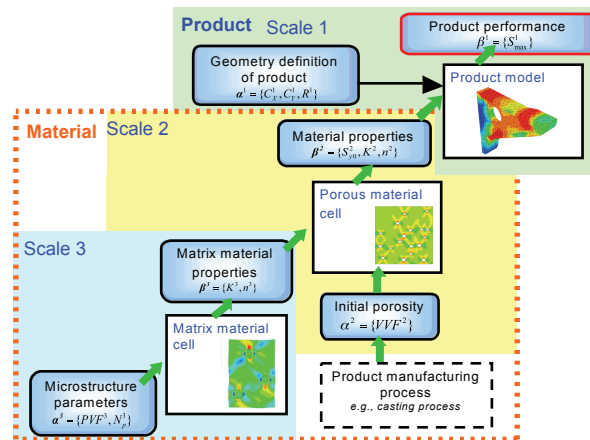
Figure 91. Flowchart of the 3-scale system.

Conclusions

This report summarized the main research activities performed in Task 8 during the period February 1, 2006 – June 30, 2009. Although many of the activities have already been described in two previous annual DOE reports, this final report was self-contained as it described these activities plus the new ones carried out during the last eight months.

In general, the project has delivered results in three main areas: (i) a material database for advance constitutive modeling of wrought aluminum and magnesium alloys, (ii) a multi-scale material modeling approach for the history-dependent mechanical response for these alloys, and (iii) a framework for integrated robust and reliability optimization method with uncertainty for

the design of TMP. Note that many of the activities initiated in this project are being continued at the different institutions in closely related projects. In particular, at MSST the activities on extrusion/sheet forming and multi-scale materials modeling are now part of an ongoing DOE project.

Finally, the technology developed/being developed on this and other related projects is of interest to the Magnesium Front End Research and Development (MFERD) Project. MSST is supporting this project by establishing the science-based knowledge of the extrusion process of magnesium alloys, in particular AM30 and AZ61. Some support on sheet forming modeling of AZ31 is also being provided.

Presentations/Publications/Patents

Conferences Presentations

1. Marin, E.B., "On the Formulation of a Classical Crystal Plasticity Model", Proceeding of the 13th International Symposium on Plasticity and its Current Applications, Girwood, Alaska, June 2-6, 2007.

2. Groh, S., Marin, E.B., and Horstemeyer, M.F., Multiscale Modeling of the Plasticity in Al Single Crystal, 14th International Symposium on Plasticity and its Current Applications, Hawaii, January 2008.

3. Groh S, Marin, EB, Horstemeyer, MF, and Bammann, DJ. Implementation of deformation twinning in a crystal plasticity code. First AAM, New Orleans, June 2008.

4. Marin, E.B., Bammann, D.J., and Horstemeyer, M.F., "On the Numerical Implementation and Applications of an ISV Material Model", The 15th International Symposium on Plasticity and Its Current Applications, St Thomas, US Virgin Islands, Jan 3-8, 2009.

5. Groh S, Marin E.B., Horstemeyer M.F., and Bammann D.J., Dislocation motion in magnesium: A study by Molecular Statics and Molecular Dynamics. The 15th International Symposium on Plasticity and Its Current Applications, St Thomas, US Virgin Islands, Jan 3-8, 2009.

6. Oppedal, A.L., Kaschner, G.C., Capolungo, L., McCabe, R.J., Vogel, S.C., Brown, D.W., C.N. Tomé, C.N., and Horstemeyer, M.F., Modeling texture, twinning, and hardening evolution during strain path reloads in pure Magnesium, TMS 2009, San Francisco, February 15 – 19, 2009.

7. Groh S., Marin E.B., Horstemeyer M.F. and Zbib H.M., Multiscale Modeling of the Plasticity in an Aluminum Single Crystal. USCCM, Columbus (Ohio), July 2009.

8. Chen, S., Chen, W., and Lee, S., "Robust Shape and Topology Optimization of Compliant Mechanisms Considering Random Field Uncertainty", 8th World Congress on Structural and Multidisciplinary Optimization, Lisbon, Portugal, June 1-5, 2009.

9. Chen, S., Lee, S., and Chen, W., "Level Set based Robust Shape and Topology Optimization under random field Uncertainties", ASME 2009 International Design Engineering Technical Conferences & Computers and Information in Engineering Conference, August 30 - September 2, 2009, San Diego, California.

10. Chen, W., Yin, X., Lee, S., and Liu, W. K., "A Multiscale Design Methodology for Designing Hierarchical Multiscale Systems Considering Random Field Uncertainty", DETC2009-87465, Proceedings of the ASME 2009 International Design Engineering Technical Conferences & Computers and Information in Engineering Conference, August 30-September 2, 2009, San Diego, CA.

11. Liu, Y, Yin, X., Arendt, P., Chen, W., Haung, H., "An Enhanced Hierarchical Statistical Sensitivity Analysis Method for Multilevel Systems with Shared Variables", submitted to ASME 2009 International Design Engineering Technical Conferences & Computers and Information in Engineering Conference, August 30 - September 2, 2009, San Diego, California.

12. Yin, X., Lee, S., Chen, W., Liu, W. K., Horstemeyer, M.F., "A Multiscale Design Approach with Random Field Representation of Material Uncertainty", Paper No. DETC2008-49560, Proceedings of the ASME 2008 International Design Engineering Technical Conferences & Computers and Information in Engineering Conference, August 3-6, 2008, Brooklyn, New York. In press, ASME Journal of Mechanical Design.

13. Lee, S., Chen, W., Kwak, B. M. "Robust Design with Arbitrary Distributions using Gauss-type Quadrature Formula", Proceedings of the 12th AIAA/ISSMO Multidisciplinary Analysis and Optimization Conference, September 10–12 2008, Victoria, British Columbia, Canada, in press, Structural and Multidisciplinary Optimization.

14. Huang, Y., Huang, J. and Cao, J., "Experimental study on the mechanical property and forming limit of magnesium sheet at elevated temperatures", ASME 2009 International Manufacturing Science and Engineering Conference, October 4-7, 2009, West Lafayette, Indiana, USA.

Publications

1. Groh S, Marin E.B., Horstemeyer M.F., and Zbib, H.M., Multiscale Modeling of the Plasticity in an Aluminum Single Crystal, International Journal Plasticity, 25 1456-73, 2009.

2. Groh S., and Zbib H.M., Advances in Discrete Dislocations Dynamics and Multiscale Modeling. J. Eng. Mater. Tech., Accepted May 25, 2009.

3. Groh S., Marin E.B., Horstemeyer M.F., and Bammann D.J., Dislocation motion in magnesium: A study by Molecular Statics and Molecular Dynamics. Modelling Simul. Mater. Sci. Eng. Accepted, January 21, 2009.

4. Cao, J., Lee, W. Cheng, H.S., Wang, H. and Chung, K. (2009) "Experimental and Numerical Investigation of Combined Isotropic-kinematic Hardening Behavior", International Journal of Plasticity, Vol. 25, pp.942-972, doi:10.1016/j.ijplas.2008.04.007.

5. Yin, X., Chen, W, Liu, W-K, and To, A., "A Statistical Volume Element Method for Predicting Microstructure Constitutive Relations", Computer Methods in Applied Mechanics and Engineering, 197(43-44), 3516-3529, 2008.

6. Yin, X., Lee, S., Chen, W., Liu, W. K., Horstemeyer, M.F., "Efficient Random Field Uncertainty Propagation in Design using Multiscale Analysis", ASME Journal of Mechanical Design, 131(2), 2009

7. Lee, S. H., Chen, W., and Kwak, B. M., "Robust Design with Arbitrary Distribution Using Gauss-Type Quadrature Formula," Structural and Multidisciplinary Optimization, in press, 2009.

References

1. [Mordike 2001] Mordike BL, Ebert T. 2001. Magnesium – Properties – applications – potential. Mater Sci Eng A;12:37 - 45.

2. [Kelley 1968] Kelley EW, Hosford Jr WF. 1968. Plane-strain compression of Magnesium and Magnesium alloy single crystals. Trans Metall Soc AIME;242:5 -13.

3. [Christian 1995] Christian JW, Mahajan S. 1995. Deformation twinning. Prog Mater Sci;39:1-157.

4. [Marin 2006] Marin EB. 2006. Sandia National Laboratories, CA; SAND2006-4170.

5. [Hughes 2000] Hughes D, Bammann DJ, Codfrey A, Prantil V, Holm E, Miodownik M, Chrzan D, and Lusk M. 2000. Sandia National Laboratories, CA; SAND2000-8232.

6. [Groh 2008] Groh S, Marin EB, Horstemeyer MF, and Zbib HM (in press). Int J Plast.

7. [Sun 2006] Sun SL, Mendelev MI, Becker CA, Kudin K, Haxhimali T, Asta M, Hoyt JJ, Karma A, and Srolovitz, DJ. 2006. Phys Rev B;73:024116-1-12.

8. [Hirth 1992] Hirth JP, Lothe J. Theory of dislocations. Malabar (FL): Krieger Publishing Company.

9. [Conrad 1957] Conrad H, Robertson WD. 1957. AIME 209;503.

10. [Reed-Hill 1957] Reed-Hill RE, Robertson WD. 1957. Acta Metall;5: 717-27.

11. [Staroselsky 2003] Staroselsky A, Anand L. 2003. Int J Plast;19:1843-64.

12. [Liu 1996] Liu XY, Adams JB, Ercolessi F, and Moriarty JA. 1996. Modell Simul Mater Sci Eng;4:293- 303.

13. [Kelley and Hosford 1968] Kelley EW, Hosford Jr WF. 1968. Trans Metal Soc AIME;242:5-13.

14. [Nave 2004] Nave MD, Barnett MR. 2004. Scripta Mater;51:881-85.

15. [Barnett 2007] Barnett MR. 2007. Mat Sci Eng A;464:1-7.

16. [Kalidindi 1998] Kalidindi SR. 1998. J Mech Phys Solids;46:267-71.

17. [Salem 2005] Salem AA, Kalidindi SR, Semiatin SL. 2005. Acta Mater;53: 3495-3502.

18. [Rudd 2002] Rudd RE, Belak JF. 2002. Comp Mater Sci;24:148-53.

19. [Seppala 2004] Seppala ET, Belak J, Rudd RE. 2004. Phys Rev B;69:134101.

20. [Lubarda 2004] Lubarda VA, Schneider MS, KalantarDH, et al. 2004. Acta Mater;5:1397-408.

21. [Belak 1998] Belak J. 1998. J Compu-Aided Mater Des;5:193-206.

22. [Traiviratana 2008] Traiviratana S, Bringa EM, Benson DJ, et al. 2008. Acta Mater;56:3874-86.

23. [Groh 2009] Groh S, Marin EB, Horstemeyer MF, and Bammann DJ. In review.

24. [Sun 2006] Sun DY, Mendelev MI, Becker CA, et al. 2006. Phys Rev B;73: 024116-1-12.

25. [Perrot 1992] Perrot G, Cheng B, Gibson J, et al. 1992. J Comput Chem; 13:1-11.

26. [Sanner 1996] Sanner MF, Spehner JC, Olson AJ. 1996. Biopolymers;38:305-20.

27. [Rudd 2007] Rudd RE, Seppala ET, Dupuy LM, et al. 2007. J Compu-Aided Mater Des;14:425-34.

28. [Horstemeyer 2000] Horstemeyer MF, Lathrop J, Gokhale AM and Dighe M. 2000. Theo Appl Frac Mech;33:31-47.

29. [Beyerlein 2008] Beyerlein IJ, Tomé CN. 2008. A dislocation-based constitutive law for pure Zr including temperature effects. Int J Plast;24: 867-95.

30. [Lebensohn 1993] Lebensohn RA, Tome CN. 1993. A self consistent approach for the simulation of plastic deformation and texture developmentof polycrystals: Application to Zirconium alloys. Acta Metallurgica et Materialia; 41:2611-24.

31. [Molinary 1987] Molinari A, Canova GR, Ahzi S. 1987. A self consistent approach of the large deformation polycrystal viscoplasticity. Acta Metallurgica;35:2893 – 2994.

32. [Kocks 1998] Kocks UF, Tomé CN, Wenk HR. 1998. Texture and anisotropy. Cambridge: Cambridge University Press.

33. [Sarma 1998] Sarma GB, Radhakrishnan B, Zacharia T. 1998. Comput Mater Sci;12:105-23.

34. [Radhakrishnan 1998] Radhakrishnan Sarma BG, Zacharia T. 1998. Acta Mater;46:4415-33.

35. [Radhakrishnan 2000] Radhakrishnan Sarma BG, Weiland H, Baggethun P. 2000. Model Simul Mater Sci Eng;8:737-750.

36. [Radhakrishnan 2004A] Radhakrishnan Sarma BG. 2004. Phil Mag A;22:2341-66.

37. [Radhakrishnan 2004B] Radhakrishnan B, Sarma G. 2004. JOM;56:55-62.

38. [Crumbach 2004] Crumbach M, Goerdeler M, Gottstein G, Neumann L, Aretz H, and Kopp R. 2004. Model Simul Mater Sci Eng;12:S1-S18.

39. [Radhakrishnan 2008] Radhakrishnan B, Sarma G. 2008. Mater Sci Eng A;494:73-79.

40. [Theyssier 1999] Theyssier MC, Driver JH. 1999. Mater Sci Eng A;272:73-82.

41. [Ridha 1982] Ridha AA, Hutchinson WB. 1982. Acta Metall Mater;30:1929-39.

42. [Humphreys 1995] Humphreys FJ, Hatherly M. 1995. Recrystallization and related annealing phenomena. 1st ed. Elsevier, New York. p. 335-7.

43. [Barnett 1999] Barnett MR, Kastens L. 1999. ISIJ Inter;39:923-9.

44. [Yoshinaga 1998] Yoshinaga N, Vanderschueren D, Kestens L, Ushioda K, and Dilewijns J. 1998. ISIJ Inter;38:610-6.

45. [Liu 1998] QLiu Q, Juul Jensen D, Hansen N. 1998. Acta Mater;46:5819-38.

46. [Sarma 1996] Sarma G, Dawson PR. 1996. Int J Plast;12:1023-54.

47. [Swift 1952] Swift HW. 1952. J Mech Phys Sol;1:1-18.

48. [Keeler 1964] Keeler SP, Backofen WA. 1964. ASM Trans Quart;56:25-48.

49. [Marciniak 1967] Marciniak Z, Kuczynski K. 1967. Int J Mech Sci;9(9): 609-20.

50. [Cao 2002] Cao J, Yao H. 2002. Int J Plast;18(8):1013-38.

51. [Wang 2000] Wang X, Cao J. 2000. Int J Mech Sci;42(12):2369-94.

52. [Du 2000] Du X, Chen W. 2000. ASME J Mech Design;122(4):385-94.

53. [Cazacu 2005] Cazacu O, Plunkett B, Barlat F. 2005. Orthotropic yield criterion for hexagonal closed packed metals. Int J Plast.

54. [Kim 2008] Kim J, Ryou H, Kim D, Kim D, Lee W, Hong SH, and Chung K. 2008. Constitutive law for AZ31B Mg alloy sheets and finite element simulation for three point bending.

B. Development of High-Volume Warm Forming of Low-Cost Magnesium Sheet

Principal Investigator: Peter Friedman
Ford Motor Company
Ford Research and Innovation Center
2101 Village Road, MD 3135
Dearborn, MI 48121-2053
Phone: 313-248-3362; e-mail: pfriedma@ford.com

Principal Investigator: Paul Krajewski
General Motors Corporation
GM, R&D and Planning
Mail Code 480-106-212
30500 Mound Road
Warren, MI 48090-9055
Phone: 586-986-8696 ; e-mail: paul.e.krajewski@gm.com

Principal Investigator: Jugraj Singh
Chrysler Corporation LLC
Body Materials Engineering
Mail Code 482-00-11
800 Chrysler Drive
Auburn Hills, MI 48326-2757
Phone: (248) 512-0029 ; e-mail: js329@chrysler.com

Technology Area Development Manager: William Joost
(202) 287-6020; e-mail: william.joost@ee.doe.gov

Field Project Officer: Magda A. Rivera
(304) 285-1359; e-mail: magda.rivera@netl.doe.gov

Contractor: U.S. Automotive Materials Partnership
Contract No.: DE-FC26-02OR22910

Objective

Develop the technology and material supply base for cost-effective lightweight body panels fabricated from sheet magnesium. A warm forming system will be designed and built to develop a suitable process for forming magnesium sheet as well as a test bed to evaluate potential low cost magnesium sheet from various global producers. Specific deliverables from this project will include the following:

- Design and build a warm forming die and demonstrate a deep draw capability on conventional direct chill (DC) material.

  Demonstrate pan forming of at least 100mm.

- Evaluate materials and compare the formability of continuous cast (CC) and direct chill (DC) materials.

  Evaluate high temperature elongation, which is equal or greater in CC material compared to DC material.

- Demonstrate high volume cycle times with CC material on an integrated forming cell.

  Part to part cycle time with CC material of 5-10 jpm (jobs per minute).

Approach

- Continuous casting (CC) is a key technology for enabling the development of low cost Mg sheet. This project will drive material development in the supply base by giving them a mechanism for evaluating materials. The project will receive material from major global magnesium suppliers including Magnesium Elektron, CSIRO, ThyssenKrupp, LY Copper, and POSCO. These materials will be characterized via tensile testing at the University of Virginia, biaxial forming at CANMET, and through stamping trials at Troy Tooling Technologies.

- Novel die systems will be designed and constructed that enable the use of warm forming in a conventional single-action press. The die will be used to determine critical forming parameters for magnesium sheet including lubricant thickness preheat temperature, die temperature, forming speed, etc. The forming windows for the different materials will be determined to see the effect of processing via different methods, e.g. continuous casting vs. ingot (DC) casting.

- Full automation including loading of pre-heated sheet and part extraction will be developed to achieve acceptable cycle times (5-10 jpm) demonstrating the high volume feasibility of warm forming.

Accomplishments

- Completed AMD602 project, meeting all timing and deliverables.

- Completed full-scale forming trial and determined a forming window for Mg sheet with respect to temperature, binder pressure, lubricant and blank size.

- Developed fully-automated warm forming cell capable of demonstrating the process under run-at-rate conditions at 5 jobs per minute for both aluminum and magnesium.

Future Direction

- AMD602 project has been completed.

- A new follow-on project, Optimization of High-Volume Warm Forming for Lightweight Sheet Alloys has been proposed to USAMP and DOE.

Introduction

The major barrier to the application of magnesium sheet components in vehicle structures is a combination of two factors: the limited formability of magnesium sheet and the cost of producing the sheet itself. Warm forming processes similar to those demonstrated in aluminum with the USAMP Warm Forming Project (AMD307) can be used to significantly improve the formability of magnesium sheet. This project is leveraging the accomplishments of the AMD307 Warm Forming project to develop equipment, lubricant, simulation, and forming equipment for the cost effective forming of magnesium sheet. A warm forming cell based on the lessons-learned of AMD307 will be designed and built to demonstrate the efficient forming of magnesium sheet. The target application for this process is deep draw panels with specific interest in door inners.

The cost of magnesium sheet is driven by the high conversion costs of rolling an ingot into sheet form. This is a direct result of the HCP (hexagonal close packed) structure of magnesium that requires the sheet to be rolled in small increments often with annealing steps between rolling passes. Continuous casting is a technology with the potential to reduce this cost dramatically. By casting directly into sheet form, continuous casting offers a higher production rate, a smaller capital investment, and significantly less energy and labor as compared with the conventional direct-chill (DC) ingot-casting process. The opportunities for decreasing the cost of magnesium sheet via continuous casting have been described by Hunt et.al in their 2005 report to the DOE. Suppliers globally are working on developing continuous casting technology. In this project, all of the major global magnesium suppliers will be included to determine if their materials are suitable for the warm forming process. The new warm forming system will be used as a standard test bed for the evaluation of these materials as well as new magnesium sheet materials produced in the future.

Material Characterization

Material

The project includes magnesium sheet from five major global magnesium suppliers. This includes two DC-Casters (Magnesium Elektron and ThyssenKrupp) and three continuous casters (CSIRO, Yinguang, and POSCO). Four suppliers have provided 100 blanks of 1 mm x 600 mm x 600 mm of AZ31B-O material. The laboratory tensile and biaxial forming results from University of Virginia and CANMET were reported previously in the 2008 annual report and are summarized in detail in the AMD602 final report.

Press Forming Trials

The focus of the material characterization efforts for 2009 was developing the press forming capability of the five different magnesium sheet materials. Prior work, which was reported in AMD602 2008 Annual Report, demonstrated that the continuously cast materials provided comparable mechanical behavior to the ingot cast materials. The goal of the press forming trials was to see whether continuously cast materials gave comparable press forming performance. The press forming trials were performed on the die setup as shown in Figure 1 below. The pan is 300 mm x 400 mm with 50 mm corner radii. The depth can be varied from 0 to 125 mm. The binder pressure was applied using nitrogen cylinders that could be varied between 0 and 1500 psi. The die was designed to enable thermal uniformity across the tool, as well as thermal isolation from the press and the operators. Blanks were trimmed and coated with a boron nitride containing lubricant developed by Fuchs Lubricant Company for the project. The lubricant was sprayed on the blanks at a thickness of 1800 mg/sq ft by Jay and Kay Manufacturing.

(a)

(b)

(c)

(d)

Figure 1. Photographs of the die and press used for the press formability material evaluation trials showing (a) pan die cavity, (b) assembled die with punch in place, (c) press and die in forming position and (d) fully formed magnesium pan, 125 mm deep.

For the press formability trials, the depth of the pan was set to 70 mm. This depth was determined by the narrowest width material available. All trials were performed isothermally. The die was set for the desired temperature, a lubricated blank was inserted into the die, when the blank reached the temperature of the die, the press was activated and the panel formed. Test temperatures were 175C, 200C, 225C, 250C, 275C, 300C, 325 C, and 350C. The press speed was 40 mm/sec. Binder pressure was varied between 500 and 3000 psi / corner or 2000 to 12000 psi total. The combination of temperature and binder pressure led to a 2 dimensional space to evaluate and compare formability.

The trials were performed on all five materials at a given combination of temperature and binder pressure to insure that the conditions were the same for each material. The panels were evaluated after forming and cooling to room temperature to determine (a) whether each corner successfully formed or split and (b) whether the amount of wrinkling was excessive. Wrinkling was measured as the height of the wrinkled metal from the flat bench surface W (as shown in Figure 2 below) minus the thickness of the material. Draw-in for each panel was measured along the width, length, and diagonal of the panel and reported as the difference between the starting rectangular blank and the final shape of the flanges on the formed pan. The details of the draw-in measurements are shown in Figure 3.
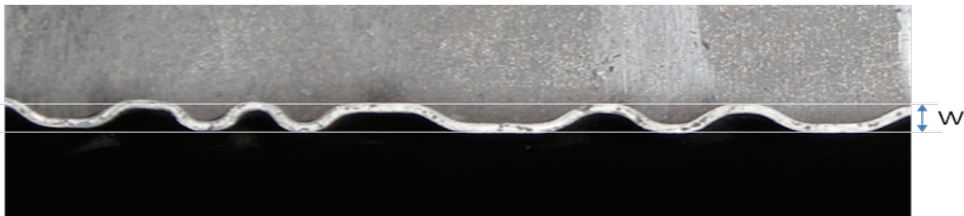
Figure 2. Photograph of wrinkled edge on a formed pan demonstrating the dimension W used to measure the degree of wrinkling. (Metal thickness was subtracted from W for the presented result).
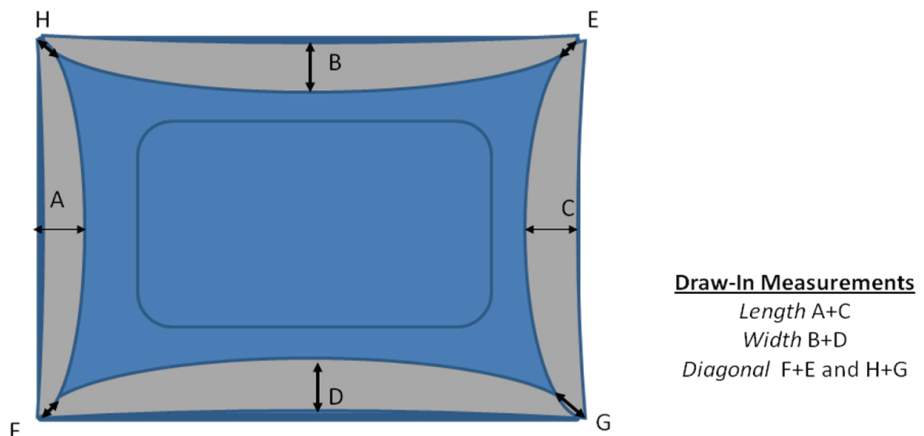
Figure 3. Schematic illustrating the measurements made to calculate the amount of draw-in during forming.

The degree of fracture in failed samples was measured as shown below. The width of the crack opening can be used to determine the draw depth at fracture as:

$$\text{fracture depth} = 70 \text{ mm} - t_{max}$$

where t_{max} is the largest crack opening on the four corners of the pan (see Figure 4). This data will be used and analyzed in more detail for the ICME projects AMD702 and 703 to develop failure criteria for warm forming.
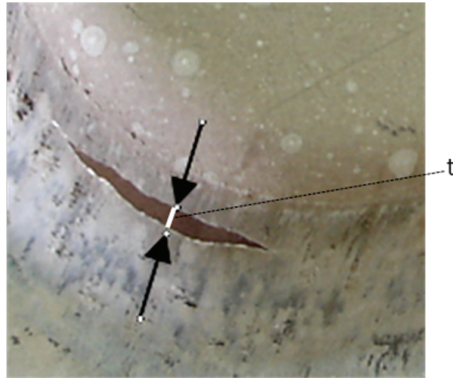
Figure 4. Photograph of split region in the corner wall of a pan demonstrating the measurement of crack opening.

The forming windows are shown for each of the five materials in the following three figures(Figures 5,6,7). Below each figure is a brief summary of the forming window for that material. In each forming window, orange data points (◆) depict the conditions under which the panes show wrinkling, red points (■) depict the conditions under which pan splits, and, green (●) data points signify good stampings with no wrinkling (<0.4 mm wrinkle height) and no splits. These points represent an average of two trials under most conditions. An overall summary and comparison of the materials is given after the individual summaries.

Material A has two separate forming windows where successful panels can be made. The first exists at the highest temperatures, 325C and above. This is a robust window with a wide range of binder pressures possible. The binder pressure range expands toward lower values as temperature is raised from 325C to 350C. The second window exists at lower temperatures, and is disjointed from the higher temperature forming window. A robust binder pressure window exists between 200C and 225C. Successful pans were formed as low as 175C, although the second window was more robust at 200C and 225C.
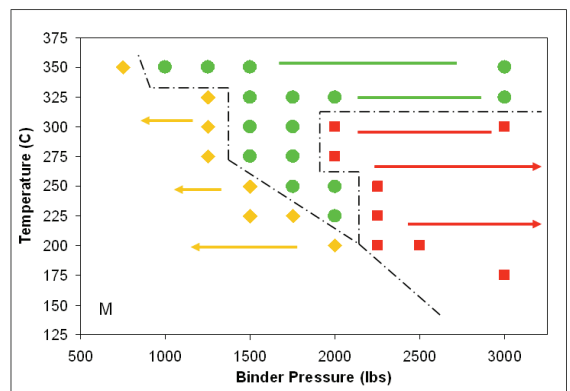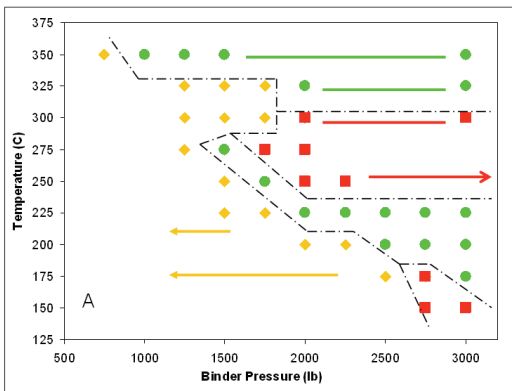
Figure 5. Forming window as a function of temperature and binder force for sheet from source 'A' and 'M'.

Material M shows a single forming window that extends from 225C up to 350C. As the temperature increases, the window of binder pressure that can be used increases producing a wider window. However, no successful pans were made at 175C or 200C.
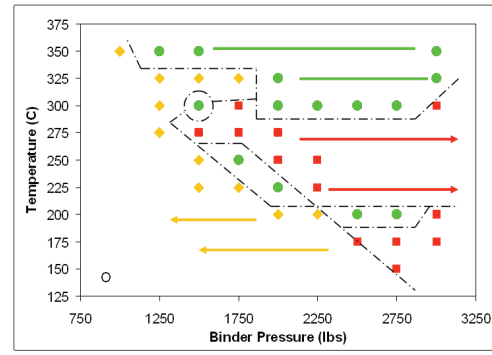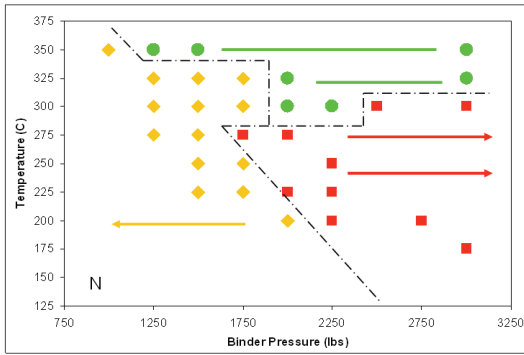
Figure 6. Forming window as a function of temperature and binder force for sheet from source 'N' and 'O'.
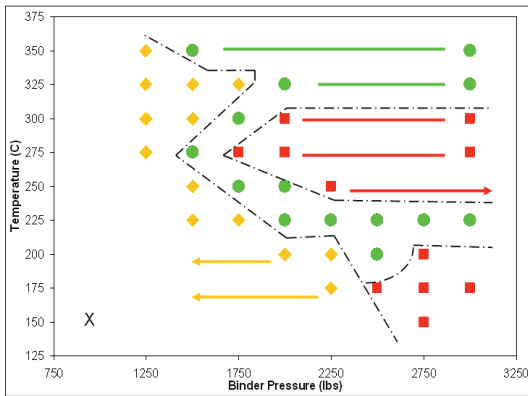
Figure 7. Forming window as a function of temperature and binder force for sheet from source 'X'.

Material N had the smallest forming window of any of the magnesium sheet materials investigated. A robust window was observed only between 325C and 350C. A limited binder pressure range exists at 300C; however, there is no forming window below 300C.

Material O has an excellent forming window at and above 300C. Similar to the other materials there is a wide range of binder pressures where a successful part can be made that increases with increasing temperature. Below 300C there is no contiguous region of successful forming. There are a few spots where good panels were made, down to as low as 200C. This shape is similar to the window for material A but with much less robustness at the lower temperatures, and no successful forming at 175C.

The warm forming behavior of material X is similar to material A. There are two robust windows, one at high temperature (> 300C), and another one at low temperatures around 225C. Unlike A, X could form pan successfully within the entire temperature range of 200 C to 350C, forming a somewhat contiguous window. However no successful pans were made at 175C.

As shown above, forming windows were developed for the five different materials evaluated in this project. All five materials exhibited a robust forming window above 300C. The materials could be stamped in to a 70 mm deep pan without wrinkling or splitting. An example of a successful pan for each material is shown in Figure 8 below, for pans formed at 350C.

Figure 8. Pans stamped at 350C for all five materials in the present study. All pans were formed without splits or excessive wrinkles.
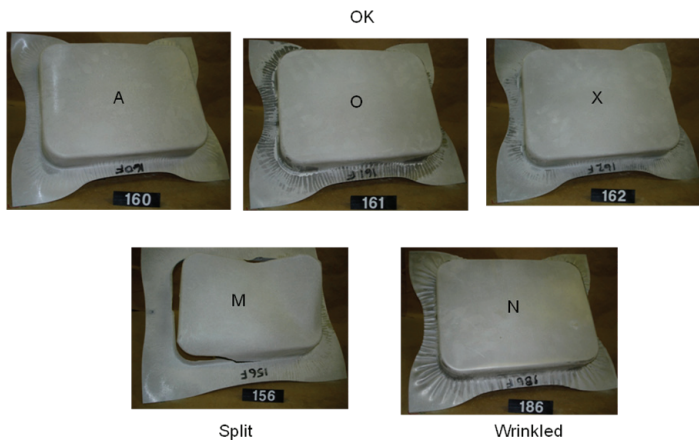
Figure 9. Pans stamped at 200C and 2500 psi for all five materials in the present study. Materials A, O, and X could make a successful part, while M and N could not.

At low temperatures, between 200C and 225C, significant differences in behavior were observed. Pans formed at 200C and 2500 psi are shown in Figure 9. Materials A, X could form pan successfully in this temperature range and had a rather robust window. Material A could be formed as low as 175C. Material N could not be formed at these lower temperatures, and while panels could be formed as low as 200C in materials O and M, the windows were much less robust. An example of this difference in behavior is shown for the five pictures in Figure 9 taken of panels formed at 200C and 2500 lbs. Three materials could make a successful part, one exhibited splitting and the other suffered wrinkling.

As shown above, forming windows were developed for the five different materials evaluated in this project. In those figures, materials were identified as wrinkled or not, using a simple criterion that said if wrinkle height (W-t_{metal}) was greater than 0.4 mm then the stamping was considered to be wrinkled. However, since exact wrinkle measurements were made for all hits, a more detailed comparison of wrinkling is presented below. Five conditions were examined to include a range of temperatures and binder conditions. Clearly, for all materials, the extent of wrinkling increases with decreasing temperature. Material N exhibited the most wrinkling among all materials under all conditions of temperature and binder pressure. This may help explain its poor forming performance compared to the other materials. Previous work by Pf. Agnew at the University of Virginia showed more anisotropy of r value for material N compared to all other materials.
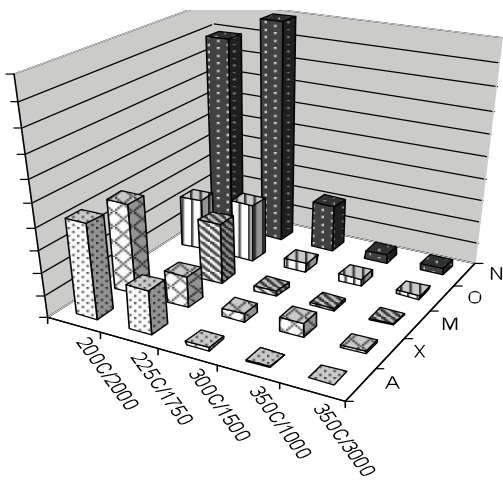
(a)
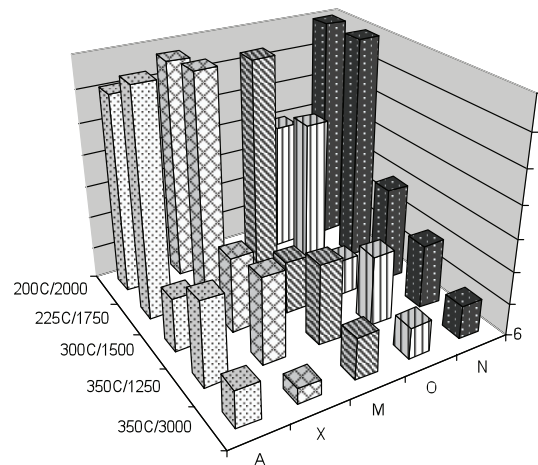
(b)

Figure 10. (a) Wrinkling response of different materials under various forming conditions. (b) Draw-in values for same set of pans for which wrinkling data is shown in (a).

As shown above, the amount of draw-in was measured for each material after each forming trial. This was a comparison between the starting blank size and the resultant shape. This parameter is often used in the metal stamping industry to calibrate formability analyses. All materials exhibited very similar draw-in values as shown in Figure 11. Draw-in value is high at low temperatures and decrease at temperatures 300C and above. At low temperatures, these materials experience heavy wrinkling. Under these wrinkling conditions, the material in the addendum not only has to feed the draw into the die, but also has to contribute towards the continuous growth of the wrinkles during the forming stroke. On average the wrinkled pans had 10% more draw-in than non-wrinkled ones. Also, for conditions when wrinkling was absent, the amount of draw-in decreased with increases in temperature. This can be attributed to the drop in flow strength of the material and resultant higher contribution of material stretch to the overall draw depth. The amount of wrinkling and draw-in are compared below for all of the five materials. The key message for these graphs are that the material N clearly exhibits more wrinkling than the other materials, even when the amount of drawn in is similar, suggesting that a difference in texture is the likely cause of the wrinkling.
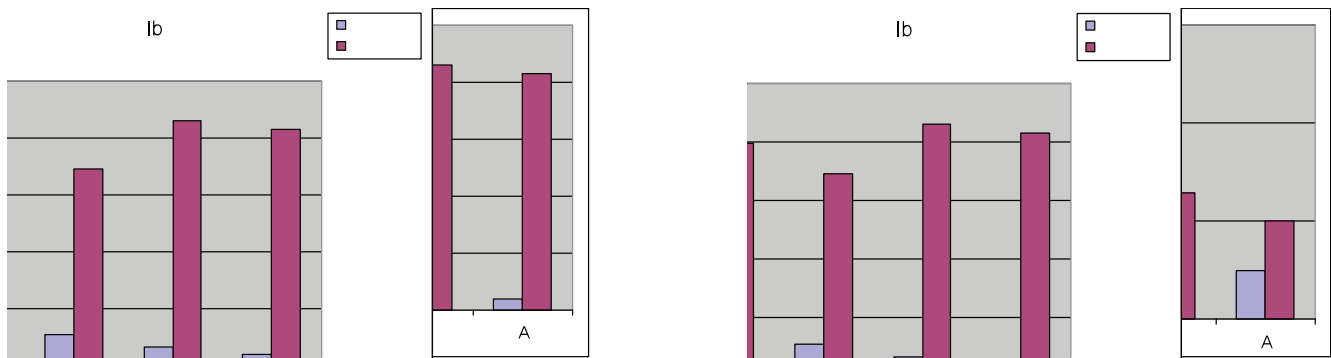
(a)   (b)

Figure 11. Comparison of wrinkling height and draw-in both in mm for pans with no splits under two forming conditions, (a) at 350C and 3000lb binder pressure, where extent of wrinkling is low, and (b) at lower temperatures under heavy wrinkling conditions. Note: Draw in = (Average Draw value − 62)/10.

The press forming results can be summarized with the following conclusions:

- Successful pans could be made with all AZ31 materials included in the present study.

- The deliverable of demonstrating comparable formability between DC and CC materials was achieved as the CC material A was the best performing material.

- Two regimes of forming were observed.

   A robust, high temperature regime at 325C and 350C where all materials could form a good part

   A less robust, low temperature regime at 200C and 225C where some materials could not form a good part.

   Material N was clearly the worst performing material, showing no lower temperature forming window. This is likely due to anisotropy in the sheet as evidenced by texture and R value, as well as a lower ductility than the other materials in this temperature regime.

High-Volume Warm Forming System

The third deliverable for this project and the focus of much of the work in 2009 was the development of an integrated forming cell which could produce warm formed panels at high volume (5-10 jpm). The integrated system used the die and press from Figure 1. Many details of the press and die are summarized in the AMD602 final report. A conveyor type oven was selected for heating the blanks prior to forming. These types of ovens (or furnaces) are common in a number of applications including the hot stamping of boron steel where a sheet is presented to the die at approximately 950C every few seconds.
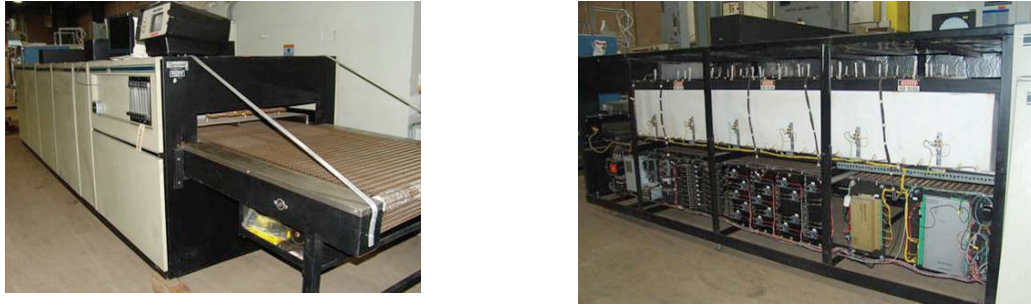
Figure 12. Photographs of the conveyor pre-heater used in the development of the warm forming cell.
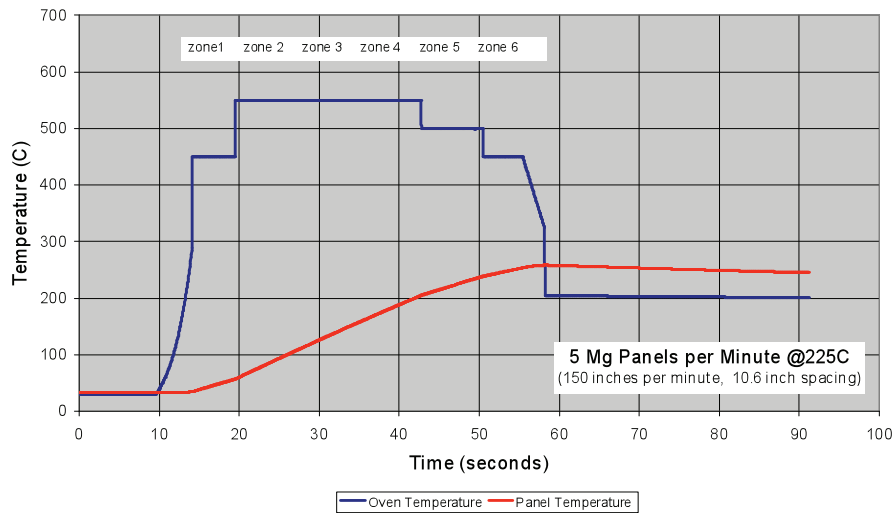
Figure 13. Set temperature of the furnace and corresponding blank temperature as the blank travels through the furnace to support the forming of 5 magnesium panels per minute at 225C.

Selection of the optimal oven design/system should be based on part size, production rate (volume) and the required thermal profile. In this work, a conveyor oven originally designed for sintering was retrofitted to heat blanks to the target forming process as they are carried through on a conveyor. Photographs of the retrofitted unit for this application are shown in Figure 12. The oven used in this work consisted of six heating zones and one cool-down zone. The cool-down zone is obviously not desirable for the warm forming process. In this work, the cool down zone was heavily insulated to minimize heat loss. Thermal simulation was conducted to set the oven zones to target temperatures to achieve a blank at 25°C as it exits the pre-heater at a rate of 5 parts per minute. Figure 13 shows the thermal trace of both the oven and the subsequent temperature of the blank. Note the oven was set significantly above the final blank target temperature to achieve the final forming temperature.

Figure 14. Photograph of the forming cell with robot and end effector.

The movement of blanks from the pre-heater to the press was accomplished with a 6-axis Fanuc robot. As shown in Figure 14, the robot was positioned between the pre-heater and the press to allow for quick and efficient movement of the blank. The strategy employed was to push the formed part off the die into a chute in the same motion in which the new blank was being placed on the die. The robot was equipped with an end effector comprised of two suction cups to lift the blank and push rods to move the prior formed part off of the blankholder. The two suction cups are designed from high temperature cloth to withstand the elevated temperatures. While robust to the elevated temperatures, this type of suction cups does not create a perfect seal. To accommodate the subsequent air losses, the suction cups are attached to air amplifiers that take compressed air and create high flow suction. This creates a very secure lift which also allows for quick release of the blank once the robot attains the correct position over the blankholder.
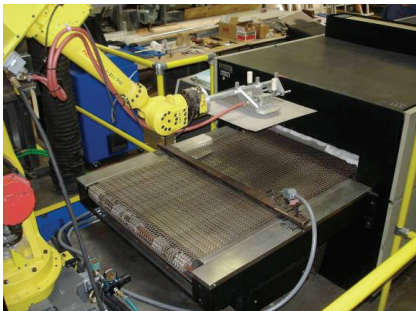
(a)

(b)

(c)

(d)

Figure 15. Photographs of the forming cell showing (a) blank entering the pre-heater, (b) blank triggering the proximity switch, (c) robot transferring the blank from the pre-heater to the forming die and (d) end effector placing the blank on the die while simultaneously pushing a formed part off the blankholder.

The automated process is based on a series of switches connected to a robot PLC. Blanks are first placed on the conveyor and an interlocked, pneumatically controlled gate holds the sheet in place [Figure 15(a)]. This gate is opened to allow the blank to proceed into the oven each time the press is cycled. This ensures an equal pitch (e.g. blank spacing) in the oven that when matched with the belt speed produces the overall system cycle time. As the blank reaches the end of the pre-heater it triggers a proximity switch which instructs the robot to retrieve the blank as noted in Figure 15(b). This switch enables the robot to lower onto the blank and pick up the sheet [Figure 15(c)]. The sheet is quickly shuttled into the press in such a manner that it is always parallel to the ground to minimize heat loss from convection. As the sheet is placed in the die, the push bar shown in Figure 15(d) pushes the last formation off the die blankholder down a chute (not shown). The robot then places the new, heated blank on the blankholder and exits the press. As it exits the press it triggers another proximity switch that gives the permissive to cycle the press.

The process was exercised using both magnesium and aluminum panels. A 10 panel run at rate was performed with a nominal cycle time of 4 jpm. This was slightly slower that he 5-10 jpm target. However this speed was solely due to the ability of the preheater to present a hot blank at the appropriate rate. If a heat with either higher temperature capacity or a longer oven were used, the faster forming speed would be easily attainable. This forming cell represents the first known experimental warm forming prototype cell enabling controlled forming experiments to be performed which aren't susceptible to variations in temperature due to the inconsistency of loading associated with a manual operation.

Acknowledgements

C. Electromagnetic Forming of Aluminum Sheet

Principal Investigator: Richard W. Davies
Pacific Northwest National Laboratory
P.O. Box 999, Richland, Washington 99352
(509) 375-6474; e-mail: rich.davies@pnl.gov

Industry Consultant: Sergey Golovashchenko
Ford Motor Company
Ford Research Laboratory, Dearborn, Michigan 48121-2053
(313) 337-3738, e-mail: sgolovas@ford.com

Participants: Nick Bessonov, EMF Simulations, University of Michigan-Dearborn,
Jeffrey Johnson, EMF System and Control, Pacific Northwest National Laboratory
Vladimir Dmitriev, EMF R&D, Ford Motor Company

Technology Area Development Manager: William Joost
(202) 287-6020; email: william.joost@ee.dov.gov

Field Technical Manager: Mark T. Smith
(509) 375-4478; e-mail: mark.smith@pnl.gov

Contractor: Pacific Northwest National Laboratory
Contract No.: DE-AC05-76RL01830

Objective

To develop electromagnetic forming (EMF) technology that will enable the economic manufacture of automotive parts made from aluminum sheet. EMF is a desirable process because the dynamic nature of the deformation results in benefits, including increased forming limits and reduced springback. These benefits would result in increased use of aluminum and more fuel-efficient vehicles due to mass reduction.

Approach, including industry participants/collaborator and path to technology transfer and commercialization

- The project will address four main technical areas: i) analysis methods for forming system design, ii) development of durable actuators (coils), iii) industrial embodiment of the EMF process, and iv) modeling tools for simulation of the EMF forming process.

- Ford Motor Company is the industry participant and has provided materials, forming tool and forming coil designs, EMF operating requirements, and performed EMF of automotive-size components for test and demonstration.

- Ford has provided funding support in conjunction with Pacific Northwest National Laboratory (PNNL) for EMF model development at Oakland University (Oakland, Michigan) and has provided experimental results for validation of modeling codes.

- The development and validation of modeling codes for EMF and durable coils are key technical barriers for EMF that have been successfully addressed by this project.

Accomplishments

- *Milestone 1: There were no milestones for PNNL during FY 2009 since the EMF project is complete.*

- During the last year of the project, remaining funds were directed at completing documentation of the EMF modeling code approaches for reduced computational run times. This work was funded through a subcontract with Oakland University, and final work was completed in early FY 2009.

- Modeling of sheet-die interaction during EMF was completed during the reporting period, and the results of this work were presented (and published) at the Third International Conference on High Speed Forming.

Future Direction

- This project is complete and final results are documented in this report.

Introduction

In the electromagnetic forming (EMF) process, a transient electrical pulse of high magnitude is sent through a specially designed forming coil by a low-inductance electric circuit. During the current pulse, the coil is surrounded by a strong transient magnetic field. The transient nature of which induces current in a nearby conductive workpiece that flows opposite to the current in the coil. The workpiece and coil act as parallel currents through two conductors to repel one another. The force of repulsion can be high, equivalent to surface pressures greater than ten of thousand pounds per square inch. Thin sheets of material can be accelerated to high velocity in a fraction of a millisecond.

A recent interest in understanding the EMF of metals has been stimulated by the desire to use more aluminum in automobiles. The high workpiece velocities achievable using this method enhances the formability of materials such as aluminum. Additionally, the dynamics of contact with the forming die can help reduce or mitigate springback, an undesired effect that cannot be avoided in other forming techniques such as stamping. The commercial application of this process has existed since the 1960s with the majority of applications involving either the expansion or compression of cylinders (tubes). The forming of sheet materials is considerably more complex and receives relatively little attention.

Approach

The project addresses three main technical areas. The first involves establishing analysis methods for designing forming systems. These methods will be based on developed knowledge of forming limits and relations between electrical system characteristics and deformation response for specific aluminum alloys of interest. The second area is coil durability. Existing EMF and relevant knowledge from pulsed power physics studies will be combined with thermo-mechanical analyses to develop durable coil designs that will be tested experimentally. The third technical area involves the industrial embodiment of the EMF process. In this project, EMF is expected to be hybridized with conventional sheet metal stamping. Different approaches to hybridization will be analyzed for issues affecting the economic implementation in a modern stamping plant, and different system concepts will be developed and studied. Existing knowledge of the EMF

process and technical achievements in this project will be combined to establish a methodology for designing hybrid-forming systems that can be readily integrated into modern manufacturing facilities for the economic production of automotive sheet aluminum components.

Some of the project focus areas and results are discussed in the following sections.

PNNL EMF System

The EMF system at Pacific Northwest National Laboratory (PNNL) has been operational since 2001. The system typically operates at 6,500 volts (V), and current levels in excess of 225 kiloamps (kA) have been demonstrated. Figure 1 shows a typical response of the EMF system during a 15 kilojoule (kJ) discharge of the capacitor bank. The half-current of the system (measuring half the total system current) is approximately 86 kA, so a total current of 172 kA passed through the load coil within 26 microseconds (μs).
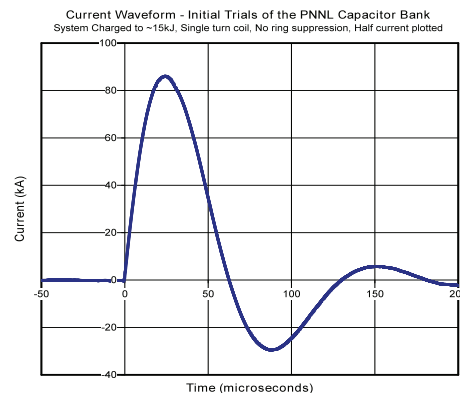
Figure 1. Typical EMF System Waveform

The system also has been cycled several thousands times at high current levels while supporting coil durability experimental work. The custom-designed control system was successfully demonstrated in automated cyclic loading operating modes. In the second half of FY 2007, a new power supply was installed and operationally validated. The supply has a significantly faster charge rate capacity that allowed faster recharging of capacitor banks so coils can be fired at higher cycle rates. This will reduce the experimental run times required to test coil designs for coil durability.

EMF Process Simulation Tool Development

The last half of FY 2008 and the initial part of FY2009 primarily were spent on further development of an EMF process simulation tool that would allow design of the process by predicting the EMF field, stresses and strains in the blank, and temperature distribution in the coil. Efforts were initiated to modify the code to run on Unix-based workstation clusters and to investigate advantages in parallelizing the code for faster run times.

EMF Process Numerical Simulation Results

The EMF process is challenging to simulate due to the need to model electromagnetic, thermal, and elastic-plastic deformation of materials simultaneously. Many of the commercial research codes have serious limitations and an inability to predict EMF process results accurately. Originally, this project focused on integrating portions of existing commercial research codes

to predict the important characteristics of a three-dimensional (3-D) EMF process accurately. However, recent work focused on more accurate custom process simulations. The current modeling work involves collaboration between PNNL, Oakland University and Ford.

During late FY 2008 and early FY2009, modelling focused on the interaction between the aluminium sheet formed at high velocity and the die into which it is being formed. The modelling of the sheet/die interaction requires development of the contact interaction, the most popular method of which is based on the geometrical analysis of the mutual position boundary nodes of each mesh. At every integration step, it verifies whether a boundary node of the blank has penetrated through the certain element of the die surface mesh. If this happens, it would be necessary to make certain corrections to bring back the node to the die surface, along which the node could slide. A significant drawback of this approach is an occasional penetration of the node through the surface, which can happen due to inaccurate calculations. As soon as the blank's node penetrates the die's surface, it is unable to return, so further calculations are useless. Therefore, a different approach was employed based on mild contact, which is popular in molecular dynamics where it is employed to model thousands of colliding atoms. The contact force is in inverse proportion to the distance between interacting surfaces. From a mathematical viewpoint, mild contact is some variable boundary of an unknown shape where the non-penetration condition and equilibrium of forces between both surfaces must be satisfied. This idea is based on the introduction of acting-in-vicinity forces repelling the surfaces to be in contact. As a result, the surfaces do not come in contact, but stay at a brief distance from each other. The force is localized in a small neighborhood of mesh elements, and it increases to infinity when the distance between them approaches zero. In other words, when the blank and die are in geometrical contact, the force between them is localized on their joint surface. Mathematically, it can be considered as continuous functions, where the absolute value of the force F is given by:

$$F = \begin{cases} k\left(\dfrac{1}{h} - \dfrac{1}{h_0}\right) & \text{at} \quad h < h_0 \\ 0 & \text{at} \quad h \geq h_0 \end{cases}$$

Here, h is the actual distance from the node of the blank to the die surface, and h_0 is the width of the layer where the force is different from zero. The direction of the force F is aligned along the local normal to the die surface. The described algorithm takes into account the Coulomb friction and other contact effects. Indeed, when the interaction of the node with an object of the other mesh is computed, the mutual positions and velocities are known. It is sufficient to find the friction directed along the tangent to the surface and opposite to the tangential part of the relative velocity vector.

Conclusions

This work has developed numerical models that describe three critical elements of the EMF process: 1) propagation of the electromagnetic field through the coil-blank system and generation of pulsed electromagnetic pressure in specified areas, 2) high-rate deformation of the blank, and 3) heat accumulation and transfer through the coil with an air-cooling system. The process models provide capability to analyze EMF restrike processes from the perspective of coil design, blank deformation, and coil cooling systems.

Presentations/Publications/Patents

1. Golovashchenko S, NM Bessonov, and RW Davies. 2008. Analysis of Blank-Die Contact Interaction in Pulsed Forming Processes. PNNL-SA-59420, Pacific Northwest National Laboratory, Richland, Washington.

2. Golovashchenko SF, NM Bessonov, and RW Davies. 2008. "Modeling of Pulsed Electromagnetic Forming." In Numisheet 2008, ed. Pavel Hora, pp. 739-742. September 1-5, 2008, Interlaken, Switzerland. The 7th International Conference and Workshop on Numerical Simulation of 3D Sheet Metal Forming Processes.

D. Pulse Pressure Forming of Lightweight Materials

Principal Investigator: Richard W. Davies
Pacific Northwest National Laboratory
PO Box 999
Richland, WA 99352
(509) 375-6474; e-mail: rich.davies@pnl.gov

Industry Consultants: Sergey Golovashchenko (Ford), John Bradley (General Motors),
Ajit Desai (Chrysler)

Technology Area Development Manager: William Joost
(202) 287-6020; email: william.joost@ee.doe.gov

Field Technical Manager: Mark T. Smith
(509) 375-4478; fax: (509) 375-4448; e-mail: mark.smith@pnl.gov

Contractor: Pacific Northwest National Laboratory
Contract Number: DE-AC05-76RL01830

Objectives

- To develop pulse pressure forming (PPF) sheet metal forming technologies (e.g., electromagnetic forming (EMF), electrohydraulic forming (EHF), and other similar technologies) to manufacture cost effective body-in-white and closure panels made from aluminum alloys, high strength and advanced high strength steels (HSS and AHSS, respectively), and magnesium alloys.

- To overcome three technical barriers to using PPF processing for more cost-effective lightweight vehicles:

  1. lack of understanding of the formability and strain rates that develop during PPF processing,

  2. lack of validated constitutive relations for lightweight materials during PPF processing,

  3. lack of validation of finite element simulation of PPF processing.

Approach, including industrial partner/collaborator and path to technology transfer and commercialization

- Design, fabricate, and demonstrate the operation of a PPF system including the use of high-speed cameras for real-time image capturing during sheet deformation.

- Characterize the strain rate, strain rate heterogeneity, formability, and fracture of 5182-O aluminum, dual phase (DP) 600 steel, and AZ-31 magnesium sheet metals during PPF and quantify the extended ductility of these lightweight metals under proportional, non-proportional, and variable strain rate loading.

- Determine the uniaxial and biaxial constitutive relations of these selected metals at PPF strain rates and investigate the microstructure, texture, and mechanical property evolution during PPF.

- Conduct numerical simulations of forming and die interaction during PPF and predict the strain, strain rate, and overall deformation of selected sheet metals subjected to PPF.

Milestones, Metrics and Accomplishments

- Milestone 1 – Complete procurement of Correlated Solutions high speed camera system and software. (Milestone No. 41812 Complete). Acquired high speed video camera equipment to capture sequential images of sheet deformation during the PPF event. The images were post-processed via digital imaging correlation software to determine the strain and strain rates during the PPF event.

- Completed PPF equipment development and demonstrated its successful operation for sheet deformation under free-forming boundary conditions and for sheet deformation in a conical die.

- Initiated forming characterization of 5182-O aluminum and DP600 steel sheet specimens and characterized real-time strain rates during PPF using the high-speed camera and image analysis system.

- Investigated the microstructure and texture evolution of 5182-O aluminum and DP600 steel sheet specimens.

- Developed an ABAQUS-based model for pulse pressure forming of sheet materials.

Future Direction

- Configure test equipment to enhance the achievable strain rate, and continue the forming characterization of 5182-O aluminum and DP600 steel to determine their forming limits at these high-strain rates.

- Complete comparisons of the texture evolution for both 5182-O and DP600 following quasi-static and high-rate deformation.

- Initiate forming characterization of AZ-31 magnesium alloy.

- Initiate high-rate uniaxial tensile testing and determine constitutive relations for 5182-O and DP600.

Introduction

The ultimate goal of the project is to extend the formability of high-strength, lightweight metals (e.g. aluminum and magnesium) and advanced high-strength steels (AHSS) using pulse pressure forming (PPF) techniques. The deliverables for the project will be the quantification of the effects of high-rate deformation on the formability and post-formed properties of several high-strength, lightweighting metal sheet materials and facilitating the extended forming of complex, lightweight automotive sheet components.

Pulse pressure forming is emerging as an attractive alternative to both conventional stamping processes and more advanced forming methods such as superplastic forming and electromagnetic forming (EMF). Since PPF relies on a high-energy discharge to generate a rapid, high-pressure pulse for high-rate deformation, it is not limited by the inherent conductivity of the sheet material. PPF can therefore be used to form "low" conductivity materials such as aluminum, AHSS, magnesium, titanium and stainless steel.

As with EMF, PPF offers the potential to develop extended ductility, allows the use of less expensive single-sided tooling, and results in little or no springback after forming. Although there are a number of established methods for generating the forming pressure pulse, little is understood about how PPF interacts with the deforming material and what the practical forming limits are for metal alloys such as aluminum, AHSS, and magnesium.

This project will conduct a series of PPF experiments to determine basic PPF operational requirements and capabilities and to generate material formability/property relationships for selected sheet materials. PPF will be demonstrated on materials having significantly lower electrical conductivity than aluminum (which can be electromagnetically formed). It is expected that the results from the project will lead to an enhanced understanding of PPF processes and its impact on metal formability, design properties and forming limits as well as material property data on post-PPF materials.

Formability and Fracture of Metals during PPF

In fiscal year 2009, PPF experiments focused on electrohydraulic forming (EHF) of 5182-O aluminum (1 mm and 2 mm thick) and of DP600 steel (1 mm thick) under free-forming boundary conditions and forming in a conical die. The details of the EHF equipment are reported in the FY2008 report [1] and only briefly described here.

The EHF test fixture (Figure 1) consisted of a test sheet that was clamped to a 150 mm diameter hemispherical chamber filled with water and subjected to a pressure-pulse from one side. The pressure pulse was generated by an underwater, high-energy electrical discharge between a pair of copper electrodes in the water-filled chamber. A pair of high speed cameras was used to capture the sheet deformation at ~67,500 frames per second and digital image correlation software was used to quantify the sheet displacement, velocity, strain-rate, and strain as a function of time.
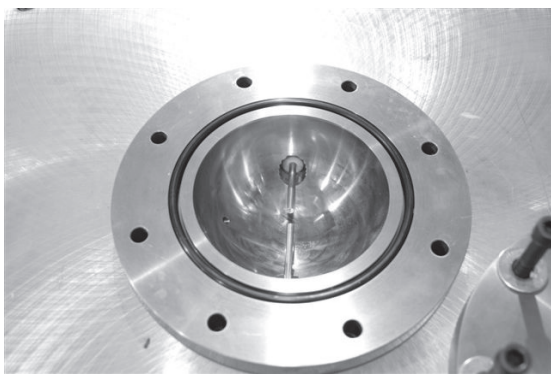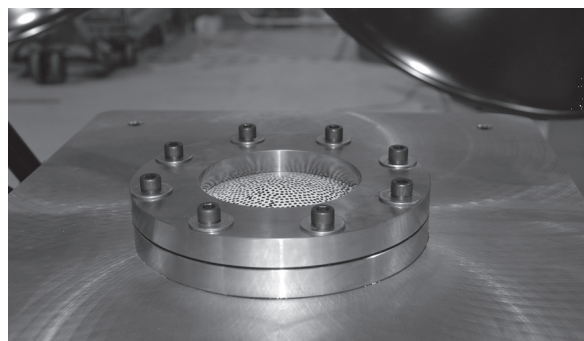
(a)   (b)

Figure 1. Images of the EHF test fixture showing (a) the electrodes in the chamber and (b) a clamped test sheet in the free-forming condition.

Preliminary EHF results showed that discharge through a solid, copper wire joining the electrodes generated greater deformation in the sheets as compared to discharge through water for the same charging voltage. Irrespective of discharge method, the sheet samples were formed into a dome shape and the majority of the data described corresponds to camera-derived measurements at the apex of the dome.

Single-pulse Experiments

Single-pulse EHF experiments (i.e. subjecting the sheet to only one pressure pulse) were conducted in the wired configuration with a charging voltage ranging from 5000 to 9500 volts depending on the sheet material and thickness. The tests were conducted in both free-forming

and conical-die forming conditions. Figure 2 compares the strain rate and the displacement at the dome apex for 1 mm thick 5182-O (Fig. 2a) and 1 mm thick DP600 (Fig. 2b) at 7500 volts and 9500 volts, respectively, under both free forming and conical-die forming conditions. A magnification in maximum strain-rate (~3-4 times) was observed in both materials when a conical die was used.
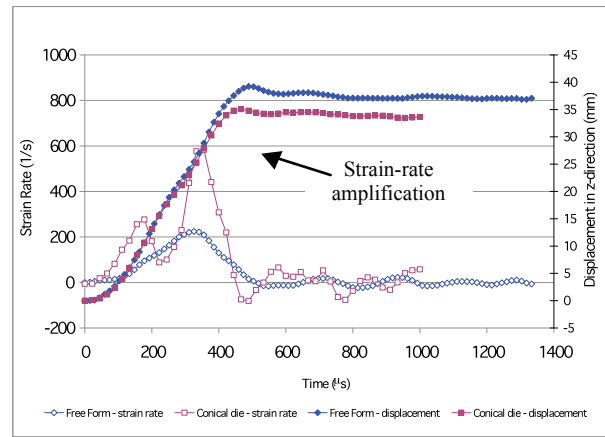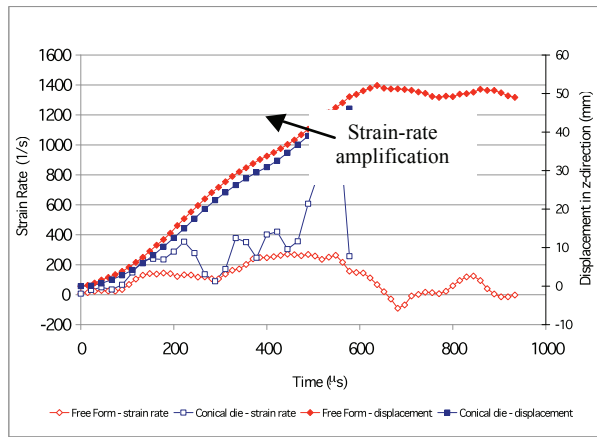
(a)   (b)

Figure 2. A comparison of the strain rate in the x-direction and displacement (z-direction) at the dome apex for the sheet metal (a) 5182-O and (b) DP600 under free forming and conical-die forming conditions.

Multi-pulse Experiments

Multi-pulse EHF experiments (i.e. subjecting the sheet to more than one pressure pulse) were performed to explore the extended ductility that this multi-step high rate forming process may offer. This step-wise forming process simulates what may be performed in production. Multi-pulse EHF experiments were conducted on 1 mm thick 5182-O and 1 mm thick DP600 at charging voltages of 6500 volts and 8500 volts, respectively. These experiments were conducted in the non-wired configuration. Figure 3 compares the strain rate and the displacement at the dome apex for 5182-O under both single and multi-pulse conditions in free forming (Fig. 3a) and conical-die forming (Fig. 3b). As observed in the single-pulse experiments, a magnification in strain rate was also observed in the multi-pulse experiments when a conical die was used.
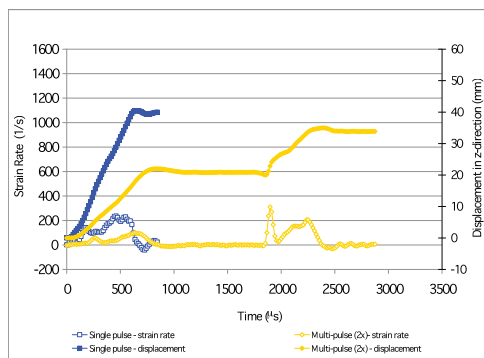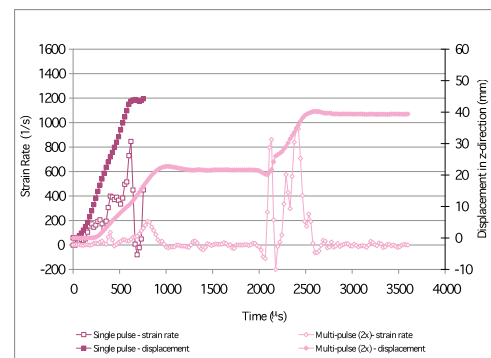
(a)   (b)

Figure 3. Comparison of the strain rate in the x-direction and displacement (z-direction) at the dome apex for single pulse and multi-pulse under (a) free forming and (b) conical die forming for 5182-O sheet metal.

Process Diagnostics

Figure 4 shows the voltage-time curves of the discharge voltage, as a function of charging voltage, recorded at the positive electrode of the EHF fixture. Figure 4(a) shows that the discharge voltage profiles for wired and non-wired configurations are quite different, indicative of the discharge initiation through the solid copper wire or water, respectively. Figure 4 shows that the (wired) discharge is accompanied by a large voltage spike whose magnitude increases with increasing charge voltage. Following the spike that lasts ~10 μs (microseconds) in duration, the voltage swings in the opposite direction and gradually decays to 0 at ~500 μs from start. The velocity-time data from the high-speed cameras indicate that the sheet deformation ends by ~600-700 μs.

(a)   (b)
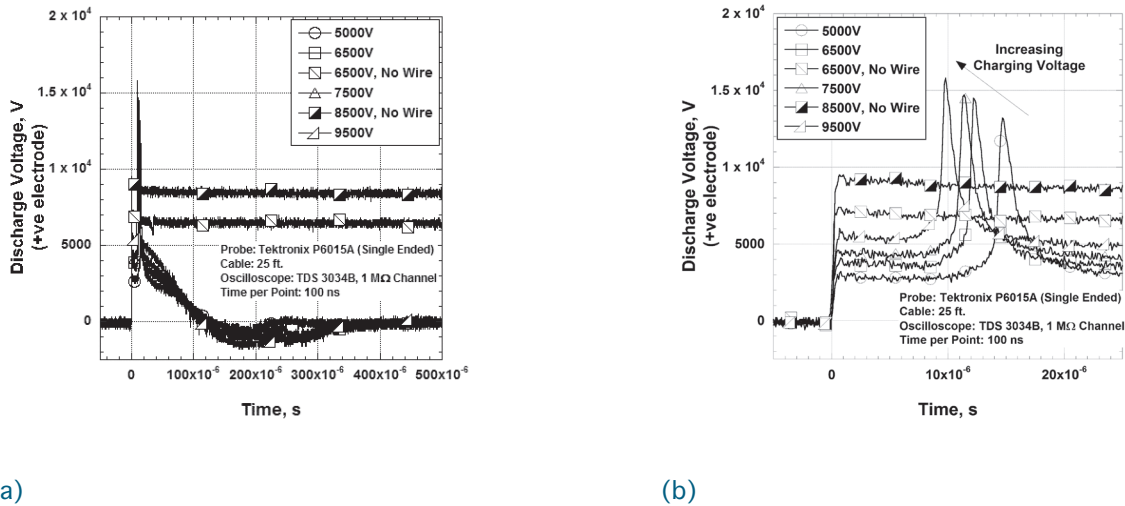
Figure 4. Voltage-time plots for discharges at various capacitor bank voltages in the wired and non-wired configurations. Image (a) shows the initial voltage rise and fall at the start of discharge, and image (b) is a close-up of image (a).

Future experiments are planned to correlate the various features of the voltage-time curve with the discharge phenomenon and the velocity profile of the deforming sheet. This information could assist in developing a realistic pressure-time profile for given test conditions, thus, enabling improved modeling of the EHF process.

Microstructure and Texture Evolution

The microstructure of aluminum and steel sheets were analyzed via optical microscopy and electron backscatter diffraction (EBSD) techniques. Test samples, ~2 mm x ~2 mm, were machined from the apex of the EHF-formed domes and from the sheet-edge, indicative of "deformed" and "undeformed" microstructures, respectively.

Figure 5 shows the pole figures of undeformed and deformed regions of aluminum and steel sheets. The sheets were deformed under free-forming conditions and a "wired" configuration. While the undeformed aluminum sheet does not show a strong texture (i.e. high intensity of poles along principal sheet directions), the undeformed steel sheet shows a strong (111) texture in the sheet-normal direction. Following electrohydraulic forming, the texture evolves in both the materials and only the principal observations from the dome-apex (i.e. bi-axially deformed region) are shown in Figigure 5. The dome apex of aluminum shows a (011) texture in the sheet-normal (ND) direction while the steel sheet shows somewhat weakening of the (111) texture (as indicated by the relative scales of the contours).

Further texture analysis of the sheets is underway that includes comparison with the texture when the sheets are deformed quasi-statically to the same strain as under high-strain rate

conditions of EHF tests. Such a comparison of sheet texture of quasi-statically deformed vs. electrohydraulically formed sheets is expected to identify the role of the microstructure in the hypothesized ductility enhancements at high-strain rates.

(a)   (b)
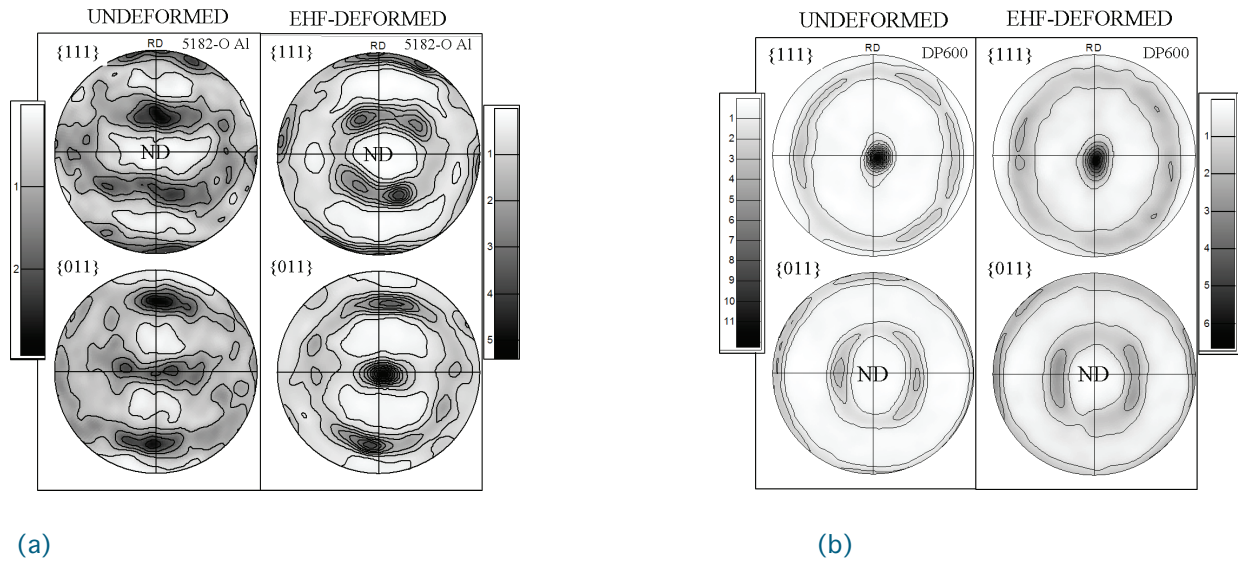
Figure 5. Selected pole figures of undeformed and EHF formed (a) Al sheet-6500V and (b) DP600 sheet (ferrite phase)-9500V. The rolling (RD) and the sheet normal directions (ND) are along the vertical axis and pole figure center, respectively, in both the sheets.

Numerical Simulation of Sheet Forming

An ABAQUS-based finite element model for EHF free-forming and conical die forming was developed. The metal sheet was modeled using axi-symmetric two-dimensional elements. A mesh size convergence study was performed, and one millimeter elements were selected for the simulations. The mechanical properties of the materials (5182-O and DP600) are given as an input to ABAQUS. A power law was adopted in our analysis, and the stress-strain relation was expressed as

$$\sigma = A + B\varepsilon^{n}$$

where A, B, and n are parameters identified for each material based on experimental uniaxial tension tests at high strain rates as described in Table 1.

Table 1. Summary of the power law parameters used for 5182-O aluminum and DP600 steel [2, 3].

	A	B	n -
5182 Al	90	455	0.32 -
DP600	450	850	0.30 -

Figure 6 is a representation of the model for both with and without a conical die and the pressure is applied to the bottom of the metal sheet. Initially, a pressure profile from literature [4] was used. The pressure function was assumed to reach the maximum at the beginning of the process (after 25 µs), then decreases continually until the end. However, this pressure profile did not yield results similar to the experiments. Consequently, a non-uniform distribution of the pressure was adopted in this work where pressure, P, is expressed as a function of time, t, and the position, x, along the sheet as follows:

$$P(x, t) = P(t)(1 - \frac{x}{2L}) \qquad 0 \le x \le L$$

The pressure profile as a function of time was based on the experimental data from the vertical displacement/velocity at the dome apex obtained from the high speed camera system.

Results of the simulations for 5182-O aluminum (1 mm thick) using the pressure profile in Equation (2) are plotted in Figures 7 and 8. Figures 7 and 8 compare the simulation and experimental results of strain rate and velocity, respectively, at the dome apex in each formed sheet. The simulations were able to reproduce the two waves present in the experiments in both the free forming and conical-die forming conditions (Figure 8). The amplitude of the velocity predicted by the simulations is also similar to the one measured experimentally.
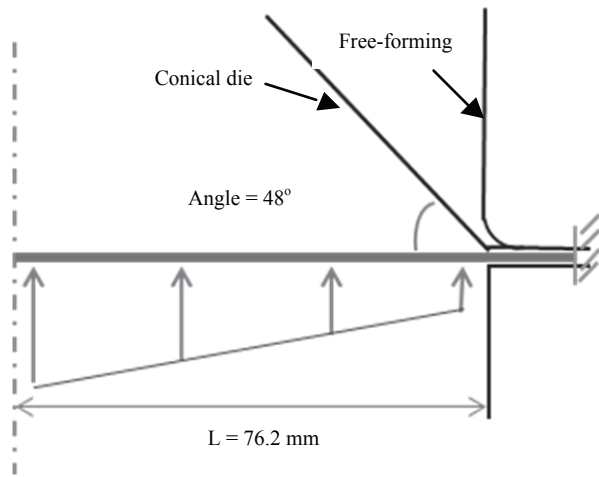
Figure 6. Representation of the model for both with and without a conical die.
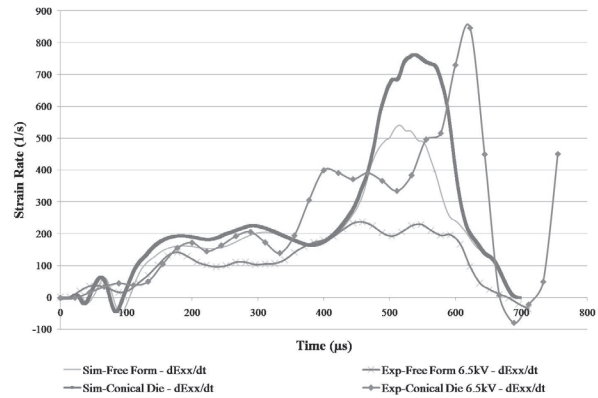
Figure 7. Simulation and experimental results of strain rate versus time for EHF formed 5182-O aluminum under free forming and conical-die forming.
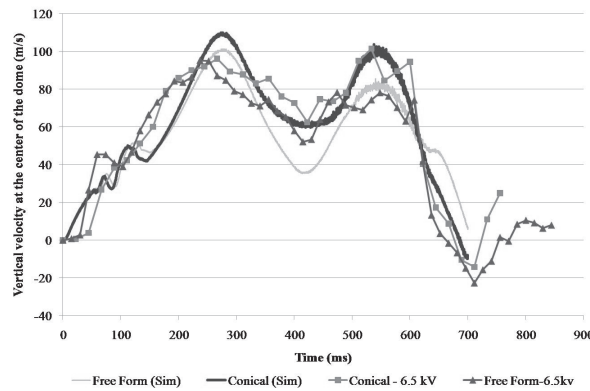
Figure 8. Simulation and experimental results of the velocity at the dome apex for EHF formed 5182-O under free forming and conical-die forming.

Conclusions

- Based on the FY2009 results, the following conclusions were drawn:

- The maximum strain-rate during EHF was magnified ~3-4 times, relative to free-forming boundary condition, by the use of a conical die.

- Extended ductility was not observed in 5182-O Al, deformed to failure by the EHF technique, with a maximum strain-rate of ~1000 /s. The pressures generated in the experiments to date were insufficient to fracture the 1 mm thick DP600 steel. Additional experiments are underway to further enhance the maximum achievable pressure and strain-rates to ascertain the existence or absence of extended ductility during high-strain-rate deformation.

- Texture changes, relative to their respective undeformed state, were observed in 5182-O aluminum and DP600 steel that were formed into domes by the EHF technique. Further experiments will be performed to identify strain-rate effects on the texture evolution.

- Literature expression for the pressure profile for an EHF process was found to be inadequate to describe the experimentally obtained velocity and strain-rate data. A new pressure profile (Equation 2) is proposed that, together with a power-law type plastic deformation behavior (Equation 1), was found to predict velocity-time and strain-rate-time profiles that matched the experimental results.

Presentations/Publications/Patents

"Pulse Pressure Forming of Lightweight Metals Project Review" presented to industry participants, Southfield, MI, August 2009.

DOE Hydrogen Program and Vehicle Technologies Program Annual Merit Review, May 2009.

"Pulse Pressure Forming of Lightweight Metals Project Review" presented to industry participants, Southfield, MI, April 2009.

DOE Materials Technologies Project Review, January 2009.

"Strain Rates and Formability under Pulse Pressure Metal Forming" presented at Plasticity 2009, St Thomas, U.S. Virgin Islands, January 2009.

References

1. Davies, R.W., et. al. 2009. "Pulse Pressure Forming of Lightweight Materials" in DOE OVT Lightweighting Materials 2008 Annual Progress Report.

2. Smerd, R., S. Winkler, C. Salisbury, M. Worswick, D. Lloyd and M. Finn. 2005. Int. J. Impact Eng. 32:541–560.

3. Curtze, S., V.-T. Kuokkala, M. Hokka, and P. Peura. 2009. Materials Science & Engineering A 507(1-2)124-131.

4. Golovaschenko, S.F., and V.S. Mamutov. 2005. 6th Symposium on Global Innovations in Materials Processing and Manufacturing held at the 2005 TMS Annual Meeting, Feb 13-17, San Francisco, CA.

E. Formability of Continuous Cast Magnesium Sheet

Principal Investigator: Aashish Rohatgi
Pacific Northwest National Laboratory (PNNL)
902 Battelle Boulevard, P.O. Box 999, Richland, WA 99352
(509) 372-6047; fax: (509) 375-4448; e-mail: aashish.rohatgi@pnl.gov

Industry Consultants:
Paul Krajewski, General Motors Corporation
(586) 986-8696; fax: (586) 986-9204; e-mail: paul.e.krajewski@gm.com

Peter Friedman, Ford Motor Company
(313) 248-3362; fax: (313) 390-0514; e-mail: pfriedma@ford.com

Jugraj Singh, Chrysler Corporation LLC
(248) 512-0029; fax: (248) 576-7490; e-mail: js329@chrysler.com

Technology Area Development Manager: Joseph A. Carpenter
(202) 586-1022; fax: (202) 586-1600; e-mail: joseph.carpenter@ee.doe.gov

Field Technical Monitor: Mark T. Smith
(509) 375-4478; fax: (509) 375-4448; e-mail: mark.smith@pnl.gov

Contractor: Pacific Northwest National Laboratory
Contract No.: DE-AC05-76RL01830

Objectives

- To evaluate the effects of lubricants on friction and formability of continuous-cast (CC) magnesium (Mg) alloy AZ31B sheets under warm forming conditions.

- To characterize the post-formed properties of CC AZ31B sheets provided by the United States Automotive Materials Partnership (USAMP) Warm Forming team (Automotive Materials Division [AMD] 602).

- To determine the forming limits of CC AZ31B sheets under bi-axial conditions (limited dome height [LDH] test) at warm forming temperatures.

Approach, including industrial partner/collaborator and path to technology transfer and commercialization

- A test-plan was developed in discussions with the following members of the Warm Forming team (AMD 602): Paul Krajewski (General Motors), Peter Friedman (Ford), Jugraj Singh (Chrysler), Sean Agnew (University of Virginia), and Kevin Boyle (Canada Center for Mineral & Energy Technology–Materials Technology Laboratory [CANMET-MTL]).

- Surface roughness of continuous-cast AZ31B sheets, provided by the AMD 602 team, was characterized using mechanical profilometry.

- A market survey of forming lubricants was conducted. Four lubricants were down-selected and evaluated by thermal analysis and elevated temperature friction tests (lubricant-coated AZ31B sheets).

- Post-formed mechanical properties of the Mg AZ31B pans (provided by the AMD 602 team), formed between 150°C–350°C at various binder pressures and using boron nitride lubricant, were determined.

- A capability to conduct elevated temperature bi-axial forming tests was developed.

- Research results were communicated to the Warm Forming team through periodic review meetings.

Milestones, Metrics and Accomplishments

- At the start of the project, a key challenge faced by the AMD 602 team was to find lubricant(s) suitable for warm forming of Mg at 350°C. Consequently, thermal response of lubricants (selected following a market survey) and the coefficient of friction (COF) for various Mg sheet-lubricant combinations were determined. Tungsten disulfide (WS2) powder lubricant was identified as a potential low-cost alternative to the currently used boron nitride (BN) lubricant.

- Sheet surface roughness and resulting friction conditions between the sheet and the die during pan-forming are believed to be a possible cause for the vendor-to-vendor variations in the AZ31B sheet formability. Consequently, surface roughness of Mg sheets from five vendors, identified as A, M, N, O, and X, was quantified. The results show a positive correlation between "high" roughness and "good" formability in all but one (vendor M) sheets. Negative correlation (i.e., high roughness and poor formability) in M sheets suggests an additional role played by the initial microstructure in determining formability.

- A bending under tension (BUT) technique to obtain the COF of Mg sheet-lubricant combinations at elevated temperature was developed. No trend was apparent between the COF and sheet roughness under the test conditions of this research. This lack of dependence of COF on sheet roughness was attributed to the dominating role of the residue that was formed upon thermal decomposition of the lubricant as the sample was heated to the test temperature.

- With the possibility of warm-forming Mg parts over a range of temperatures, it was not clear what forming temperature(s) resulted in the best post-formed mechanical properties. Consequently, post-formed mechanical properties of magnesium pans (vendor A) were determined and forming at ~175 °C–200 °C was identified as the temperature range that resulted in maximum post-formed room temperature quasi-static tensile strength in both rolling and transverse directions.

Future Direction

- The microstructure of Mg pans will be characterized via optical metallography and electron backscatter diffraction (EBSD) to obtain microstructure-formability–mechanical property correlation.

- Elevated temperature bi-axial formability tests will be conducted on selected sheet-lubricant combinations using the recently upgraded bi-axial forming equipment.

Introduction

The automotive industry is continually working toward reducing vehicle emissions and fuel consumption. A substantial portion of these efforts is focused on reducing overall vehicle weight. Magnesium (Mg) technology gives automotive producers the ability to apply this low-density

structural material selectively to automobiles to reduce cost, weight, and fuel consumption. Mg sheet has potential application in body-in-white (BIW), body closures, interior frames/brackets, and tubular components. A major barrier to using Mg sheet is the cost of conventional wrought processing due to the hexagonal crystal structure and poor hot-short characteristics. Continuous casting of Mg using twin-roll casting techniques offers the potential to reduce the cost of Mg alloy sheet.

The work scope for this agreement was developed in conjunction with the United States Automotive Materials Partnership (USAMP) Warm Forming team (Automotive Materials Division (AMD 602) and is directed at developing a fundamental understanding of the microstructure/ formability relationship and post-formed properties of continuous cast (CC) sheet materials currently being considered for use by the domestic original equipment manufacturers (OEMs). The work focuses on a collaborative contribution to AMD 602 and is intended to work in conjunction with other program participants at the University of Virginia and Canada Center for Mineral & Energy Technology–Materials Technology Laboratory (CANMET-MTL).

Activities at Pacific Northwest National Laboratory (PNNL) commenced in the latter part of 2008 and focused on establishing test matrices for lubricant evaluation and post-formed property testing. This included teleconference calls with the USAMP Warm Forming team to finalize the scope of work, schedules, and to define material sets of interest for evaluation and characterization. Heated limited dome height (LDH) tooling was set up on an Interlaken, Inc., formability machine the data from which will complement the efforts by CANMET-MTL for forming limit diagram (FLD) development.

Fiscal year 2009 (FY 2009) was the first full year for PNNL-led activities of this project. Test materials in the form of Mg sheets and warm-formed Mg pans were received from the Warm Forming team, while lubricants were obtained from commercial vendors. The experiments, results, and a discussion of FY 2009 work are described as follows:

Experimental Procedures

As-received Sheets: Mg alloy AZ31B sheets, supplied by five undisclosed vendors—identified by letters A, M, N, O, and X—were received from the AMD 602 Warm Forming team. Each sheet measured ~600 mm long (rolling direction) by ~480 mm (transverse direction) by 1 mm thick. Commercially available AZ31 sheet (1 mm thick) from Magnesium Elektron North America was also analyzed for comparison purposes (EO: annealed; EH: H24 temper).

Surface Roughness Measurements: The average surface roughness parameters of as-received sheets (both sides) were determined in the 0 degree (rolling direction), ±45 degree, and 90 degree (transverse) orientations using a SJ-201 Mitutoyo stylus profilometer and following American National Standards Institute (ANSI) standards.

Lubricant Selection: Following a market survey and down-selection (in discussions with the AMD 602 team), the following lubricants were evaluated in the present work: Deltaforge DF1105 and Deltaforge F60A (Acheson Colloids Co.), EG135 (Pyrotek, Inc.), and tungsten disulfide (WS2 powder, 0.5 μm) (MK Impex, Canada). A boron nitride-based lubricant (Forge Ease 06 ALWF from Fuchs), used by the AMD 602 team for forming Mg pans, was also evaluated to provide a baseline.
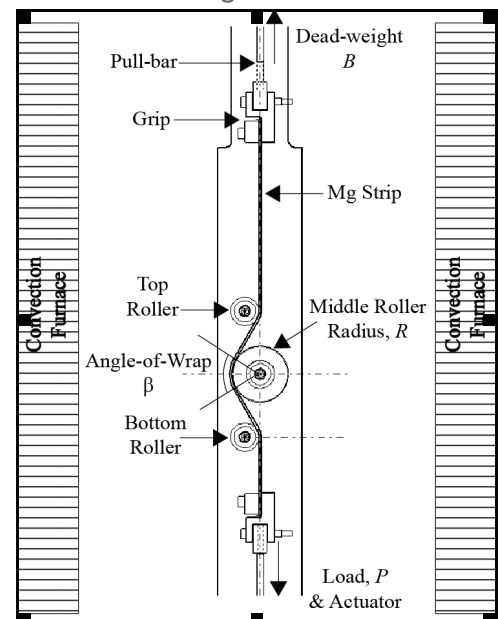
Figure 1. A Schematic of the Fixture for BUT Friction Tests of Metal Sheet Samples at Elevated Temperatures (adapted from [1])

Lubricant Analysis: The liquid lubricants (all except WS2) were evaluated by simultaneous thermo-gravimetric analysis (TGA) and differential scanning calorimetry (DSC) in a Netzsch STA 409 C/CD instrument. The ease of lubricant removal (from Mg sheet) was determined by visual examination of pre-lubricated test coupons that were subjected to elevated temperature exposure and subsequently cleaned using various washing routines.

Coefficient of Friction Determination: The elevated temperature coefficient of friction (COF) for as-received Mg sheets and lubricant combinations were determined using a modified bending under tension (BUT) fixture (Figure 1) [1]. The tests were conducted at 350°C within a furnace and consisted of pulling a strip of the test material, with lubricant applied on its surfaces, through a sequence of three rollers and recording the drawing force as a function of displacement [1, 2]. The COF is given by [3]

$$COF = \left(\frac{1}{\beta}\right)\left[\frac{(R+0.5t)}{R}\right]\ln\left[\frac{(P_{fix}-P_{bend})}{B}\right]$$

(1)

where β is the angle of wrap of the sheet specimen (thickness, t) around the middle roller (outer radius, R), B is the dead weight, P_{bend} is the measured force when all the rollers are free to move, and P_{fix} is the measured force when the middle roller is locked and prevented from rotating.

Post-formed Property Determination: Sub-size tensile specimens, as per ASTM standard E8, were machined from the base of the Mg pans along the sheet's rolling (0 degree) and transverse (90 degree) directions. The samples were tested to failure in tension at room temperature and at a quasi-static strain rate of ~0.005/s. Strain to failure and 0.2% proof stress were determined from the resulting true stress-true strain curves.

Results

Figure 2a shows that the arithmetic mean deviation of profile (R_a) for the as-received sheets ranged from ~0.2–2 μm with sheet N being the "smoothest" for all orientations and X being the "roughest" for all (except in transverse direction) orientations. Figure 2b shows the maximum two-point height of profile (R_y) for the as-received sheets ranged from ~2–15 μm with sheets N and O typically having the lowest values for all orientations. Figure 2 also shows that for a given sheet and orientation there was no significant difference between the R_a (or R_y) values of its two sides.

Figure 3 shows images of Mg test coupons that were lubricated and subjected to a heat-treatment followed by a washing routine. Upon heat-treatment, the residues of lubricants

(a)   (b)
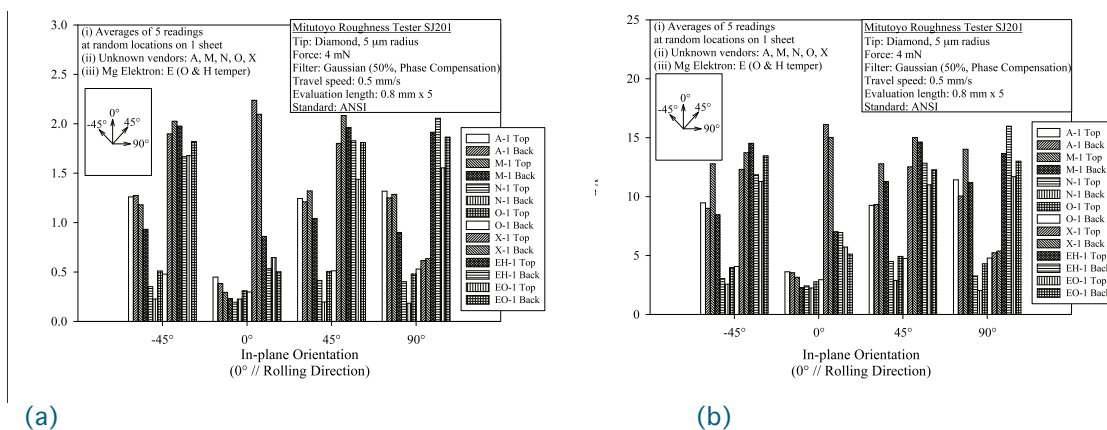
Figure 2. (a) Arithmetic Mean Deviation of Profile (R_a) and (b) Maximum Two-point Height of Profile (R_y) as a Function of In-plane Orientation for As-received Mg Sheets

Figure 3. Images of 25.4-mm-wide Mg (sheet EO) Test Coupons (with and without lubricant) Subjected to 350°C for 30 Minutes in Air and Followed by Various Washing Routines

Figure 4. TGA and DSC Curves for the Lubricants Evaluated

Figure 5. Load-displacement Curve for BUT Friction Tests for Sheet A (with and without lubricants) at 350°C in Air

DF1105, EG135, and F60A were present as a dark-brown film, dark-gray layer, and a flaky-white layer, respectively. Of the three washing routines listed in Figure 3, simple washing in warm soapy water appeared to remove the lubricant residues.

Figure 4 shows the simultaneous DSC and TGA curves for the lubricants heated at 10°C/min. in flowing air. The TGA curves for all the lubricants show a continuous weight decrease at roughly similar rates with increasing temperature and no further weight decrease occurs for heating beyond ~125°C–150°C. The residual weight at the end of the run was in the range ~20%–40%. The DSC curves for all the lubricants show evidence of endothermic reaction(s) in the temperature range ~90°C–160°C and no apparent additional reactions upon further heating to 400°C.

Figure 5 shows typical load-displacement curves for test strips that were tested along the rolling direction with and without lubricant. The curves show an initial load increase leading to a load plateau (P_{bend}) whose magnitude is indicative of the load to bend and unbend the test strip through the rollers. Subsequently, the load rapidly increases to a peak value on account of the middle roller being locked (see Figure 1). The post-peak load (P_{fix}) is indicative of the friction conditions between the test strip and the rollers. Hence, the variation of P_{fix} with displacement depends upon the specific lubrication conditions. Figure 6 shows an edge view of the tested strips, and Figure 7 shows that the average COF for the lubricants can be arranged in an ascending order as follows:

$$WS_2 < BN < EG135 < F60A < \tag{2}$$

$$DF1105 < No\ lubricant$$

This sequence is true for all the sheets except for N and X sheets where the order of F60A and DF1105 lubricants is reversed.

Figure 8 shows typical true stress-true strain tensile curves for test samples that were obtained by machining along the rolling and transverse directions (i.e., 0 degrees and 90 degrees, respectively) from the base of a Mg pan. The tensile failure in the test samples occurred with minimal necking, with ductility being generally the same (~20%) for both specimen orientations. Figure 9 shows that the 0.2% proof stress plots for vendor A pans exhibit an alternating increasing-decreasing-increasing trend with an increase in pan-forming temperature. Figure 10 shows a wide variation in the 0.2% proof stress of pans from different sheet vendors with successful forming being achieved in only A and X sheets. The strength in the rolling direction was always lower than that in the

Figure 6. Edge-view of Sheet A Test Samples Tested in a BUT Friction Test (with and without lubricants) at 350°C in Air
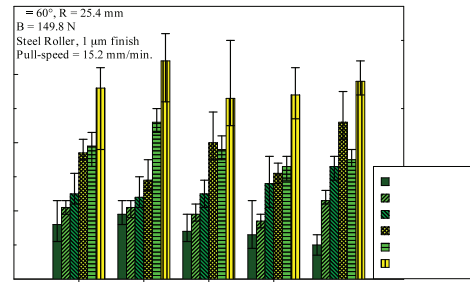
Figure 7. COF of Lubricant-coated Mg Sheets at 350°C in Air (The height of each bar is the average COF calculated from a given load-displacement curve [e.g., Figure 5] and the corresponding "scatter bar" represents the minimum and maximum COF calculated from the same curve.)
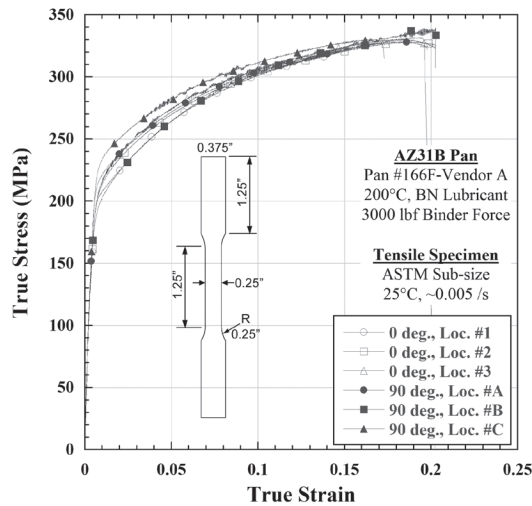
Figure 8. Stress-strain Curves of Specimens Machined from Several Locations (Loc.) in the Base of the Warm-formed Mg Pans
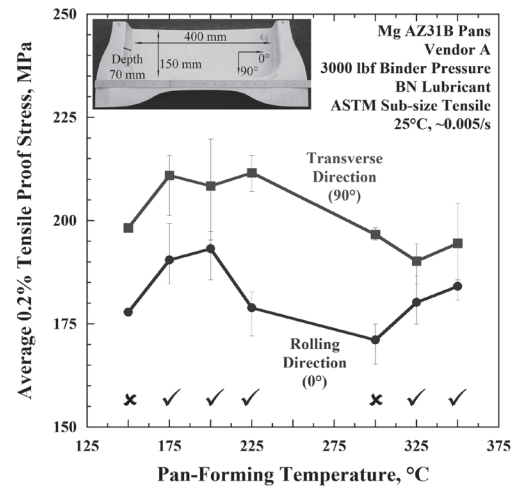
Figure 9. Post-formed 0.2% Proof Stress for Sheet A as a Function of Pan-forming Temperature (The check marks [✓] and crosses [x], respectively, indicate the success or failure in forming the pan at the corresponding temperature. The inset shows a typical pan that has been cut in half along its length [rolling direction/0 degrees].

transverse direction, except for the N sheet pan. This opposite trend (N sheet pan) in the relative magnitudes of rolling and transverse direction strength was unexpected, and the data is listed as "tentative" while additional tests are being performed for verification.

Discussion

The overall goal of this work is to understand the inter-relationship between the initial properties of continuous-cast Mg AZ31B alloy sheets and their subsequent formability and post-formed mechanical performance. From an applications standpoint, the ability to form a part (a pan, a door, etc.) from a starting sheet material is as important as obtaining the desired mechanical performance from the finished product. The issue of Mg sheet formability was addressed in this work through quantifying sheet roughness and friction conditions, while the post-formed mechanical performance of the formed sheet was quantified through quasi-static tensile tests.

Sheet formability and roughness: The AMD 602 team qualitatively ranked the sheets in the order of decreasing formability as:

$$\text{(Best) A} > \text{X} > \text{N} > \text{O} > \text{M (Worst)} \qquad (3)$$
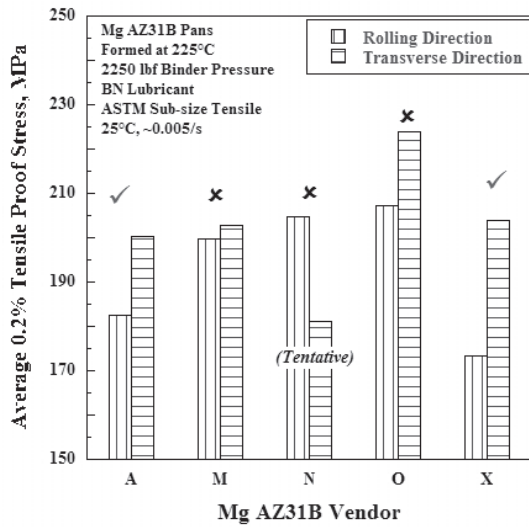
Figure 10. Post-formed 0.2% Proof Stress for Various AZ31B Sheets Formed at 225°C and 2250 lbf Binder Pressure with BN lubricant (The check marks [✓] and crosses [•], respectively, indicate the success or failure in forming the pan.)

The roughness values (R_a and R_y) of the sheets, measured along four in-plane directions (i.e., ±45 degrees, 0 degrees, and 90 degrees), were averaged. Based on these direction-averaged roughness values (R'_a and $R'y$) [2], the sheets can be ranked in descending order as follows:

$$R'_a: \text{X (1.67 } \mu m\text{)} > \text{A (1.05 } \mu m\text{)} >$$
$$\text{M (0.90 } \mu m\text{)} > \text{O (0.45 } \mu m\text{)} > \text{N (0.27 } \mu m\text{)}$$
$$(4)$$

$$R'_y: \text{X (11.91 } \mu m\text{)} > \text{M (9.49 } \mu m\text{)} >$$
$$\text{A (8.21 } \mu m\text{)} > \text{O (4.07 } \mu m\text{)} > \text{N (2.87 } \mu m\text{)}$$
$$(5)$$

The trend in vendor-to-vendor variation of sheet formability (Equation 3) and sheet roughness (Equations 4–5) suggests a positive correlation between poor formability (sheets N and O) and low value of average roughness (R'_a and R'_y) and vice-versa (i.e., good formability is correlated to high average roughness as seen in sheets A and X). It is likely that a "rougher" sheet may entrap larger amount of lubricant and the resulting friction conditions may be conducive to greater formability. However, such subjective correlation between formability and roughness does not seem to hold for sheet M (worst formability in spite of high R'_y) and indicates the need for additional characterization (e.g., microstructure) to clarify the relationship between the sheets' initial properties and formability.

Lubricant Selection: In response to the AMD 602 team's need for an alternative to boron nitride (BN) or graphite-based lubricants, tungsten disulfide (WS_2) powder (COF ~0.1–0.2 for the Mg sheets evaluated in this project) is suggested as a potential alternative on account of its COF values that are similar to or lower than the COF of currently used BN/graphite-based lubricants. Liquid lubricants (i.e., liquid at room temperature) evaluated in this work were found to decompose upon heating (see Figure 4), leaving behind a solid residue (see Figure 3). The similar COF values for a given lubricant (see Figure 7), irrespective of the Mg sheet roughness, indicates that the solid residue dominated the friction conditions rather than the sheet's inherent roughness.

Post-formed Properties: While Mg may be warm formed successfully over a range of temperatures and binder pressures, it is important to determine which forming conditions result in the best post-formed mechanical properties. Figure 9 shows that although sheet A could be formed over a range of temperature between 175°C–350°C (except 300°C), forming at 175°C–200°C resulted in maximum room-temperature, quasi-static 0.2% proof strength (tensile) in both rolling and transverse directions. The simultaneous achievement of good formability and high post-formed strength via low-temperature processing is highly desirable in the automotive industry since low-temperature processing (e.g., 175°C instead of 350°C) entails lower heating costs and enables the use of conventional oil-based lubricants. In turn, the use of oil-based lubricants (instead of BN or graphite-based lubricants for high-temperature processing) greatly simplifies post-formed processes, such as cleaning, welding, painting, etc., ultimately resulting in lower production costs.

Figure 10 shows that pans were successfully formed from sheets A and X under the given forming conditions. On the other hand, sheets M, N, and O could not be formed successfully, although they achieved similar/greater post-formed strength relative to sheets A and X. It is anticipated that microstructural analysis (planned for FY 2010) may help determine how to obtain simultaneous formability (as seen in sheets A and X) and high post-formed strength (as seen in sheets M and O).

Our expectation is that the results of this research will enhance understanding of correlations between sheet properties (microstructure, roughness, etc.), processing conditions for good formability (temperature, lubricant, COF, etc.), and post-formed properties (microstructure, mechanical performance, etc.). Such an understanding could broaden the supply base of Mg sheet-stock, leading to lower raw-material costs and eventually enabling greater use of Mg sheets in automotive applications for greater fuel economy and reduced emissions.

Conclusions

1. Owing to similar COF values as currently used BN lubricant (Figure 7), tungsten disulfide powder was identified as a potential low-cost alternative.

2. A qualitative comparison of formability and sheet roughness data (Equations 3–5) suggests "good" formability to be associated with "high" sheet roughness values. This association is seen in all the sheets except M, where an opposite trend was observed, suggesting that additional factors (e.g., sheet microstructure) need to be considered in order to understand vendor-to-vendor variations in Mg sheet formability (see Figure 10).

3. Elevated temperature BUT friction tests (Figure 1) on lubricant-coated Mg sheets demonstrated similar COF values for a given lubricant, but independent of the sheet roughness (Figure 7). This lack of dependence of COF on sheet roughness is attributed to the dominating role of the residue (Figure 3) that was formed upon thermal decomposition of the lubricant as the lubricant-coated sample was heated to the test temperature.

4. Warm forming of AZ31B sheets at ~175°C–200°C was identified as the temperature range that resulted in maximum post-formed, room-temperature, quasi-static tensile strength in both rolling and transverse directions (Figure 9).

5. Metallographic and texture analysis of Mg pans is underway to relate their formability and post-formed strength to microstructure.

Presentations/Publications/Patents

1. Rohatgi A, D Herling, and E Nyberg. 2009. "Formability of Continuous Cast Mg Sheet." October 13, 2009, Detroit, Michigan. Lightweighting Automotive Metals and Enabling Technologies Symposium (LAMETS).

2. Herling D, A Rohatgi, and E Nyberg. 2009. "Formability of Continuous Cast Mg Sheet: Forming Lubricants Selection & Post-Formed Property Characterization." January 14-15, 2009, Richland, Washington. DOE Project Review Meeting.

3. Rohatgi A, D Herling, and E Nyberg. In Press. "Characterization of Continuous-Cast AZ31B Magnesium Alloy Sheets and Lubricants for Warm-Forming Friction Effects." 2010 Annual Conference proceedings, The Minerals, Metals, and Materials Society.

References

1. Davies RW, MA Khaleel, SG Pitman, and MT Smith. 2002. "Experimental Determination of the Coefficient of Friction During Superplastic Forming of AA5083 Aluminum Alloy." Metals Park, Ohio. International Symposium on Superplasticity and Superplastic Forming, ASM International.

2. Rohatgi A, D Herling, and E Nyberg. In Press. "Characterization of Continuous-Cast AZ31B Magnesium Alloy Sheets and Lubricants for Warm-Forming–Friction Effects." 2010 Annual Conference proceedings, The Minerals, Metals, and Materials Society.

3. Fox RT, AM Maniatty, and D Lee. 1989. "Determination of Friction Coefficient for Sheet Materials under Stretch-Forming Conditions." Metallurgical and Materials Transactions A, 20(10):2179-2182.

F. Development of High-Strength Superplastic-Forming Aluminum Sheet for Automotive Applications

Principal Investigator: Curt A. Lavender
Daniel Edwards, Jung-Pyung Choi, and Elizabeth Stephens
Pacific Northwest National Laboratory (PNNL)
PO Box 999, MS K2-44
Richland, Washington 99352
(509) 372-6770; fax: email: curt.lavender@pnl.gov
(509) 375-6836; email: elizabeth.stephens@pnl.gov
(509) 376-4867; email: dan.edwards@pnl.gov
(509)276-3380; email : jung.choi@pnl.gov

Industry Consultants: Paul Krajewski, General Motors; email: paul.krajewski@gm.com
Peter Friedman, Ford Motor Company; email: pfreidma@ford.com
Ajit Desai, Chrysler; email: aj5@chrysler.com

Technology Area Development Manager: William Joost
(202) 287-6020; e-mail: william.joost@ee.doe.gov

Field Technical Manager: Mark T. Smith
(509) 375-4478; email: mark.smith@pnl.gov

Contractor: Pacific Northwest National Laboratory
Contract Number: DE-AC05-76RL01830

Objective

- The objective of this agreement is to develop a cost-effective superplastic sheet with a post-formed strength greater than that of the commonly used 5083 alloy.

Approach

- Identify candidate 5XXX, 6XXX, and 7XXX alloy systems.

- Establish operating limits for automotive pre- and post-superplastic forming (SPF) processes, such as heat-up rates and paint bake cycles, and assess alloy heat treat response.

- Collaborate with aluminum suppliers to mill-process sheet materials with SPF microstructures based on selected 5XXX, 6XXX, or 7XXX alloy compositions.

- Demonstrate SPF of high-strength sheet under simulated automotive manufacturing conditions.

Milestone, Metrics, and Accomplishments

- A survey of the literature was completed to better understand the role of low-temperature solution treatment and slow quench rate on the hardening mechanisms of 5XXX and 6XXX alloys. The results of the survey indicated that it may be possible to achieve 250 megapascal (MPa) yield strength through modification of the Mg/Si/Cu ratio in existing 5XXX and 6XXX composition alloys.

- Two basic alloy composition types were identified and cast into five book mold ingots of approximately 8 kilograms (kg) each with varying Si, Mg, and Cu content.

- Five alloy compositions in book mold form were homogenized using a single condition, forged, and rolled into 1.5 mm sheet.

- Sheet materials produced from the five compositions were characterized for tensile properties, and the alloy identified as 6-2 achieved the 250 MPa strength level using the non-ideal heat treatments required for high-volume superplastic part production.

- Superplastic tensile properties were measured on a single sheet condition for the five alloy compositions, and the results indicated additional thermomechanical process development will be required to achieve adequate ductility.

- Milestone: Complete post-forming mechanical property measurements and report results on modified 6000-series SPF sheet formed under simulated manufacturing cycle (completed September 2009)

Future Direction

- Focusing on the alloy 6-2, cast additional book mold materials and process to sheet for superplastic and room temperature tension test evaluation using alternate thermomechanical processing designed to develop adequate superplasticity.

- Produce sheet of at least 180 mm width and superplastic form using the biaxial forming die. Evaluate the post-SPF mechanical properties using a test matrix of cooling rates and simulated paint bake cycles.

- Identify industrial aluminum mill to support process scale up.

Introduction

The objective of this project is to develop a cost-effective superplastic sheet with a post-formed strength >250 MPa. Superplastic forming (SPF) of aluminum alloys has been used in forming automotive outer body panels and closures. Because SPF involves forming of the aluminum sheet at elevated temperatures, the final formed material strength is similar to that of an annealed (soft) aluminum sheet. Current automotive SPF applications have focused on the use of aluminum 5083 alloy, which, with its relatively high magnesium content, develops a post-formed strength of around 150 MPa. Using 5XXX-series aluminum alloys with Mg levels above 3 weight % introduces the potential for stress-corrosion cracking (SCC) when exposed to an elevated temperature environment. The net result of these factors is SPF 5083 alloys have largely been restricted from use in body-in-white (BIW) and under-hood applications where higher strength and resistance to SCC are required.

The current project is planned for three years and will evaluate a series of 5XXX-, 6XXX-, and 7XXX-series aluminum alloys to develop a modified alloy and mill processing methods to produce a high-strength SPF aluminum sheet with a post-formed strength >250 MPa. The technical approach will evaluate modifications to existing heat-treatable alloys, combined with thermomechanical processing methods to produce a fine-grained SPF sheet with a post-formed heat treat response. The development of a fine-grain microstructure that remains stable at SPF temperatures generally requires a combination of alloy chemistry adjustment combined with combinations of hot and cold rolling into sheet. In the aluminum alloy system, individual alloy

specifications contain significant ranges for many of the key alloying elements. As deduced from previous PNNL SPF development work, alloy modifications within the set alloy ranges can be used to optimize SPF microstructures. The focus of the project will be to develop a heat-treatable alloy that has a post-forming, age-strengthening response compatible with automotive body-in-white (BIW) thermal cycles (E-coat; paint bake). The project will result in the development of a cost-effective, high-strength SPF aluminum alloy sheet that can be used in higher strength and elevated temperature automotive applications, extending the use of SPF aluminum to BIW and underhood sheet components.

Low-Cost High-Strength Superplastic Forming Development

Automotive Superplastic Processing Constraints

1. During the previous reporting period, the process parameter constraints required for a low-cost, high-volume automotive SPF process[1], as shown by Figure 1, were identified and can be summarized by the following:

2. The sheet blank will be heated in the preheater to the forming temperature in 30 to 60 seconds, and the transfer from the furnace to die will be rapid with negligible heat loss.

3. The part must be formed in the forming press at less than 500°C (ideally closer to 450°C).

4. The part will be formed in less than 2 minutes.

5. The part will cooled at a relatively slow rate in a cooling fixture manner to minimize distortion. The cooling time from the forming temperature to 65°C will be approximately 1 minute.

6. The as-formed part must be ductile enough to be hemmed.

7. The part must respond to a paint-bake heat treatment to achieve the desired 250 MPa strength with no more than 0.4% Cu as an alloying addition.
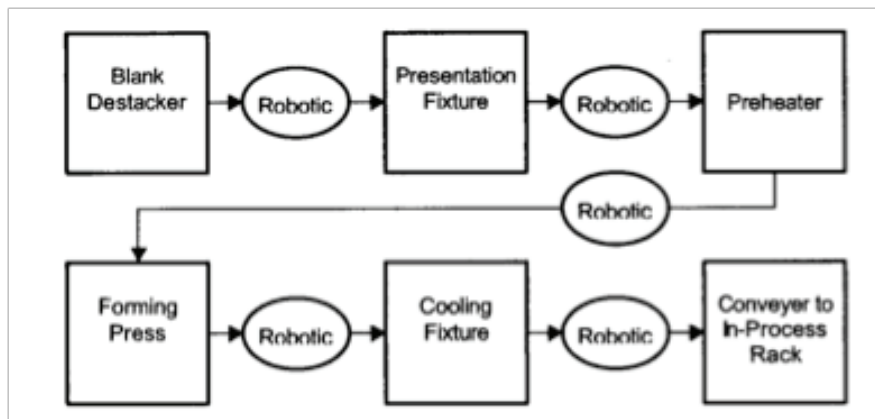
Figure 1. Advanced Automotive Superplastic Forming Process Sequence (from Schroth[1])

Given the low-cost, high-volume automotive SPF process constraints, it is necessary that the part exit the cooling fixture with a metastable solid solution containing sufficient solute to strengthen the alloy to 250 MPa during precipitation that will occur during paint bake. In addition to the challenging, less-than-ideal thermal process, the alloy must exhibit approximately 150% elongation at a strain rate of 1×10^{-3} s^{-1}. The more difficult of the two technical challenges is likely to be the development of an alloy that achieves the 250 MPa strength level using a low-temperature solution treatment, slow cooling rate, and short aging times associated with the paint bake. Therefore, the project has focused on first developing an alloy that realizes

the required 250 MPa strength, then the thermomechanical process to develop the necessary superplastic behavior. The following sections report on progress during this reporting period on the development of both strength and superplasticity.

Superplastic Alloy Development

Development of Alloy Composition and High Strength

The challenge for strength development in the SPF process is achieving a sufficient hardening response during the paint bake. Unlike ideal conventional aluminum age treatments that are 8 to 24 hours, the SPF alloy must achieve 250 MPa strength in less than 2 hours at a temperature of 180°C. Previously, PNNL demonstrated that this was possible with the 6013 alloy. However, the primary hardening phase in the 6013 alloy is the AlMgCu (theta) precipitate.(2) Given that Cu additions of greater than 0.4 weight percent produce unacceptable corrosion resistance for automotive applications, the new alloy must rely on Mg and Si additions for precipitation hardening. A survey of the literature found that alloys with no Cu that contain specific ratios of Mg/Si can achieve strengths in excess of 300 MPa in short aging times through precipitation when solution is heat treated at ideal conditions to produce the Mg_2Si precipitate.(3) Additionally, Gaber(4) showed small additions of Cu can reduce the age time by a factor of three for alloys that contain the exact ratio of Mg/Si to produce the Mg_2Si precipitate (known as a "balanced alloy"). As with the previous work, the Gaber alloys were solution heat treated at the ideal conditions. The literature suggested that it may be possible to achieve the 250 MPa strength level during the short aging time associated with the paint bake. The challenge would be to determine if an alloy that can achieve strengths in excess of 300 MPa with an ideal solution heat treatment can achieve 250 MPa with the less-than-ideal 450°C to 500°C forming process and slow cooling.

Table 1. The Nominal Chemical Compositions, in Weight Percent, for the Five Developmental Alloys

Alloy	Mg	Si	Cu	Cr	Mn
5-1	3.5	0	0.4	0.1	1.0
5-2	3.5	0.4	0.4	0.1	1.0
5-3	3.5	0.6	0.4	0.1	1.0
6-1	0.7	1.5	0.2	-	1.0
6-2	0.7	1.5	0.4	-	1.0

Superplasticity is primarily achieved by solute drag, grain boundary sliding, or a combination of both. [5]

Therefore, two additional considerations were given in alloy design: 1) superplasticity through solute drag by adding Mg and 2) minimizing the grain size by promoting nucleation of many grains by maximizing the eutectic constituent. Based on previous work(6), the most effective eutectic constituent addition is Mn. All alloys were designed to have 1.0 weight percent Mn.

From this alloy design strategy, five alloys were cast at PNNL into 75 mm-thick book molds using the casting equipment shown in Figure 2.
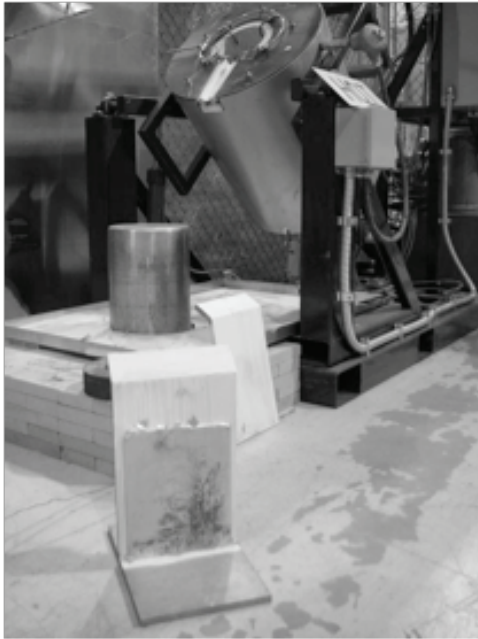
Figure 2. Tilt Pour System and Stainless Steel Book Mold Used to Produce 8 kg heats Approximately 75 mm Thick

The alloy compositions provided in Table 1 use varying ratios of Mg, Si, and Cu to develop strengthening by a combination of Mg_2Si and AlCu precipitation and solid solution strengthening from Si and Mg.

The alloys were produced in two groups and were roughly designed around common 5XXX and 6XXX alloys. Each group was designated 5 and 6, respectively. The 5 alloy series was designed to maximize superplasticity through solute drag while achieving strengthening from the Mg_2Si and AlCu precipitates and Mg in solid solution. The 6 alloy series was designed to achieve strengthening through the Mg_2Si and AlCu precipitates and Si in solid solution. Superplasticity in the 6 alloy series would be achieved entirely by fine-grained superplasticity.

For the 5 alloy series, the amount of Si was varied. Alloys designated 5-1, 5-2, and 5-3 contained 0, 0.2 and 0.4 of Si, respectively. The 6 alloy series had two levels of Cu, 0.2 and 0.4, for the alloys designated 6-1 and 6-2, respectively.

After casting, each alloy was homogenized at 510°C for 10 hours and hot forged at 510°C to 16 mm. For expedience, hardness, and tensile strength characterization of the alloys, tensile samples were removed from the 16 mm slab. Tensile testing was performed using 4 mm gage diameter round samples.

An extensive matrix of hardness testing also was performed, which is too lengthy to report here. The results can be summarized as follows:

- All hardness samples were solution-treated and air-cooled at the 16 mm thickness to provide a slow cooling rate.

- To be consistent with the expected paint bake cycle, the aging temperature was held constant at 180°C.

- For the 5-1, 5-2, and 5-3 alloys, little or no hardening was observed when solution heat treated at 400°C or 450°C. A slight hardening response was observed for solution treatment at 510°C.

- For the 6-1 and 6-2 alloys, no hardening was observed when solution heat treated at 400°C. However, significant hardening was observed for solution heat treatments above 450°C.

- In all cases for alloys that exhibited a hardening response, the maximum hardness was achieved after 8 hours of aging.

From the hardness test results, a reduced matrix of heat treatments were used on the alloys, and tensile properties were measured. As expected from the hardness test results, the 5-1,

5-2, and 5-3 alloys had strengths less than 170 MPa, even when aged to peak hardness and solution treated at 510°C. The low strengths of the 5 alloy series suggests that the mechanism for hardening, predominately using Mg_2Si precipitate, requires a much more rigorous solution heat treatment than the low-temperature slow cooling required for a low-cost, high-strength SPF process. However, the hardening response found in the 6-1 (0.2 Cu) and 6-2 (0.4 Cu) did translate into much higher tensile strengths.

For the 6-1 (0.2 Cu) and 6-2 (0.4 Cu) alloys solution treated at 510°C and peak aged, the tensile strengths were nearly identical where the yield strength and ultimate were 300 MPa and 330 MPa, respectively. When the solution temperature was reduced to 450°C in the peak age condition, the 6-1 alloy exhibited a yield strength of 210 MPa and an ultimate strength of 230 MPa, and the 6-2 alloy had yield and ultimate strengths of 240 MPa and 280 MPa, respectively.

Given the encouraging tensile results for the peak age conditions, the 6-1 and 6-2 alloys were then subjected to a simulated thermal cycle expected for a low-cost SPF process at 450°C followed by a short aging cycle simulating the expected paint bake. The 6-1 alloy exhibited tensile yield and ultimate strengths of 180 MPa and 225 MPa, respectively. The 6-2 alloy exhibited 230 MPa and 280 MPa for yield and ultimate strengths, respectively.

The tensile results for the 6-1 and 6-2 alloys suggest it is possible to achieve a 250 MPa using the less-than-ideal thermal cycle required for a low-cost automotive SPF process. The design of the alloy obviously oversimplifies the hardening mechanisms that are active. For example, it would not be expected that at 510°C solution heat treatment there was no difference in strength for the 6-1 (0.2 Cu) and 6-2 (0.4 Cu) alloy when there was a 50 MPa difference in ultimate strength at the 450°C solution heat treatment. This unexpected result, along with a nearly identical strength for the 6-2 alloy when peak aged and paint baked, would suggest that once the mechanisms are understood, further optimization likely would result in even higher strengths at a wider range of thermal conditions.

Development of Superplasticity

The five book mold cast alloys were processed to 2 mm sheet and hot tension tested using the ASTM E2448 method. Given the need for short forming times in high-volume automotive production, the tests were run at the relatively fast rates of 5×10^{-4} s-1 and 1×10^{-3} s^{-1}. At this stage of the development, a single thermomechanical process was used based on prior experience with the development of fine-grained superplasticity in the 5083 alloy. The thermomechanical

process was as follows: homogenization of the 75 mm casting at 510°C for 10 hours, hot forging at 510°C to 16 mm, cold rolling to 8 mm, annealing at 400°C, and, finally, cold rolling to 2 mm sheet. The ASTM E2448 hot tension samples, as shown in Figure 3, then were machined from the 2 mm sheet and tested at 450°C and 510°C at the two previously described rates.

The results for the 5 alloy series were promising where the alloys exhibited tensile elongations in excess of 250% at all rates and temperatures. However, given the low strengths achieved during heat treatment, the alloys are of little interest and additional thermomechanical processing and optimization of the superplasticity will not be performed.

Figure 3. ASTM E2448 Superplastic Tensile Sample Used for Superplastic Tension Characterization (The top sample is untested; the lower samples were tested to failure from the 6-2 alloy.)

The alloys 6-1 and 6-2 exhibited lower elongations, whereas samples tested at 500°C had total elongations of 150% to 175% at 1×10^{-3} s^{-1} and 225 to 250% at 5×10^{-4} s^{-1} (as shown by the stress strain curves in Figure 4). When tested at 450°C, the ductility decreased to 100% at 1×10^{-3} s^{-1} and 200% at 5×10^{-4} s^{-1}.
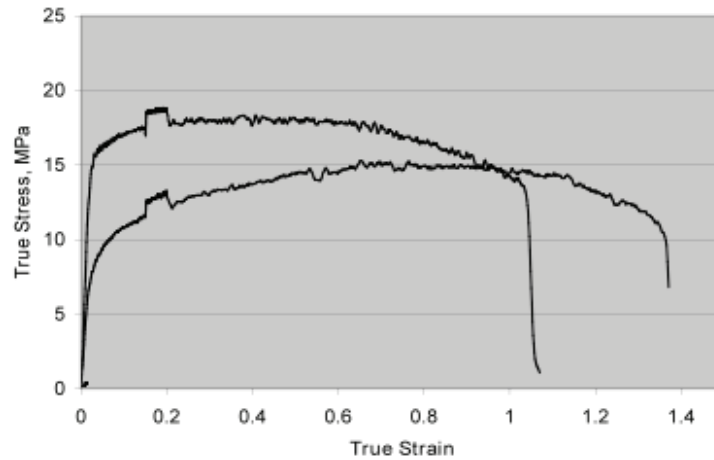
Figure 4. True Stress-True Strain Curves for Alloy 6-2 tested at 1×10^{-3} s^{-1} (top line) and 5×10^{-4} s^{-1} at 500°C

The relative low ductility observed in sheets from alloys 6-1 and 6-2 can be explained by the larger-than-desired grain size of 30 µm. The unexpected larger grain size likely is a result of the non-optimal thermomechanical process. As shown by Figures 5a, 5b, and 5c, the eutectic constituents were excessively coarsened by the homogenization treatment and not adequately redistributed during the forging process. Tests are underway now to optimize the homogenization treatment, and future reductions from the as-cast book mold to the intermediate 16 mm slab will be performed by hot rolling using the PNNL 9000 kN 14-inch diameter rolling mill.
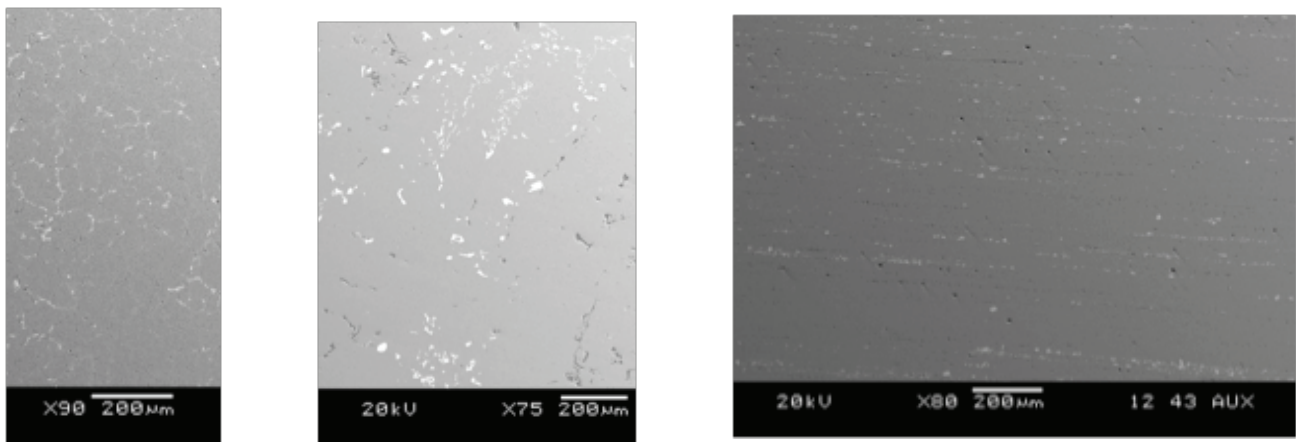
(a)   (b)   (c)

Figure 5. Scanning Electron Images of the Eutectic Constituent Phases (light color) in the 6-2 Alloy in the As-cast(a), As-forged(b) and (c) 2 mm Sheet Conditions (The micrographs show the coarsening of the phase that occurred during homogenization and the relative poor distribution after rolling to sheet.)

Conclusions

During this reporting period, the following conclusions were derived:

- An alloy strengthened by excess Si, Mg_2Si, and AlCu can meet the challenging demand for 250 MPa strength using thermal treatments consistent with those needed for a low-cast, high-volume automotive superplastic process.

- Alloys dependent upon Mg solid solution strengthening and the Mg_2Si precipitate cannot develop the strengths needed with the low-temperature slow cooling rate solution heat treatment step needed for a low-cost, high-volume automotive superplastic process.

- The alloys designed for fine-grained superplasticity combined with solute drag, 5-1, 5-2, and 5-3, exhibited the best superplastic elongation.

- The alloys 6-1 and 6-2 exhibited poor superplastic elongations likely attributed to the large grain associated with the thermomechanical process used. Additional thermomechanical processing is in development.

- The alloy down-selection milestone was met, and future development will focus on an alloy close to a 6XXX alloy composition using excess Si, the maximum allowable Cu content, and the Mg_2Si precipitate.

Presentations

- DOE Vehicle Technologies Program Annual Merit Review, February 2008.

References

1. Schroth JC. 2004. "General Motors Quick Plastic Forming Process." In Advances in Superplasticity and Superplastic Forming, eds. EM Taleff, PA Friedman, PE Krajewski, RS Mishra, and JC Schroth. TMS, Warrendale, Pennsylvania.

2. Lavender CA. 2006. "Enhanced Plasticity in AA6013 at Elevated Temperatures." July 4–6, 2006, Vancouver, British Columbia. THERMEC' 2006.

3. Gupta AK, DJ Lloyd, and SA Court. 2001. "Precipitation hardening in Al-Mg-Si alloys with and without excess Si." Materials Science and Engineering 316(1-2):11-17.

4. Gaber A, MA Gaffar, MS Mostafa, and EFA Zeid. 2007. "Precipitation kinetics of Al–1.12 Mg2Si–0.35 Si and Al–1.07 Mg2Si–0.33 Cu alloys." Journal of Alloys and Compounds 429(1-2):167-175.

5. Taleff EM. 2004. "An Overview of Creep Deformation Behaviors in 5000-Series and Al-Mg Alloys." In Advances in Superplasticity and Superplastic Forming, eds. EM Taleff, PA Friedman, PE Krajewski, RS Mishra, and JC Schroth. TMS, Warrendale, Pennsylvania.

6. Vetrano JS, CA Lavender, CH Hamilton, MT Smith, and SM Bruemmer. 1994. "Superplastic Behavior in a Commercial 5083 Aluminum Alloy." Scripta Metallurgica et Materialia 30(5):565–570.

G. Aluminum Automotive Closure Panel Corrosion Test Program

Project Co-Chair: Tracie Piscopink-Jafolla
General Motors Corporation
3300 General Motors Road
MC: 483-370-101
Milford, MI 48380-3726
(248) 676-7014; e-mail: tracie.l.jafolla@gm.com

Project Co-Chair: Francine Bovard
Alcoa Technical Center
100 Technical Drive
Alcoa Center, PA 15069
(724) 337-3249; e-mail: francine.bovard@alcoa.com

Technology Area Development Manager: William Joost
(202) 287-6020; e-mail: william.joost@ee.doe.gov

Objective

- Develop a standardized cosmetic corrosion test for finished aluminum automotive body panels that provides a good correlation with in-service testing and field performance.

Approach

- Conduct laboratory testing, outdoor exposures, test track exposures and in-service testing.

- Evaluate test data to determine which accelerated tests correlate with in-service testing.

- Conduct iterative laboratory testing to improve correlation between lab tests and on-vehicle exposures.

Accomplishments

- Test track exposures, on-vehicle exposures and outdoor exposures have been completed.

- Many laboratory tests have been conducted and compared with service-relevant exposures.

- Corrosion product analyses conducted for some laboratory tests and exposures on-vehicles.

- Key environmental parameters have been identified as important for inclusion in an accelerated test for painted aluminum.

- ASTM G85-A2 has been identified as the existing test method that most consistently provides the best correlation with in service exposures.

Future Direction

- The objective of this program has been accomplished and the program is now complete. A final paper will be submitted for publication in the proceedings for SAE 2010.

Introduction

All Original Equipment Manufacturers (OEMs) and their suppliers rely on various laboratory tests to assist in prediction of real life service performance, even though it is well recognized that many of these lab tests do not fully represent observed corrosion behavior. Part of the difficulty lies in the large number of variables in service that influence corrosion rates and how to fully take all of these factors into account with one single test procedure. OEMs have also developed elaborate test tracks or proving ground tests in attempts to more closely simulate service conditions but in general the proving ground tests also have not correlated well with on-vehicle performance for painted aluminum [1-5].

In addition to variations in the real life corrosion conditions, there are also many factors in the OEM production process that influence the aluminum surface condition, chemical treatment and paint performance of a closure panel that are difficult to fully control on lab prepared panels. Despite these difficulties, the potential for time and cost savings that could be achieved by having a general agreement on a lab test capable of closely mimicking real life performance is highly desirable. Therefore, in 2000, a group of representatives from the aluminum industry, US automotive manufacturers, coating and other suppliers formed a task group within the Automotive Corrosion and Protection Committee of the Society of Automotive Engineers (SAE) to work together on identification of a test method that provides good correlation with on-vehicle cosmetic corrosion performance. Since then, a number of papers have been presented at the SAE Congress [1-5] to provide periodic updates on the findings of this group to the automotive corrosion community. In this report, the final results of this multi-year project are summarized.

Experimental

Materials

The painted panels used in this program are listed in Table 1. The substrate materials, metal finish and paint processing variables were selected to give a range of cosmetic corrosion performance. Several aluminum alloys used in the United States and in Europe, both current and historical, were included, with two alloys processed to simulate metal finishing in an automotive assembly plant body shop. Panels made from electro zinc coated steel and uncoated cold rolled steel were included as reference materials [6].

Table 1. Materials

Panel Code	Alloy Substrate	Metal Finish	Paint System
A or 1	AA6111-T4PD	Mill	Standard
B or 2	AA6111-T4PD	Mill	Low F⁻
C or 3	AA6111-T4PD	Mill	Ecoat
D or 4	AA6111-T4PD	Sanded	Standard
E or 5	AA6016-T4	Mill	Standard
F or 6	AA6022-T43	Mill	Standard
G or 7	AA2036-T4	Sanded	Standard
H or 8	EG 60 Steel	Mill	Standard
I or 9	CR Steel	Mill	Standard

Two sizes of panels, 2" x 4" and 4" x 6", of each of the materials were painted with a typical automotive paint system. This paint system included zinc phosphate pretreatment, medium-build cathodic electrophoretic priming (E-coating), and spray painting with a primer surfacer and white basecoat/clear topcoat system for a total paint film thickness of approximately 100 μm. One set of 6111 panels (Panel Code B) was processed through the phosphate pre-treatment with lower fluoride concentration (comparable to the fluoride level used for steel only vehicles which results in lower phosphate coating weight). Also, since qualification testing is often done on panels that are processed only through the electrophoretic primer (E-coat) step, another set of 6111 panels (Panel Code C) was processed only through the E-coat step (i.e., standard fluoride for Al but no basecoat or clear coat applied). Panel code C was evaluated in lab tests only (no on-vehicle or proving ground exposures).

Panels were prepared as needed for testing with two parallel scribes penetrating through the coatings to the substrate. The panels were provided to the testing laboratories as fully prepared painted and scribed panels. Triplicate sets of the painted and scribed samples have been exposed in a variety of environments, including: laboratory, static outdoor exposure, proving ground, and on-vehicle exposure.

Evaluation Method

For this study, an optical imaging system developed by Atlas Material Testing Technology, LLC was employed to quantitatively interpret the degree of cosmetic corrosion. The imaging system employs controlled illumination conditions, high-resolution digital image capture and advanced algorithm-based image and data analysis methodologies [6].

Four geometrical attributes of the cosmetic corrosion were measured: area of corrosion, maximum length, minimum length, and average length. The area of corrosion was found to be the most representative and comprehensive measurement. Because the size of the panels and therefore the scribe lengths for the lab tests were different from the other tests the corrosion area was normalized to the length of the scribe (i.e. area per length). The normalized corrosion areas for triplicate panels (2 scribes per panel) were then averaged and the results are reported as "normalized average area".

On-Vehicles Exposures

It is critical when developing a laboratory based test that test-to-field correlation be performed. In an effort to capture real-world data in developing this test, it is preferable to expose these panels to severely corrosive environments that represent "worst case" real-world service environments. Suitable environments exist in the northeastern United States, southeastern coastal areas of the United States, and southeastern Canada. Two of these environments (northeastern United States and southeastern Canada) were part of this program. The sites selected for this study were: 1.) Detroit, Michigan, 2.) St. John's, Newfoundland, 3.) Montreal, Quebec and 4.) Cleveland, Ohio to Buffalo, New York truck route. Two sets of 2" x 4" test panels were exposed on each vehicle (two vehicles per site). Each set of 24 (three each of eight material variables) were attached to a mounting panel (16" x 12") using double-backed tape prior to mounting on the vehicle. At the Detroit, St. John's, and Montreal sites one set was mounted on the hood of each vehicle (horizontal orientation) and one set on the right front door of each vehicle (vertical orientation). For the Ohio-New York (OH/NY) truck route the panels were mounted beneath the trailer frame behind the front wheels (vertical orientation only). Each panel contains 2 diagonal scribe lines which are 2" long and 1" apart. The panels were exposed for a total of 4 years of in-service exposure. Intermediate evaluations were conducted when possible.

Laboratory Tests

Several rounds of laboratory testing were conducted through the duration of this project [1-5]. All of the accelerated laboratory tests that were evaluated are listed in Table 2. After several rounds of laboratory tests and comparison of the results with results from on-vehicle exposures, the list of lab tests of interest was narrowed to the following two tests:

1. *ASTM G85-A2 - Cyclic Acidified Salt Fog Test [8]*

Test Cycle: 6 hr repetitive cycle with 3 steps/ cycle:

1. 45 min. Spray

2. 2 hr. dry-air Purge

3. 3hr. + 15 min. Soak (RH gradually increases during soak)

• Test Solution: 5%NaCl acidified to pH = 2.8 – 3.0 with acetic acid

• Temperature: 49˚C (120˚F)

Table 2. Laboratory Tests Evaluated in this Program

	Test Procedure	Duration(s)
1	SAE J2334	40, 60 & 80 cycles
2	ASTM D2803 (80% RH)	6 weeks
3	Modified ASTM D2803 (60% RH)	6 weeks
4	Modified ASTM D2803 (100% RH)	6 weeks
5	ASTM G85-A 2	1, 2 & 3 weeks
6	VDA 621-415	10 cycles / 70 days
7	ASTM B117	500 & 1000 hours
8	CCT IV	35 & 70 cycles
9	KWT	6 weeks
10	Ford Arizona proving Ground Exposure (APGE)	35 & 70 cycles
11	Ford APGE (Automated)	35 & 70 cycles
12	HCl Dip	3, 6 & 8 weeks
13	GM9511P	4 weeks
14	GM9682P	4 weeks
15	ASTM G87	20 cycles
16	ASTM G85-A5	500 hours
17	ASTM G85-A4 (continuous spray)	500 hours
18	ASTM G85-A4 (intermittent spray)	500 hours
19	Modified ASTM G85-A4 (continuous spray)	500 hours
20	Modified ASTM G85-A2	500 hours

2. *ASTM G85-A4 - Salt/SO2 Spray Test (Intermittent) [9]*

-Test Cycle: 3 hr repetitive cycle with 3 steps/ cycle:

1. 30 min. Spray

2. 30 min. SO_2

3. 2hr. Soak

● Test Solution: 5%NaCl acidified to pH = 2.5 – 3.2

● Temperature: 35˚C (95˚F)

The ASTM (American Society for Testing and Materials) G85-A2 test cycle was developed for use with standard water jacketed salt spray cabinets. A protocol for using automated cyclic cabinets to run this cycle has been developed to allow use of alternate equipment. If the RH is properly controlled the cycle can be adequately replicated. The addition of this alternate protocol for automated equipment will be proposed as a revision to the ASTM standard.

Corrosion Product Analysis

Corrosion product analysis was performed on panels A, D, G and I removed from on-vehicles in Detroit, St. John's and Montreal. In addition, the analysis of CLIMAT wire samples [10] from various locations was also conducted to evaluate atmospheric conditions in the areas where on-vehicle exposures were conducted.

Corrosion product analyses were performed using Leo 440 scanning electron microscope (SEM) equipped with a Quartz XOne energy dispersive X-ray (EDX) analysis system. The use of SEM/EDX allows not only for a measurement of the chemical species present, but also for an analysis of the distribution of these species in and around the corroded area on the panel.

Results and Discussion

On-Vehicle Exposures

Although the extent of corrosion in the on-vehicle exposures varied considerably from vehicle-to-vehicle for the various sites, panels D, G, and I typically exhibited significantly more corrosion than the other substrates, as illustrated by the images in Figure 1. The aluminum panels with metal finishing (D & G) generally have more corrosion than the other aluminum substrates, and cold rolled steel (I) has more corrosion than the electro-galvanized steel (H). Normalized average area results from on-vehicle service relevant exposures in Detroit, Montreal, St. Johns and the OH/NY Truck route are summarized in Table 3 and plotted in Figure 2.
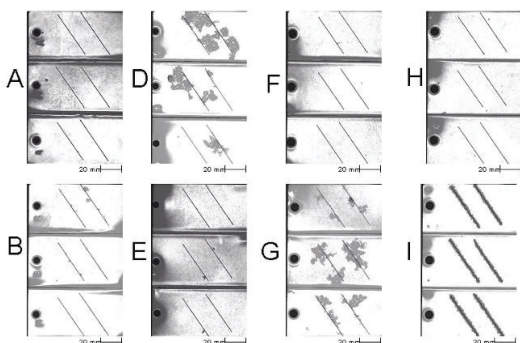
Figure 1. Images of the 3 replicate panels of each substrate from a Detroit on-vehicle exposure with ~2 years exposure.
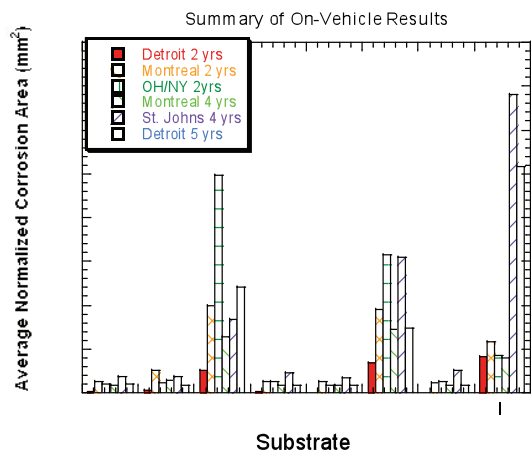
Figure 2. Compiled results from on-vehicle exposures with 2, 4, and 5 years exposure.

Table 3. Summary of Normalized Average Area of Corrosion from the Various On-Vehicle Exposures.

Substrate	Detroit 2 Yrs	Montreal 2 Yrs	Ohio/NY 2 Yrs	Montreal 4 Years	St. Johns 4 Yrs	Detroit 5 Yrs
A	13	129	97	88	184	95
B	27	250	108	148	191	87
D	252	995	2478	641	841	1210
E	10.6	125	130	91	230	91
F	0	128	79	85	174	84
G	348	946	1578	724	1544	745
H	0	110	122	90.9	254	87
I	413	584	432	393	3400	2580

The aluminum panels with metal finishing (D and G) exhibited more corrosion than the aluminum panels with standard paint system (A, E or F) at all of the different exposure sites. This is consistent with other reports in the literature which indicate that metal finishing significantly impacts the susceptibility to filiform corrosion [11, 12].

Corrosion Product Analysis

Table 4 presents the average SEM/EDX composition data from the analysis of the CLIMAT wire samples removed from different on-vehicle exposure locations. For comparison purposes, a reference unexposed aluminum wire was also examined under the same conditions. EDX analyses of the unexposed reference wire indicated the presence of small particles with very low levels of elements such as sodium, sulfur, chlorine, calcium, copper and iron on the reference wire. In contrast, the CLIMAT wire samples from various on-vehicle exposure locations exhibited numerous and large precipitates at the outer surface. The CLIMAT wire from St. John's location exhibited greater amounts of sulfur compared to the chlorine (present commonly as chloride) species. In contrast, Montreal location exhibited greater amounts of chlorine compared to sulfur. The CLIMAT wire from Detroit exhibited an intermediate pattern, with slightly greater amounts of sulfur compared to chlorine.

Table 4. Average Composition of the Precipitates on the CLIMAT Wire Samples from Various Locations.

Location	Elements Detected (wt.%)						
	C	O	Na	Al	S	Cl	Cu
Reference Bare Wire	42	5.5	0.49	49	0.1	0.2	1.6
St. John's, NL	17	35	0.04	36	1.8	0.08	8.6
PointClaire, Montreal, PQ	15	43	3.48	33	1.0	3.2	
Detroit, MI	51	24	0.41	21	0.6	0.3	0.5
Lockport, Buffalo, NY	22	50	0.06	25	1.7	0.04	
Cleveland, OH	29	48	0.06	14	3.3	0.5	0.7
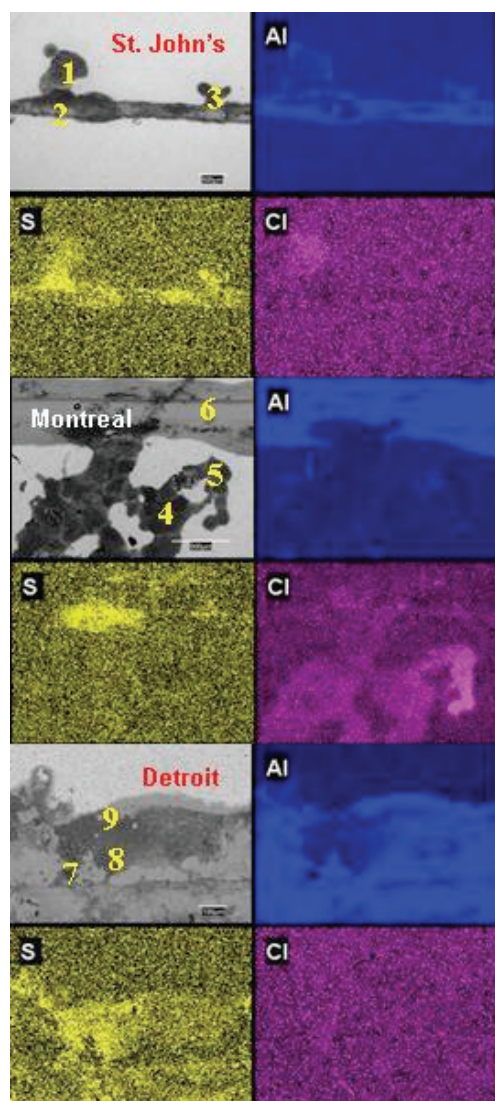
Figure 3. Secondary electron micrograph and elemental distribution maps for Al, S and Cl from a corroded region on substrate A exposed at St. John's for four years (top four micrographs), Montreal for four years (middle four micrographs) and Detroit for five years (bottom four micrographs). The numbers 1 to 9 represent the locations where EDX data was collected. EDX data is presented in Table 5.

Figure 3 presents the secondary electron micrographs of a corroded region from a substrate A panel exposed at St. John's for four years, Montreal for four years and Detroit for five years. Regions containing filiform corrosion filaments are shown in these figures. Elemental distribution maps for Al, S, and Cl are also presented in these figures. Due to space restrictions, the maps for other elements are not shown. The numbers 1 to 9 represent the locations for the EDX data reported in Table 5. The St. John's location indicated the presence of greater amounts of sulfur within the corrosion product region, even at the tip of the filiform filament. Chlorine (as chlorides) was also detected at the tip of the filiform filament at one location. In contrast, the Montreal location exhibited the greater amounts of chlorine at the corroded regions including filiform filaments. Sulfur was detected at the base of the scratch. The Detroit location exhibited greater amounts of sulfur within the corroded regions.

Table 5 presents the EDX composition data for the nine numbered locations denoted on the images in Figure 3. Up to 2.2% sulfur was detected within the corrosion product region on the panel A from St. John's exposure, while chlorine (0.7%) was detected at only one location. The Panel A from Montreal exposure exhibited a reverse trend, with chlorine species detected at more locations and in greater quantities compared to sulfur species. Consistent with EDX maps, the Detroit exposure panel exhibited greater amounts of sulfur and not much chlorine within the corroded regions.

Table 5. EDX composition data from the locations shown in Figure 3.

Exposure Location	Area Analyzed	Al	S	Cl	Ca
St. John's	1	24	0.9	0.7	2.5
	2	23	2.2		0.5
	3	26	1.3		0.4
Montreal	4	25	0.2	0.9	
	5	22		3.7	
	6	66			
Detroit	7	40	2.4		0.9
	8	32	2.9		1.0
	9	27	1.2		

Table 6 summarizes the Cl and S data from EDX spot analyses for substrates A, D, G, and I from panels exposed on-vehicles in the St. Johns and Montreal areas. The results from the EDX spot analysis of the corrosion products on the 4-year St. John's exposure panels indicate that the aluminum panels exhibited sulfur species at more locations than the chloride species. Conversely, the aluminum panels exposed in Montreal tend to show more signs of the presence of chlorine than sulfur which is consistent with the results of the CLIMAT wire analyses.

Table 6. Cl and S content of corrosion products from 4-year St. John's exposure and from 4-year Montreal exposure from EDX spot analyses.

	Panel ID	Number of Spots	S (wt%)	Cl (wt%)
St Johns	A	4	1.7	0.2
	D	6	0.7	2.4
	G	9	0.8	1.3
	I	3	0	0.1
Montreal	A	5	0.1	1.2
	D	7	0.1	0.2
	G	6	0.1	0.5
	I	3	0.3	0.2

Laboratory Test Results

Many of the tests evaluated early on in this project resulted in little or no corrosion on the aluminum panels, even on substrates D and G which showed significant corrosion in the on-vehicle exposures. The following tests did not show any significant corrosion and therefore did not differentiate D and G from the other substrates:

ASTM B117   ASTM D2803   GM9511   ASTM G87   SAE J2334   GM9540P   VDA 621-415

Many other laboratory tests either did not provide the same relative ranking of the substrates as the on-vehicle exposures or provided inconsistent results. After several rounds of laboratory tests and comparison of the results with results from on-vehicle exposures, the list of lab tests of interest was narrowed to two tests: ASTM G85-A2 and ASTM G85-A4. The normalized average area results from the ASTM G85-A2, the ASTM G85-A4 (Constant spray) and the ASTM G85-A4(Intermittent spray) tests are shown in Figure 6. All 3 tests show more corrosion area on the aluminum panels with metal finishing (D and G) than the other aluminum panels with standard paint system applied to the mill finish (non-sanded) substrates (A, E and F). The intermittent spray cycle for the ASTM G85-A4 test is more severe than the constant spray test and therefore appears to better differentiate between the sanded and mill finish panels. However, relative to the on-vehicle exposures, the intermittent ASTM G85-A4 and the ASTM G85-A2 test slightly over-predicted the corrosion for the mill finish substrates.
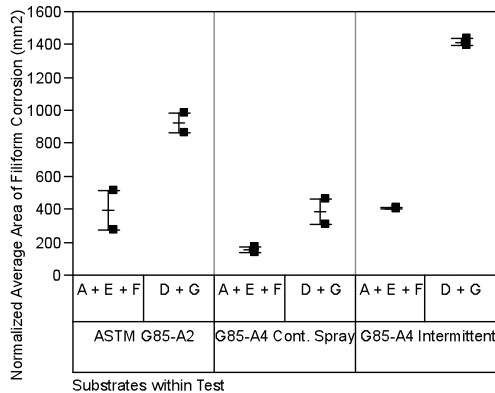
Figure 6.Normalized average area results from the ASTM G85-A2, the ASTM G85-A4 (Constant spray) and the ASTM G85-A4 (Intermittent spray) tests. Duration for all 3 tests = 21 days (~500 hours).
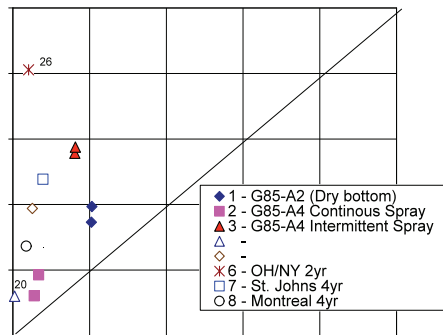
Figure 7. Average normalized corrosion area (mm²) for substrates "A + E + F" versus that for substrates "D + G" for on-vehicle exposures and lab tests: ASTM G85-A2, ASTM G85-A4(constant spray) and ASTM G85-A4 (intermittent spray)

The lab test results are compared with the on-vehicle results in Figure 7. The diagonal line in the plot represents a 1:1 correlation between "D+G" and "A+E+F". All of the data for both the on-vehicle and the 3 lab tests are above the line reflecting the fact that the more corrosion occurred on the sanded panels (D and G) than on the non-sanded panels (A, E and F). The numbers next to the symbols on the plot are the actual ratios of (D + G) to (A+E+F). For the on-vehicle exposures the ratios range from 6:1 to 26:1. The ratios are lower for the lab tests (for example, the ASTM G85-A4 intermittent spray test has the highest ratio for the lab tests at 3.5:1).

EDX spot analyses of the corrosion product were performed on the aluminum and steel panels after being exposed to G85-A4. Results of the EDX spot analyses on panels A, D, G and I are presented in Table 7. It should also be noted that, in addition to the elements shown here, Mg, Si, P and Mn were also detected within the corrosion products. The results presented in this table indicate that sulfur and chloride species could be detected in significant quantities at most of the regions analyzed. The ASTM G85-A4 tests which included both salt and SO_2 in the exposure were the only lab tests conducted that resulted in sulfur incorporation in the corrosion products. However, tests with SO_2 and NaCl in the exposure can mimic S in corrosion products but various factors limit their usefulness. Attempts to repeat these tests have shown a particular lack of repeatability and/or reproducibility. It is also recognized that environmental health and safety issues with handling of SO_2 may preclude use of this type of test at some facilities. Because of these issues there are a limited number of facilities with existing SO_2 testing capability.

Table 7. Cl and S content of corrosion products from ASTM G85-A4 (constant spray) laboratory salt spray test.

	Panel ID	Number of Spots	S (wt%)	Cl (wt%)
ASTM G85-A4	A	7	1.5	2.1
	D	6	1.4	1.6
	G	8	1.3	1.3
	I	6	2.4	4.2

Conclusions

Evaluation of in-service panel exposures shows that all of the panels that were prepared with metal finishing (sanding) prior to paint application exhibit a significantly higher level of cosmetic corrosion than those that were not sanded. Because of this observation, differentiation of the sanded panels from the non-sanded (mill finish) panels was the primary criteria for establishing correlation of accelerated corrosion test results to the in-service exposure results. Many of the existing tests used to evaluate cosmetic corrosion of painted aluminum auto-body panels do not mimic results from on-vehicle exposures because they show too little corrosion on sanded panels (D and G).

Another observation from the in-service panel exposures was the presence of sulfur along with chloride in the corrosion product on aluminum panels in some cases. Therefore, in order to mimic corrosion products observed on in-service aluminum sheet corrosion in certain atmospheric environments, sulfur may need to be included in the accelerated test exposure.

The accelerated corrosion tests that show the greatest promise at mimicking in-service aluminum corrosion are ASTM G85–A2 and ASTM G85–A4. Both of the accelerated tests are acidified to a pH of 2.5-3.2. An acidic exposure environment appears to be a key parameter when trying to mimic in-service corrosion performance with an accelerated test. However, many of the industry accepted standards for accelerated corrosion tests of steel are run in neutral environments. Neutral environments evaluated in this program induced little or no corrosion on the painted aluminum panels. While the ASTM G85 – Annex 2 does not include sulfur in the exposure, the acidic exposure provides the necessary environment to induce corrosion on aluminum that replicates the morphology of corrosion on the in-service panels.

ASTM G85-A4 provides both the acidic exposure and the exposure to sulfur, but can be a difficult test to run due to the use of sulfur dioxide (SO_2) gas. Attempts were made to modify the ASTM G85-A2 and -A4 tests by using sulfuric acid in the exposure, it was found that sulfuric acid in the exposure was not as effective at inducing corrosion on the painted aluminum panels as either acetic acid in ASTM G85–A2 or the SO_2 in ASTM G85 – A4. Tests with SO_2 and NaCl in the exposure can mimic S in corrosion products but various factors limit their usefulness. Attempts to repeat these tests have shown a particular lack of repeatability and/or reproducibility. It is also recognized that environmental health and safety issues with handling of SO_2 may preclude use of this type of test at some facilities. Because of these issues there are a limited number of facilities with existing SO_2 testing capability.

Of all of the test methods evaluated in this project, ASTM G85-A2 appears to be the most reliable test for evaluating filiform corrosion of painted Aluminum auto-body panels. The test method consistently provides the same relative ranking and cosmetic corrosion morphology as is observed in service relevant on vehicle exposures. It should be noted however, the ATM G85-A2 test cannot mimic the sulfur that is observed in corrosion products in certain environments.

References

1. F.S. Bovard, J. Tardiff, T. Jafolla, D. McCune, G. Courval, K. Smith, S. Ramamurthy, R. Singleton, F. Vartolas, and J. Repp, "Development of an Improved Test for Finished Aluminum Autobody Panels", SAE Paper No. 2008-01-1156, SAE 2008, April 2008.

2. F.S. Bovard, J. Tardiff, T. Jafolla, D. McCune, G. Courval, K. Smith, F. Lee, S. Ramamurthy, J. Shaffer, F. Vartolas, and J. Repp, "Update on the Development of an Improved Test for Finished Aluminum Autobody Panels", SAE Paper No. 2007-01-0417, SAE 2007, April 2007.

3. F.S. Bovard, J. Tardiff, T. Jafolla, D. McCune, G. Courval, K. Smith, F. Lee, F. Lutze, and J. Repp, "Development of an Improved Test for Finished Aluminum Autobody Panels", SAE Paper No. 2005-01-0542, SAE 2005 Transactions Journal of Materials and Manufacturing, March 2005.

4. G. Courval, K. Smith, C. Meade, F. Lutze, F. Bovard, and T. Jafolla, "Development of an Improved Test for Finished Aluminum Autobody Panels", SAE Paper No. 2003-01-1235, Proceedings of SAE World Congress, March 2003.

5. F.S. Bovard, J. Tardiff, T. Jafolla, D. McCune, G. Courval, K. Smith, S. Ramamurthy, R. Singleton, F. Vartolas, and J. Repp, "Update on the Development of an Improved Test for Finished Aluminum Autobody Panels", SAE Paper No. 2009-01-0891, SAE 2009, April 2009.

6. SAE J2334, "Cosmetic Corrosion Lab Test", Society of Automotive Engineers, Warrendale, PA, June 1998.

7. Lee, F., Pourdeyhimi B, and Adamsons, K, "Analysis of Coatings Appearance and Surface Defects Using Digital Image Capture/Processing/Analysis", The International Symposium on a Systems Approach to Service Life Prediction of Organic Coatings, Breckenridge, Co, Sep 14-19, 1997

8. ASTM G85-98 Annex 2, "Cyclic Acidified Salt Fog Testing", Annual Book of ASTM Standards, Vol. 3.02, 2005.

9. ASTM G85-98 Annex 4, "Salt/SO2 Spray Fog Testing", Annual Book of ASTM Standards, Vol. 3.02, 2005.

10. D.P.Doyle and T.E. Wright, "Rapid methods for Determining Atmospheric Corrosivity and Corrosion resistance", pp 227-43, Atmospheric Corrosivity, edited by W.H. Ailor, 1982.

11. E.L. Colvin, et. al., "Filiform Corrosion of Aluminum Auto Body Sheet in Accelerated and Outdoor Environments", SAE Paper No. 970735, Proceedings of SAE World Congress, Feb. 1997.

12. L.F. Vega, et. al. "Influence of Surface Treatments on Durability of Painted Aluminum Alloys", SAE Paper No. 970731, Proceedings of SAE World Congress, Feb. 1997.

Presentations/Publications/Patents

SAE 2002B-203

SAE 2003-01-1235

SAE 2005-01-0542

SAE 2006 Oral Only

SAE 2007-01-0417

SAE 2008-01-1156

SAE 2009-01-0891